

**Numerical Study of Glassy Systems:  
Fragility of Supercooled Liquids,  
Ideal Glass Transition of Randomly Pinned Fluids,  
and  
Jamming Transition of Hard Spheres**

Misaki Ozawa  
Doctoral Program in Physics

Submitted to the Graduate School of  
Pure and Applied Sciences  
in Partial Fulfillment of the Requirements  
for the Degree of Doctor of Philosophy in  
Science

at the  
University of Tsukuba



# Contents

<b>1</b>	<b>Introduction</b>	<b>5</b>
1.1	What is the glass transition? . . . . .	5
1.1.1	Thermodynamic properties . . . . .	5
1.1.2	Dynamic properties . . . . .	6
1.2	Fragility . . . . .	7
1.2.1	Fragile vs. Strong glass formers . . . . .	7
1.2.2	What is the origin of super-Arrhenius behavior? . . . . .	9
1.3	Ideal glass transition . . . . .	10
1.4	What is the jamming transition . . . . .	12
1.4.1	Hard-Sphere packing . . . . .	12
1.4.2	How is the jamming transition related to the glass transition? . . . . .	13
1.5	Targets of the thesis . . . . .	14
1.6	Computer simulation of glassy systems . . . . .	15
<b>2</b>	<b>Fragility of Supercooled Liquids</b>	<b>17</b>
2.1	Motivation . . . . .	17
2.2	Methods . . . . .	18
2.3	Results . . . . .	19
2.3.1	Structural properties . . . . .	19
2.3.2	Dynamic properties . . . . .	22
2.3.3	Dynamical heterogeneities . . . . .	27
2.4	Discussion and Future work . . . . .	31
<b>3</b>	<b>Ideal Glass Transition of Randomly Pinned Fluids</b>	<b>33</b>
3.1	Motivation . . . . .	33
3.2	Methods . . . . .	35
3.3	Results . . . . .	38
3.3.1	Entropy and configurational entropy . . . . .	38
3.3.2	Overlap approach . . . . .	40
3.3.3	Potential energy landscape and its saddle points . . . . .	41
3.3.4	Phase diagram . . . . .	43
3.4	Conclusion and discussion . . . . .	44
<b>4</b>	<b>Jamming Transition of Hard Spheres</b>	<b>45</b>
4.1	Motivation . . . . .	45
4.2	Methods . . . . .	46
4.3	Results . . . . .	47
4.3.1	Onset of denser jamming transition points and the dynamic transition . . . . .	47
4.3.2	Geometrical and vibrational properties . . . . .	49
4.3.3	Local structure of denser jammed packings . . . . .	56
4.3.4	Bond orientational order . . . . .	60
4.3.5	Hidden onset of growth of locally preferred structures . . . . .	60

4.4 Conclusion . . . . .	66
<b>5 Summary and Future Works</b>	<b>69</b>
<b>A The Adam Gibbs Theory</b>	<b>71</b>
A.1 Dynamics and configurational entropy . . . . .	71
A.2 Relation with the VFT equation . . . . .	72
<b>B The Mode-Coupling Theory</b>	<b>73</b>
B.1 The MCT equation . . . . .	73
B.2 The MCT transition points for the binary hard-sphere systems . . . . .	74
<b>C Configurational entropy of the pinned systems</b>	<b>77</b>
C.1 Statistical mechanics of the pinned systems . . . . .	77
C.2 Total entropy of the pinned systems . . . . .	78
C.3 Vibrational entropy of the pinned systems . . . . .	81
C.4 Anharmonic contribution for the vibrational entropy . . . . .	82
C.5 Finite size effect . . . . .	83
<b>D Effects of pinning on glass states</b>	<b>85</b>
D.1 Effects of pinning on the vibrational entropy of the glass states . . . . .	85
<b>E Saddle points and dynamic transition point</b>	<b>89</b>

# Chapter 1

## Introduction

In this thesis, we focus on three research topics related to the glass transition. We use computer simulations to study these topics. In this section, we briefly explain physics of the glass transition, basic methods of the computer simulations, and motivation of this thesis.

### 1.1 What is the glass transition?

When liquids are cooled or compressed, they freeze and become crystals at a melting temperature or pressure. For example, water freezes at 0 degrees in Celsius under 1 atm. But, if we quench the liquids (cooling or compressing rapidly) or add impurities to them, the crystallization is avoided and they maintain random configurations even below (above) the melting temperature (or pressure). This state is referred to as the supercooled state. Cooling (or compressing) further, the supercooled liquids freeze in amorphous states at a certain temperature (or pressure). This phenomenon is called the glass transition and this transition point is referred to as the glass transition temperature  $T_g$  (or pressure  $P_g$ ). In short, the glass transition is the phenomenon that constituent particles like atoms and molecules solidify with amorphous configurations. The most familiar glassy material in our daily life is the window glasses, which are mainly composed of silicon and oxygen atoms with an amorphous configuration. The glassy materials are not limited to the window glasses. For instance, metallic glasses, polymer glasses, colloidal glasses, and even biological cells often behave like glassy materials. Thus, the glassy materials are widely seen and the glass transition is thought to be universal.

One of the feature of the glass transition which many researchers are attracted to study is an anomalous dynamics. In general, the dynamics of the supercooled liquids dramatically slows down when the systems approach the glass transition points. As we shall explain later, the relaxation time and the transport coefficients such as viscosity of the system increase more than 10 decades within narrow temperature and pressure windows. Besides, the systems also show heterogeneous dynamical behavior in real space, which means that motion of particles forms a patchwork of clusters of mobile and immobile particles. This behavior implies that there exists a certain collective phenomenon in a relaxation process of the supercooled liquids near the glass transition point.

Understanding the nature of the glass transition and the anomalous dynamics of the supercooled liquids are the ultimate goal [1, 2]. In the subsequent subsections, we explain thermodynamic and dynamic properties of the glass transition in more detail.

#### 1.1.1 Thermodynamic properties

The entropy is an useful observable to characterize thermodynamic properties of the glass transition. Here we discuss the entropy  $S$  of the supercooled liquids and its relation to the glass transition.  $S$  is usually obtained by integrating the specific heat measured by calorimetric experiments.

Normal materials transform from the liquid state into the crystal state as they undergo the first order phase transition at melting temperatures, where  $S$  changes discontinuously as shown in Fig. 1.1. If we quench the liquids or introduce frustration against crystallization by, for example, adding im-

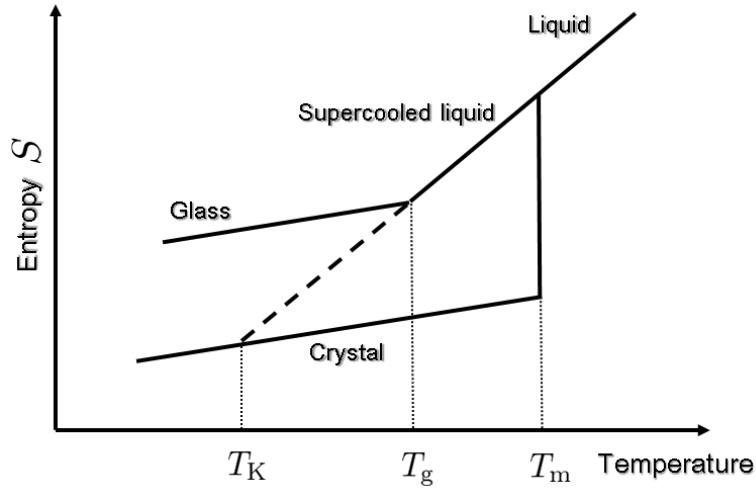


Figure 1.1: Schematic plot of the entropy as a function of temperature.

purities, the first order phase transition is avoided and the systems become the supercooled state. We can cool the system further along the supercooled liquid-line. Concomitantly, the relaxation time increases rapidly. Eventually, the relaxation time of the system exceeds the experimental time scale and the system falls in out-of-equilibrium, *i.e.*, it becomes non-ergodic.<sup>1</sup> This is seen as the point at which the supercooled liquid line bends sharply and becomes almost parallel to the crystal line in Fig. 1.1. We define this point as the empirical glass transition temperature  $T_g$  by the thermodynamic measurement. The state in this out-of-equilibrium branch is called the glass state. Many glassy materials including the widow glasses follow the path shown in Fig. 1.1 to become the glasses. Note that  $T_g$  depends on the experimental time scale. Hence, the more we wait for the measurement, the more the system can go down to low temperature along the supercooled liquid line in equilibrium, which means that  $T_g$  is lowered further. Apparently,  $T_g$  is not uniquely determined but varies depending on the experimental timescales. This is a major difference between the glass transition and usual equilibrium phase transitions.

### 1.1.2 Dynamic properties

Here, we explain dynamic properties of supercooled liquids near the glass transition point. The relaxation time  $\tau_\alpha$  and transport coefficients, especially the viscosity  $\eta$ , are useful quantities to discuss dynamics of the supercooled liquids.  $\eta$  is a macroscopic quantity and is often measured by rheometers [3]. On the other hand,  $\tau_\alpha$  is a microscopic observable and typically defined as a characteristic time scale of the time correlation functions of the density and stress fluctuations [4]. In many cases,  $\eta$  is proportional to  $\tau_\alpha$  as can be explained by the Maxwell's viscoelastic model [3] or the Green-Kubo formula [4].

In Fig. 1.2, experimentally measured viscosity  $\eta$  are shown for several supercooled liquids as a function of the inverse temperature [5]. Note that  $\eta$  is plotted in the logarithmic scale. Interestingly,  $\eta$  increases more than ten decades for all supercooled liquids. It means the dynamics becomes extremely sluggish when the temperature is lowered. All data points shown in Fig. 1.2 terminate around  $\eta \simeq 10^{13}$  poise simply because measuring  $\eta$  more than this value is very difficult. For this reason,  $\eta(T_g) = 10^{13}$  poise is used as another definition of the empirical glass transition temperature  $T_g$ . We have already introduced  $T_g$  as the point at which the entropy  $S$  bends. Empirically, the two different  $T_g$  are close to each other. Thus, hereafter, we regard them to be identical. We emphasize that  $T_g$  defined by viscosity is also an empirical variable which depends on the technical limit of the rheometer (in this

<sup>1</sup>Rigorously speaking, the supercooled state is a metastable state with respect to the crystalline ground state. Thus, equilibrium state of the supercooled liquids might be thought to be ill-defined. But in practice, we can safely treat the system as thermally equilibrated as long as the time scale is shorter than the nucleation time.

case  $10^{13}$  poise). In other words,  $T_g$  is an artificial value and not uniquely determined as we said in the previous subsection.

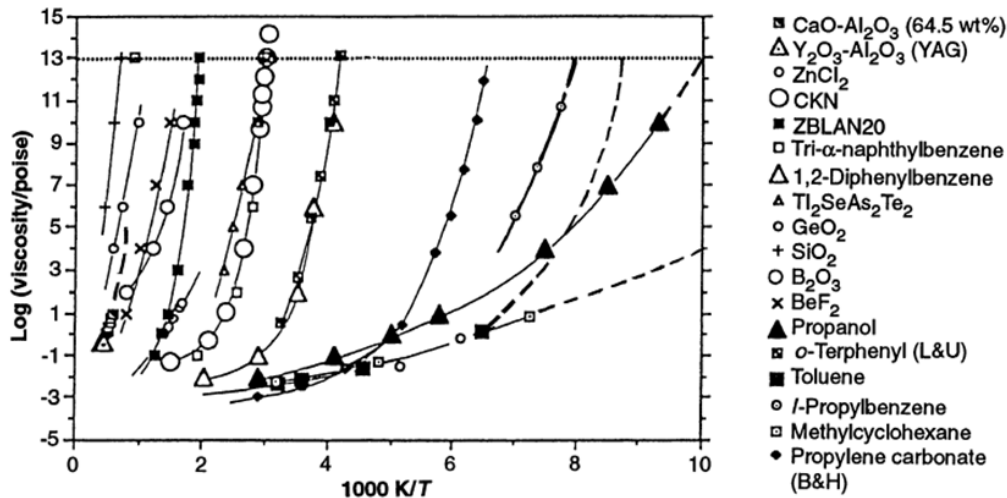


Figure 1.2: The viscosity of the supercooled liquids near the glass transition temperatures measured by experiments as functions of the inverse temperature. This figure is from CA. Angell. *Science*, 267(5206):1924-1935, 1995 [5].

Next, we explain microscopic relaxation process of the supercooled liquids. As we discussed before, the time correlation functions play a central role to describe the microscopic dynamics. In Fig. 1.3, we show a computer simulation result [6] of the density-density correlation function,  $F(k, t)$  defined by

$$F(k, t) = \frac{1}{N} \langle \delta \rho_{\mathbf{k}(t)} \delta \rho_{-\mathbf{k}}(0) \rangle, \quad (1.1.1)$$

where  $\delta \rho_{\mathbf{k}(t)}$  is the Fourier transform of the density fluctuation [4]. The relaxation time  $\tau_\alpha$  is defined by  $F(k, \tau_\alpha) = e^{-1}$ . Note that the horizontal axis, time, is scaled in the logarithmic scale. At high temperatures,  $F(k, t)$  shows exponential decay like normal liquids. However, when the temperature is lowered, the relaxation curve is stretched and  $F(k, t)$  shows the two-step relaxation which is thought to be a sign of the glassy behavior. Concomitantly, the characteristic time scale,  $\tau_\alpha$  increases rapidly.

We have explained the dramatic slowdown of the dynamics of the supercooled liquids from both macroscopic and microscopic dynamics. Here we briefly mention the relation between the dynamics and configurations of particles. It is well known that, while the dynamics changes qualitatively within narrow temperature windows, the static quantities such as the static density distribution function, which contains the configurational information of particles, show little changes [6, 7]. This is totally different from the situation of the critical slowing down at the second order phase transition point, where the dramatic change of the static properties of the order-parameter induces and controls the dynamics [8]. Therefore, the slowing down of the dynamics without resorting to any apparent structural changes is a distinct property of the glass transition.

## 1.2 Fragility

In this section, we discuss the temperature dependence of  $\eta$  and  $\tau_\alpha$  for supercooled liquids in more detail. In particular, their functional forms are discussed to characterize the dynamics near  $T_g$ .

### 1.2.1 Fragile vs. Strong glass formers

First, we explain the temperature dependence of  $\eta$  and  $\tau_\alpha$  for normal liquids before discussing the supercooled liquids. It is empirically known that in the liquid state,  $\eta$  and  $\tau_\alpha$  increase with decreasing

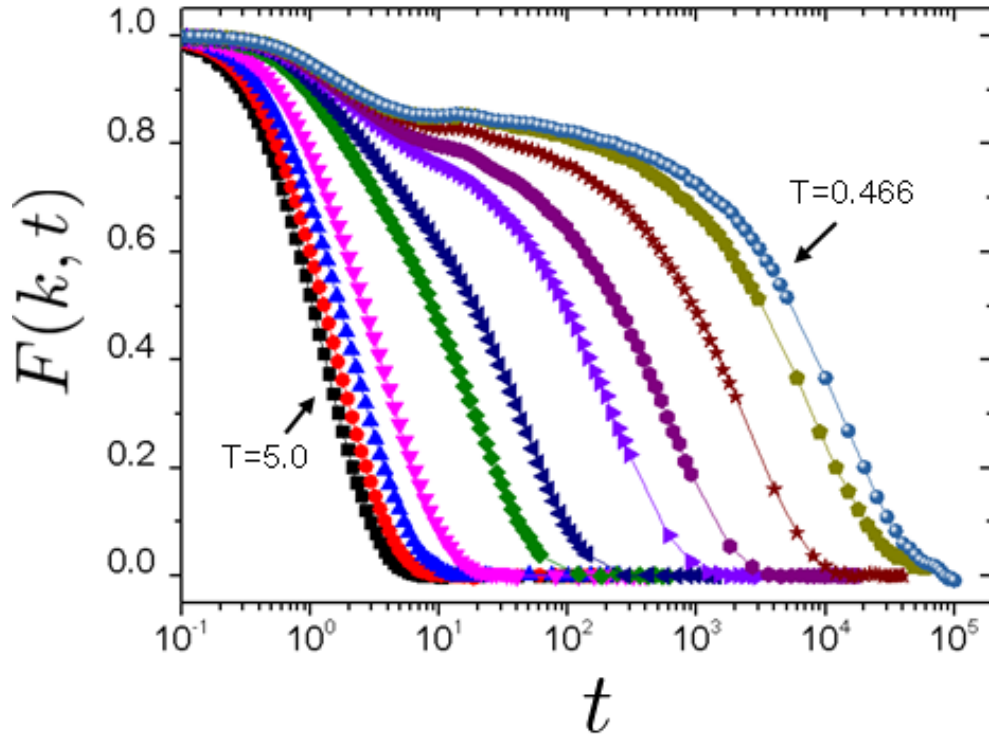


Figure 1.3: The density-density time correlation function from a computer simulation result. The wave number  $k$  is fixed at the position of the first peak of the static structure factor  $S(k) = F(k, 0)$ . This figure is replotted from W. Kob and H. C. Andersen. *Physical Review E*, 52(4):4134, 1995 [6].

the temperature and obey the Arrhenius law<sup>2</sup>,  $\eta, \tau_\alpha \propto \exp[E/T]$ . The Arrhenius law can be explained by the phenomenology proposed by Eyring [9]. Here we briefly explain Eyring's argument on the Arrhenius law. In a liquid, a constitute particle is surrounded by the cage formed by neighboring particles. The elementary relaxation process of the liquid is assumed to be the breaking of the cage and escape of the particle from it. This can be regarded as a rate process with an activation energy  $E$ . Therefore,  $\tau_\alpha^{-1} \propto \exp[-E/T]$  is concluded. In this argument,  $E$  is assumed to be insensitive to the temperature, *i.e.*,  $E$  is constant.

Next, let's move on to the supercooled liquid case. Does the dynamics of the supercooled liquids also obey the Arrhenius law? To answer this question, we introduce the so-called Angell plot [5], which is suitable to discuss whether a system obeys the Arrhenius law or not. The Arrhenius law is represented by a straight line if  $\log \eta$  (or  $\log \tau_\alpha$ ) is plotted against  $1/T$  like Fig. 1.2. However, Fig. 1.2 is not suitable to check how straight they are, since characteristic temperature scales vary depending on glass formers. Thus, Fig. 1.2 should be rescaled by a characteristic temperature such as  $T_g$ . This is the Angell plot shown in Fig. 1.4 [5].

The temperature dependence of  $\eta$  for some glass formers such as  $\text{SiO}_2$  and  $\text{GeO}_2$  are certainly straight lines in the Angell plot, which indicates their dynamics obey the Arrhenius law. On the other hand, most other glass formers (o-terphenyl, toluene, etc...) show apparent deviation from the Arrhenius law. This non-Arrhenius behavior is sometimes called super-Arrhenius. The super-Arrhenius temperature dependence is empirically well fitted by the Vogel-Fulcher-Tammann (VFT) equation,

$$\eta = \eta_\infty \exp \left[ \frac{1}{K(T/T_0 - 1)} \right] \quad \text{or} \quad \tau_\alpha = \tau_\infty \exp \left[ \frac{1}{K(T/T_0 - 1)} \right], \quad (1.2.1)$$

<sup>2</sup>Contrary to the liquid and the supercooled state,  $\eta$  decreases with decreasing the temperature in the gas state. According to Maxwell's momentum transfer argument, for dilute gases,  $\eta$  behaves as  $\eta \propto \sqrt{mk_B T}$ , where  $m$  and  $k_B$  are single particle mass and the Boltzmann constant respectively.

where  $\eta_\infty$ ,  $\tau_\infty$ ,  $K$  and  $T_0$  are fitting parameters. In the glass research community, glass formers whose relaxation time and transport coefficients obey the Arrhenius law are referred to as *strong* glass former. On the other hand, the ones which show the super-Arrhenius behavior are called the *fragile* glass former [5]. As shown in Fig. 1.4, there are variety of glass formers between very strong glass formers ( $\text{SiO}_2$  and  $\text{GeO}_2$ ) and very fragile ones (o-terphenyl, toluene, etc...). The degree to measure how fragile (or strong) the system is is called *fragility* [5], which quantifies how much the dynamics deviates from the simple Arrhenius law. There are several definitions of the fragility in experiments and computer simulation studies [10]. Representative one is the steepness index  $m$  given by

$$m = \left. \frac{\partial \log_{10} \eta(T)}{\partial (T_g/T)} \right|_{T=T_g} \quad \text{or} \quad m = \left. \frac{\partial \log_{10} \tau_\alpha(T)}{\partial (T_g/T)} \right|_{T=T_g}. \quad (1.2.2)$$

The parameter  $K$  in the VFT equation Eq. (1.2.1) is another well known definition of the fragility. Tuning  $\eta_\infty$ ,  $K$  and  $T_0$ , we can fit all data of the Angell plot of Fig. 1.4. Both  $m$  and  $K$  are large if the system is the fragile glass former:  $m = 20$  for the typical strong glass former,  $\text{SiO}_2$  [11], and  $m = 81$  for the typical fragile glass former, o-terphenyl [12]. Note that  $m$  and  $K$  are related to each other when  $\eta$  or  $\tau_\alpha$  is well fitted by Eq. (1.2.1) [13]. If we use Eq. (1.2.1) and Eq. (1.2.2), we get

$$m = \frac{1}{K \ln 10} (T_0/T_g) / (1 - T_0/T_g)^2. \quad (1.2.3)$$

Eq. (1.2.3) indicates  $m$  depends on  $K$  and  $T_0/T_g$ , which characterizes distance between  $T_0$  and  $T_g$ . The more the distance is close, the more  $m$  is large.

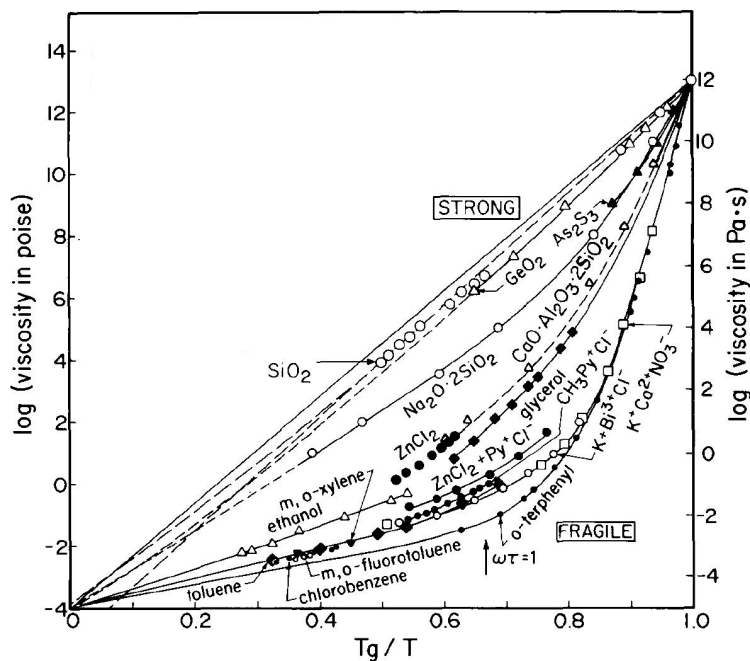


Figure 1.4: The Angell plot. This figure is from CA. Angell. *Journal of Non-Crystalline Solids*, 102(1):205-221, 1988 [14]. We cut the insert of the original figure.

### 1.2.2 What is the origin of super-Arrhenius behavior?

In the last subsection, we have introduced the notion that the glass formers can be classified as the strong and fragile ones whose dynamics obey the Arrhenius and super-Arrhenius law, respectively. The fragility which quantifies the degree of deviation from the simple Arrhenius law is also introduced. However, why does the dynamics of some glass formers show the super-Arrhenius temperature

dependence? In other words, what is the origin of the super-Arrhenius behavior? This question is one of the fundamental problems in the glass transition study [1,2].

Here, we briefly discuss the super-Arrhenius behavior with a phenomenological argument based on that of Eyring. Dynamics of the strong glass formers obey the Arrhenius law, and it indicates that the activation energy  $E$  of the elementary relaxation process is constant up to  $T_g$ . On the contrary, the super-Arrhenius behavior shown in the fragile glass formers implies that  $E$  is no longer a constant but temperature dependent, *i.e.*,  $E \rightarrow E(T)$  and  $E(T)$  increases with decreasing the temperature. The increase of  $E(T)$  is interpreted as a result that the number of particles participating the elementary relaxation processes increases and hence certain "collective" motions among them emerge. Indeed, clusters of mobile and immobile particles forming a heterogeneous patchwork have been observed in real space by the experiments and the computer simulations [15]. These observed heterogeneous dynamics can be regarded as an emergence of the collective motions of the particles. In short, when the temperature is lowered, these clusters for the elementary relaxation processes grow, and thus  $E(T)$  increases and the super-Arrhenius behavior results. The above argument is intuitive and requires more quantitative explanation. For example, we do not know what precisely  $E(T)$  is. The argument is assuring the existence of a certain collective phenomenon in the glass transition [16], which attracts many researchers in the field.

We repeat that the origin of the super-Arrhenius behavior is still unclear. How does the collective phenomenon is related to the slowing down of the dynamics [2,17]? And what is the essential difference between the strong and the fragile glass formers [10]? One of the goal of the field is to answer these questions from the microscopic point of view.

In this thesis, we investigate the origin of the super-Arrhenius behavior by using the computer simulation. This is the first topic of the thesis discussed in Chap. 2.

### 1.3 Ideal glass transition

We have stated that  $T_g$  is an empirical value and not uniquely determined.  $T_g$  is defined as the position at which the entropy sharply changes, or its temperature derivative, the specific heat, jumps. Or, alternatively,  $T_g$  is defined by the viscosity measurement as the point at which  $\eta$  reaches  $10^{13}$  poise. In general, if we decrease the cooling rate or wait for a long time, the system goes down to the equilibrium branch shown as the dashed line in Fig. 1.1 and thus  $T_g$  shifts to the low temperature. However, if we can cool the system with the infinitesimal cooling rate or the infinite waiting time, what happens at the very low temperature? Fig. 1.1 indicates that the entropy of the supercooled state  $S$  keeps decreasing and eventually crosses the crystal entropy  $S_{\text{cry}}$  at a finite temperature (which we shall denote as  $T_K$ ). Below  $T_K$ ,  $S$  may go down further. But, this is somewhat paradoxical since the supercooled liquids have random configurations like liquids and thus their entropy should not be lower than the entropy of the ordered crystal. Therefore, an anomaly should happen around  $T_K$ . This argument is called Kauzmann's paradox proposed more than 60 years ago [18].

The above argument can be interpreted using the notion of the number of states. The essence of this interpretation is to relate the excess entropy  $S_{\text{exc}} = S - S_{\text{cry}}$  measured by the experiments with the number of microscopic states  $\mathcal{N}$  available for the system. The logarithmic of  $\mathcal{N}$  is called the configurational entropy  $S_c$  and we can assume that it is identical to  $S_{\text{exc}}$ .<sup>3</sup>  $S_c$  plays a central role in the thermodynamic description of the glass transition. Hereafter, we use  $S_c$  to discuss the thermodynamics instead of  $S_{\text{exc}}$ . The Kauzmann's paradox discussed above can be explained in terms of  $S_c$  as shown in Fig. 1.5. Decreasing  $S_c$  with decreasing the temperature is rephrased as reducing of the number of available states. If the temperature is lowered with infinitely small cooling rate,  $S_c$  becomes zero, which means  $\mathcal{N}$  becomes sub-exponential, *i.e.*, the configuration of the particles is almost uniquely determined. This state of matter is called the ideal glass state and an *equilibrium*

---

<sup>3</sup>At very low temperatures, the supercooled liquid is so sluggish that the particles would vibrate only around fixed positions. Thus,  $S$  is mainly composed of the vibrational contribution  $S_{\text{vib}}$  and the logarithm of the number of available random states  $S_c$ , *i.e.*,  $S \simeq S_{\text{vib}} + S_c$ . Empirically, it is known that the vibrational entropy of the crystal  $S_{\text{cry}}$  and  $S_{\text{vib}}$  are close,  $S_{\text{cry}} \simeq S_{\text{vib}}$ . Therefore, we can conclude that  $S_{\text{exc}} \simeq S_c$ .

transition from the supercooled state into the ideal glass state is called the ideal glass transition [19]. The point  $T_K$  at which the ideal glass transition takes place is often referred to as the ideal glass transition temperature or the Kauzmann's temperature. However, the existence of the ideal glass transition and  $T_K$  are still hypothesis and has not been proved yet. Nobody has reached  $T_K$  and observed the ideal glass transition because the relaxation time diverges at the point as we explain the below.

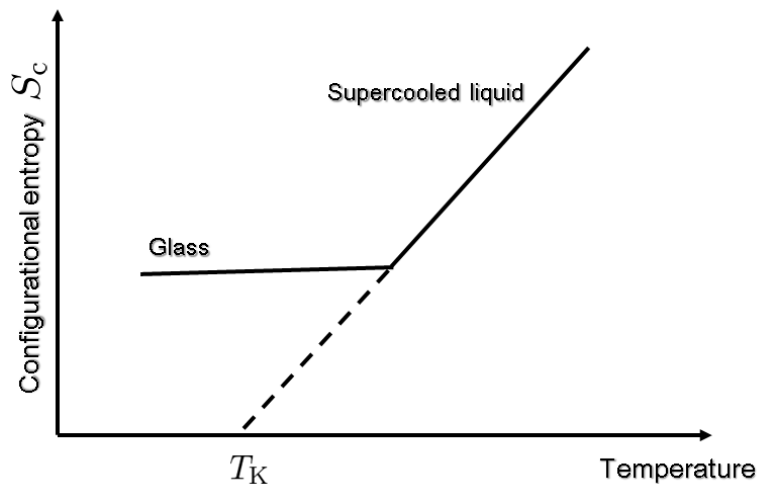


Figure 1.5: Schematic plot of the Kauzmann's paradox.

Interestingly, the temperature dependence of the dynamical observables such as  $\eta$  and  $\tau_\alpha$  discussed in the previous subsections also suggest the existence of a singular point in finite temperature. We have explained that  $\eta$  or  $\tau_\alpha$  for many glass formers can be well fitted by the VFT equation, Eq. (1.2.1). This equation indicates that there exists a temperature  $T_0$  at which  $\eta$  or  $\tau_\alpha$  diverge, *i.e.*, the dynamics completely freezes. Interestingly,  $T_0$  obtained by fitting  $\eta$  or  $\tau_\alpha$  are very close to  $T_K$  extrapolated from  $S_{exc}$  for many glass formers. We show  $T_K$  vs.  $T_0$  plot in Fig. 1.6 to see the correlation between them [20]. The straight line indicates  $T_K \simeq T_0$  holds. This means the dynamics data also supports the existence of the ideal glass transition.

There are some theories of the glass transition which describe the slowing down of the dynamics in terms of this anomalous thermodynamics in the system. The Adam Gibbs theory (AGT) and its refined version, the random first order transition theory (RFOT) are based on the existence of the ideal glass transition, both of which claim that the singularity of thermodynamics, *i.e.*, vanishing of the configurational entropy, is responsible for the dynamical slowing down. The AGT and the RFOT connect the dynamical observables  $\eta$  or  $\tau_\alpha$  with the configurational entropy  $S_c$  and explain that the dramatic increase of  $\eta$  and  $\tau_\alpha$  is due to decreasing of the number of available states. The theories state that the singularity of  $T_K$  causes growing of collective motions of the particles and hence the activation energy increases. This is the origin of the super-Arrhenius behavior explained from the thermodynamic point of view. The AGT is briefly explained in Appendix A, and the RFOT will be explained in Chap. 3. The basic concepts of the AGT are deduced from the RFOT.

Although the above statement seems to be reasonable, we emphasize again that the existence of the ideal glass transition has not been proved yet. All previous studies of  $T_K$  rely on unreliable extrapolations from the temperature dependence of  $S$  at higher temperatures [21]. Proving (or disproving) the existence of the ideal glass transition is the most fundamental problem in the study of the glass transition. This is the second topic of this thesis and will be discussed in Chap. 3.

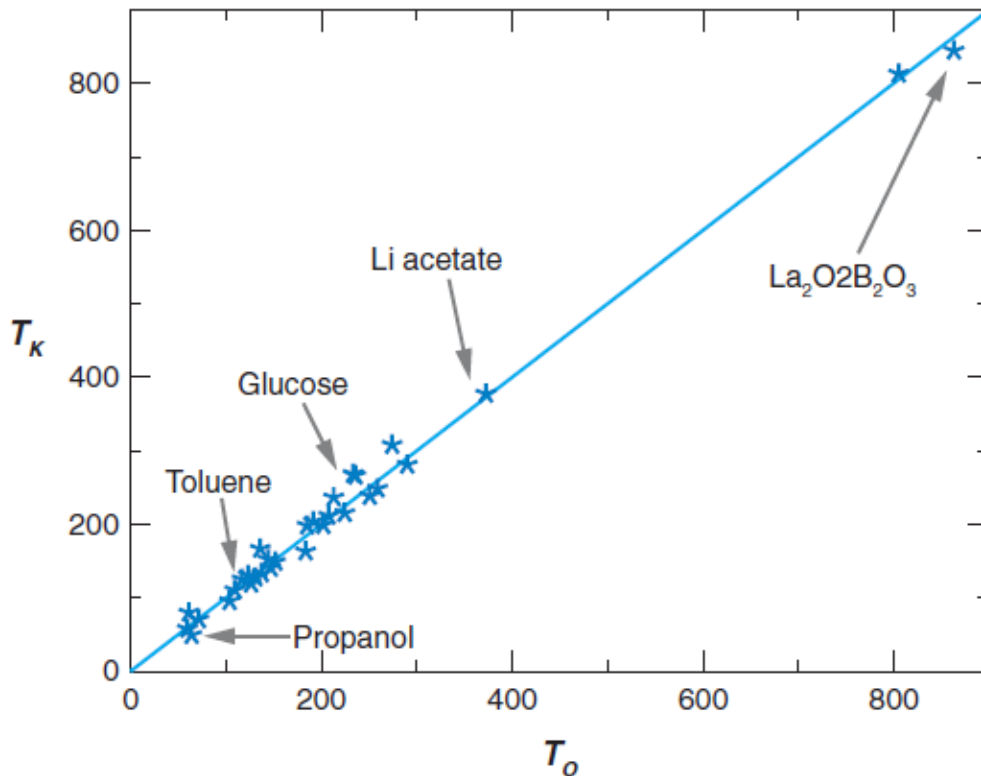


Figure 1.6: Correlation between  $T_K$  and  $T_0$  for many glass formers. This figure is from V. Lubchenko and P.G. Wolynes. *Annual Review of Physical Chemistry*, 58:235-266, 2006 [20].

## 1.4 What is the jamming transition

In this section, we briefly explain the jamming transition and its properties. Macroscopic particles like grains, pinballs, and colloids can flow easily when some external forces are applied. However, when the densities of these particles are increased above a certain value, any movement is no longer allowed, and the systems become a solid with random configurations. This phenomenon is called the jamming transition and a density at which they get stuck and solidify is called the jamming transition point. We emphasize that the jamming transition is purely "athermal" phenomenon because the constituent particles are so large that they are not affected by the thermal noises.

### 1.4.1 Hard-Sphere packing

To understand the nature of the jamming transition, here we consider the simplest example, the hard-sphere packing problem [22]. Imagine that we pack a bunch of identical hard spheres like pinballs into a large container. The most efficient way to put as much of spheres as possible into the container is to lay out the spheres periodically so that they form the face centered cubic (FCC) or the hexagonal close packed (HCP) structures. It is well known that the volume fraction (volume of the entire spheres divided by the container's one)  $\varphi$  of the FCC and the HCP structures are  $\varphi_{\text{FCC}} = \varphi_{\text{HCP}} = \sqrt{2}\pi/6 \simeq 0.7405$ . This value is proved to be the largest in three dimensions, which is known as the "Kepler conjecture". However, when we throw the spheres into the container at random, or compress the container rapidly, the spheres fill the container in a disordered manner as shown in Fig. 1.7. Surprisingly, the volume fraction of the system is always  $\varphi_J \simeq 0.64$ , if the container is large enough [23]. This is the jamming transition point of the hard-sphere system, which is confirmed by many experiments and computer simulation studies.

It is also well known that at  $\varphi_J$ , the configuration of the particles has distinct geometrical proper-

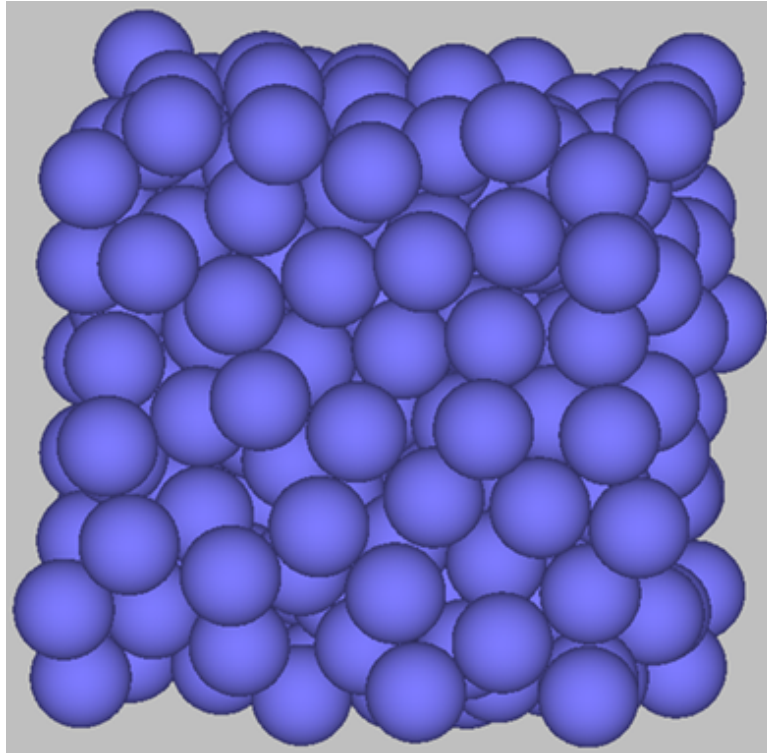


Figure 1.7: A snapshot of the monodisperse hard spheres at the jamming transition point  $\varphi_J \simeq 0.64$ . The configuration is generated by the computer simulation.

ties. The averaged contact number  $Z$  is an useful variable to characterize geometrical properties of the jammed systems. In the FCC crystalline structure, each particle contacts with 12 neighbor particles, thus  $Z = 12$ . On the contrary, the jammed system at  $\varphi_J$ , the contact number for each particle makes a distribution due to the random configuration. Remarkably, the *averaged* contact number for the system is always  $Z = 6$  in three dimensions. In general,  $Z = 2d$  holds, where  $d$  is dimension of the system, and it is understood to be a distinct property of the jamming transition point.  $Z = 2d$  can be interpreted as a condition of a marginal stable state. This identity has been proposed by Maxwell in 1864 [24] and can be shown in the following. Imagine that a jammed configuration of  $N$  hard spheres with  $Z$  in  $d$  dimension. The number of total contacts in the system is  $NZ/2$  (we take double counting into account). A single particle needs at least  $d$  equations of the force balance to maintain its position, which means that in total, at least  $Nd$  equations are required to stabilize the configuration of the entire system. Therefore, the condition of the marginal stable state is  $NZ/2 = Nd$  and hence  $Z = 2d$  is concluded. This condition is sometimes called *isostaticity*. This argument indicates that jammed states observed in the experiments and simulations are in the marginal stable states, or isostatic. Moreover, it is widely reported that the isostaticity causes other unique properties such the scaling law around  $\varphi_J$ .

#### 1.4.2 How is the jamming transition related to the glass transition?

Although the jamming transition looks very similar to the glass transition in that both phenomena are characterized by dynamical arrest and random configurations of the constituent particles, a essential difference exists between these transitions. As we have explained, the target systems of the jamming transition are athermal particles like grains and pinballs, which means the systems are not affected by thermal fluctuations. In other words, contrary to the glass transition, the temperature does not play a role in the jamming transition.

Here we have a fundamental question. How are these two transitions related to each other? One

may naively think that the jamming transition is nothing but a *zero temperature glass transition*. This scenario sounds intuitively reasonable, since essential difference between these two transitions is the presence/absence of the thermal fluctuations. This scenario can be illustrated as a phase diagram in the temperature-density-load axes, which is shown in Fig. 1.8 [25]. In this figure, the load means some kind of external perturbations such as shear stress. In the jamming phase diagram,  $\varphi_J$  is uniquely determined as a special (zero temperature) point of the glass transition.

However, recent computer simulation studies show that  $\varphi_J$  varies depending on packing protocols such as the compression rate [22, 26]. For example, if we compress the spheres slowly,  $\varphi_J$  increases above 0.64 with random configurations. These observations imply that the jamming phase diagram can not capture entire physics of the jamming transition. In this thesis, we try to understand the relation between the glass and jamming transitions based on the RFOT picture. This is the third topic of the thesis discussed in Chap. 4.

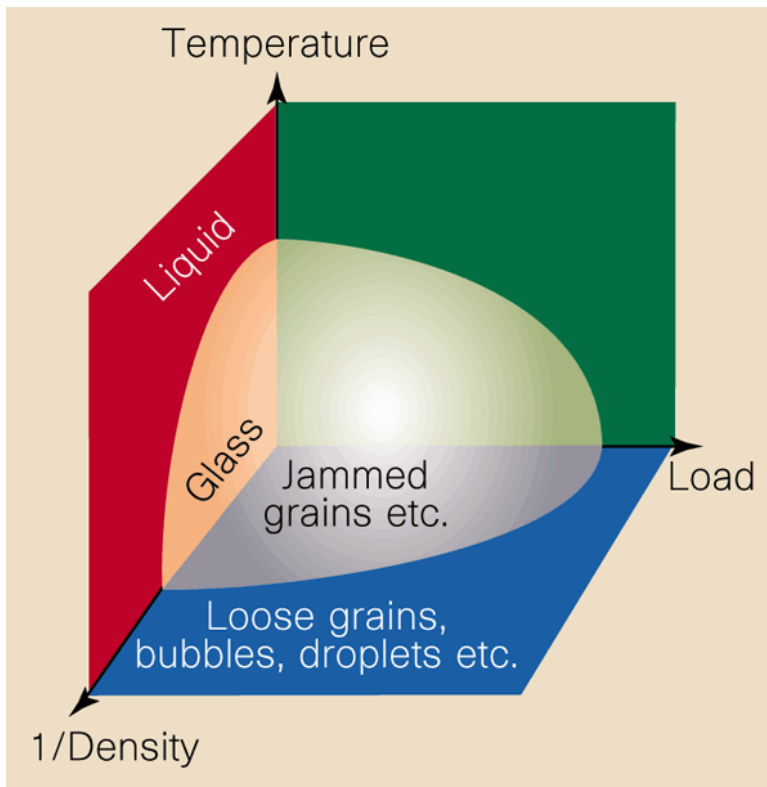


Figure 1.8: Schematic plot of the jamming phase diagram. This figure is from J. Liu and SR. Nagel. *Nature*, 396(6706):21-22, 1998 [25].

## 1.5 Targets of the thesis

In the previous sections, we have briefly explained the glass and jamming transitions and their properties. Also, we mentioned fundamental problems in the field, the origin of super-Arrhenius behavior, the existence of the ideal glass transition, and the relation between the glass and jamming transitions. In this thesis we investigate these problems by using the computer simulations. The organization of the thesis is following. In Chap. 2, we investigate the origin of super-Arrhenius behavior. In Chap. 3, we study the issue of the ideal glass transition. In Chap. 4, we try to understand the relation between the glass and jamming transitions. Finally, we summarize our results and discuss future works and perspectives in Chap. 5. Before that, we explain an overview of the methods of the simulation study in the next section.

## 1.6 Computer simulation of glassy systems

We use computer simulations to investigate the three topics in this thesis. In this section, we briefly explain basic concepts and methods of the computer simulation [27]. More details of the methods for each topic will be explained in each Chapter.

### Interaction potential

The interaction between particles are modeled by potential functions. In the glass transition study, two body interaction potential is preferable since its simplicity enables us to investigate the essence of the thermodynamic and dynamic properties. In addition, the simple potentials are useful to compare simulation results with theoretical predictions.

In Fig. 1.9, we show three representative two body interaction potentials  $v(r)$  often used in the glass transition studies; the hard-sphere (HS) potential, the soft-sphere (SS) potential, and the Lennard-Jones (LJ) potential. The HS potential is the simplest potential among the three and defined by

$$v(r) = \begin{cases} \infty & (r \leq \sigma) \\ 0 & (r > \sigma), \end{cases} \quad (1.6.1)$$

where  $\sigma$  is the diameter of a particle. The HS potential is often used as a model potential for the colloidal glass former. It is also used as athermal granular materials such as grains and pinballs. The SS potential is defined by

$$v(r) = \epsilon \left( \frac{\sigma}{r} \right)^{12}, \quad (1.6.2)$$

where  $\epsilon$  is energy scale. The SS potential is literally softer than the HS potential since the potential allows particles to overlap slightly. The SS potential is also used as a model of the colloidal glass former. The LJ potential is an empirical potential defined by

$$v(r) = 4\epsilon \left[ \left( \frac{\sigma}{r} \right)^{12} - \left( \frac{\sigma}{r} \right)^6 \right]. \quad (1.6.3)$$

According to convention, we put the number, 4, in front of the energy scale  $\epsilon$ . The LJ potential is often used to model atomic or molecular glass formers.

Notion of relevant control parameter should be emphasized here. The thermodynamic properties of the SS and the LJ systems can be characterized both the temperature and pressure (or density). On the other hand, the temperature does not play any role for the HS system, since the potential energy conjugate to the temperature is only either 0 or  $\infty$ . The temperature only plays a role of a time unit which is defined by the averaged kinetic energy. Thus, the relevant control parameter for the HS systems is pressure (or density) alone.

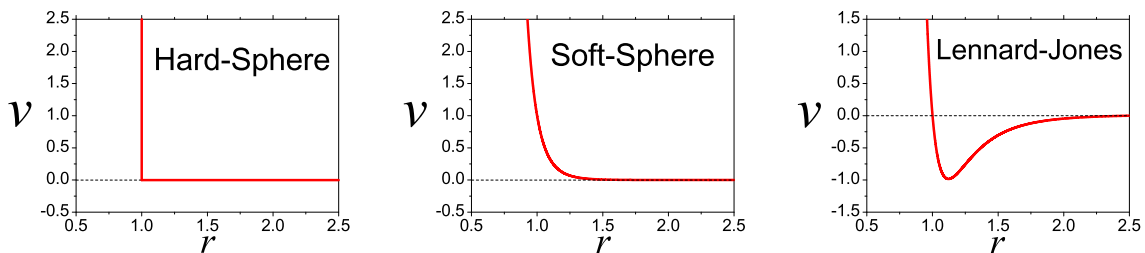


Figure 1.9: Three representative two body interaction potentials commonly used in the glass transition study. The left, middle and right panels are the hard-sphere, the soft-sphere and the Lennard-Jones potentials respectively.

## Polydispersities

To simulate the model glass formers in the supercooled and glass states, we have to put a certain frustration in them in order to avoid the crystallization. The monotonic (one-component) system quickly freezes to a crystal state when the temperature (or pressure) is lowered (or raised). One useful method is to introduce the size disparities of the particles in the systems. The simplest way is to use the binary (two-component) system instead of the monotonic system. Another methods is to make the size of the particles dispersed over a distribution. Particles of different sizes play a role of frustration against crystallization each other.

In this thesis, we mainly use the binary system with different size ratio.

## Integrators

In these settings, the trajectory of the particles is produced by some integrators to calculate the thermodynamic and the dynamic variables. There are two representative integrators; one is the Molecular Dynamics (MD) and another is Monte-Carlo (MC) methods. The MD method integrates the Newton's equation of motion (EOM). Thus, generated trajectories are deterministic. On the other hand, the MC method uses the pseudo-random numbers to move the particles. Thus, the trajectories are essentially stochastic. Originally, the MC method is only used to evaluate the thermodynamic variables since the stochastic trajectories are not true trajectories of the EOM. However, as far as slow dynamics of the supercooled liquid is concerned, it is known that the MC method well reproduces long time scale behavior of the dynamics of the supercooled liquids [28]. The MC method is often more efficient than the MD method to produce the dynamical variables in the same time scale. Therefore, we use the MC method for calculations both the thermodynamic and the dynamic variables.

## Advantage and Shortcoming

Finally, we mention main advantages and shortcomings of the computer simulation compared to the experiments.

- Advantage: The computer simulation allows one to access to the microscopic information of the system. For example, we have already shown the density-density time correlation function,  $F(k, t)$  obtained from the computer simulation in Fig. 1.3. This variable is very useful to describe microscopic dynamical process in supercooled liquids. In principle, we can obtain all coordinates of the particles throughout the computer simulation. Therefore, it allow us to observe any microscopic variables other than  $F(k, t)$ . Moreover, we can design new model systems freely for any purpose. By tuning the interaction potential, we can generate diverse model systems. We adopt this strategy in the first topic of this thesis.

- Shortcoming: A shortcoming of the computer simulation compared to the experiment is the limited time scale available for the simulation. We have mentioned that the empirical glass transition temperature is defined as  $\eta(T_g) = 10^{13}$  poise, which means we have the limit of measurement in experiments. Likewise, the computer simulation has the limit of computational time. Unfortunately, available time scale of computer simulation is about 10 orders of magnitude shorter than the those of the experiment.

The computer simulation and the experiment are complementary to each other. The study of the glass transition has been developed by taking advantages from both sides.

## Chapter 2

# Fragility of Supercooled Liquids

### 2.1 Motivation

The supercooled liquids show dramatic slowing down of the dynamics near empirical glass transition temperature  $T_g$ . By observing the temperature dependence of the relaxation times and the transport coefficients such as the viscosity one sees two distinct characters of the slow dynamics. While the dynamics of some glass formers obey the Arrhenius type temperature dependence like normal liquids, other glass formers show apparent deviation from simple Arrhenius law, *i.e.*, super-Arrhenius behavior. According to the Angell's classification, the glass formers whose dynamics obey the Arrhenius law are called the *strong* glass formers and the ones showing the super-Arrhenius behavior are classified as the *fragile* glass formers [5]. The *fragility* quantifies the extent how the dynamics shows super-Arrhenius behavior [5]. Representative strong glass formers are anisotropic network glass formers such as  $\text{SiO}_2$  and  $\text{GeO}_2$ . On the other hand, o-terphenyl and toluene are typical fragile glass formers. Despite of intensive experimental, numerical, and theoretical studies, the mechanism of the fragility is still unclear. Why does the dynamics of the fragile glass formers deviate from simple Arrhenius law? What is the essential difference between the strong and fragile glass formers? One of the goal of the glass transition study is to answer these questions from microscopic point of view [1, 2, 10].

The computer simulation is an invaluable way to study glassy dynamics since it offers microscopic information of the glass formers [29]. Relatively simple models such as the soft-sphere (SS) potential [30] and the Lennard-Jones (LJ) potential models [7] have been widely performed for the fragile glass formers. These potential models tend to form highly packed and isotropic particle configurations. On the other hand, (anisotropic) network glass formers models [31, 32] have been intensively used for the strong glass formers. These models of the strong and fragile glass formers have been investigated rather independently. In practice, as the experiments have shown, there are variety of glass formers between very strong glass formers ( $\text{SiO}_2$  and  $\text{GeO}_2$ ) and very fragile ones (o-terphenyl and toluene) [5]. To understand the difference between the strong and fragile and the origin of the super-Arrhenius behavior, a simulation model whose fragility can be systematically controlled is desirable.

In the previous studies, several ways to control the fragility of the system have been proposed. They can be classified into as follows. (1) Changing the density of the system [33–35]. (2) Changing the polydispersity, especially, the size ratio in binary systems [36–38]. (3) Tuning softness of the interaction potential or truncating it. [39–42]. (4) Introducing many-body interactions to change frustration against the crystallization [43, 44]. These methods enable us to control the fragility of the simulation models. However, they are of limited or little applicability to understand fully the nature of the fragility. Regarding the method (1), it has been shown that the measured variation of the fragility is only apparent since these results are collapsed into a single curve by a density-temperature scaling [33, 35, 39]. The variation of the fragility by the methods (2) and (3) is very small, and that hardly covers the full range from the strong and fragile glass formers [37, 38, 40, 41]. Finally, the method (4) can reproduce the strong glass behavior very well and tuning the many-body interaction can change the fragility is not difficult, but they use the many-body interaction [43, 44].

In this Chapter, we propose a new simulation model whose fragility can be controlled systemat-

ically. We numerically investigate its structural and dynamical properties. Our model is originated from a model potential recently proposed by Coslovich and Pastore [32]. Coslovich and Pastore (CP) have introduced the potential to mimic the network glass former (strong glass former) without three-body interaction. We modified and generalized in such a way that we can tune the depth of the two-body attraction potential. This model enables us to bridge the gap between an anisotropic network glass former model and an isotropic soft-sphere potential model. This Chapter is organized as follows. In Sec. 2.2, we describe details of the model and the simulation methods we employed. The results of this study will be presented in Sec. 2.3. Finally, we summarize the results and discuss future directions in Sec. 2.4.

## 2.2 Methods

We introduce the modified Coslovich-Pastore (MCP) model in this Chapter. Before describing the MCP model, we briefly explain the original CP model and its properties. The CP model is a simple strong glass former model. Although the model has only two-body simple spherical interaction potentials like the SS and LJ potentials, it exhibits an anisotropic tetrahedral network structure. According to Refs. [45, 46], there are three conditions for a binary mixture with spherical potential to be able to form the tetrahedral network structure; (1) The composition ratio is  $N_1 : N_2 = 1 : 2$ , where  $N_1$  and  $N_2$  are the number of particles for species 1 and 2 respectively. (2) The potential should be non-additive. In other words, the range of the interaction between the species 1 and 2 is not the simple sum of their diameters. (3) The attractive interaction between different species should be strong. The CP model satisfies these conditions and hence the model reproduces the structural properties of well established  $\text{SiO}_2$  model [31].<sup>1</sup> Recently, the CP model has been intensively investigated to understand the properties of the strong glass former [47–49]

Here we describe the details of the MCP model. The model is a binary mixture in three dimensions whose composition ratio is  $N_1 : N_2 = 1 : 2$ . The mass ratio is  $m_2/m_1 = 0.57$ . The interaction potentials between two particles are given by

$$\left\{ \begin{array}{l} v_{11}(r) = \epsilon_{11} \left( \frac{\sigma_{11}}{r} \right)^{12}, \\ v_{12}(r) = \epsilon_{12} \left[ \left( \frac{\sigma_{12}}{r} \right)^{12} - C \left( \frac{\sigma_{12}}{r} \right)^6 \right], \\ v_{22}(r) = \epsilon_{22} \left( \frac{\sigma_{22}}{r} \right)^{12}. \end{array} \right. \quad (2.2.1)$$

We set  $\epsilon_{12}/\epsilon_{11} = 24$ ,  $\epsilon_{22}/\epsilon_{11} = 1$  and  $\sigma_{12}/\sigma_{11} = 0.49$ ,  $\sigma_{22}/\sigma_{11} = 0.85$ .  $v_{\alpha\beta}(r)$  ( $\alpha, \beta \in \{1, 2\}$ ) is truncated at  $r = 2.5\sigma_{\alpha\beta}$  and the switching function<sup>2</sup> is used up to  $r = 3\sigma_{\alpha\beta}$ . In the original CP model, the particles belonging to the species 1 and 2 correspond to Si and O atoms respectively. In the following, we will use  $\epsilon_{11}$ ,  $\sigma_{11}$ , and  $\sqrt{m_1\sigma_{11}^2/\epsilon_{11}}$  as the units of energy, length, and time, respectively. We set  $k_B = 1$ . We introduce a coefficient  $C$  in the second term (the attraction part) in  $v_{12}(r)$ . This is the only modification of the original CP model. Indeed,  $C = 1$  corresponds to the original CP model. The physical meaning of  $C$  is a magnitude of the attraction potential between different species. The depth of the potential well  $\Delta$  is written as  $\Delta = \epsilon_{12}C^2/4$ .  $\Delta = 6$  for the original CP model. Hereafter, we use  $\Delta$  to characterize the MCP model instead of  $C$ . As we have mentioned,

<sup>1</sup>The van-Beest-Kramer-van Santen (BKS) model is a well-established  $\text{SiO}_2$  model [31]. Although the model uses only two-body potential, its functional form has long range interaction term. Thus, one needs a computationally demanding procedure such as the Ewald method to evaluate the potential.

<sup>2</sup>The switching function  $S(r)$  connects two points,  $R_1$  and  $R_2$ , continuously and is defined as

$$S(r) = \begin{cases} 1 & (0 \leq r < R_1) \\ (r - R_2)^2(2r + R_2 - 3R_1)/(R_2 - R_1)^3 & (R_1 \leq r < R_2) \\ 0 & (R_2 \leq r) \end{cases} \quad (2.2.2)$$

Its derivative,  $dS(r)/dr$  is also a continuous function.

large  $\Delta$  leads to the tetrahedral network structure. Thus, the tetrahedral network structure shown in the original CP model will be broken gradually when  $\Delta$  is decreased. Then an isotropic structures are recovered at  $\Delta = 0$ , where the potential reduces to the SS. In other words, we can connect the CP model ( $\Delta = 6$ ) with purely repulsive SS potential system ( $\Delta = 0$ ) continuously. In Fig. 2.1, we show  $v_{12}(r)$  for several  $\Delta$ 's. Note that the MCP model at  $\Delta = 0$  limit is slightly different from the conventional SS model [30] because the range of the interaction is still non-additive.

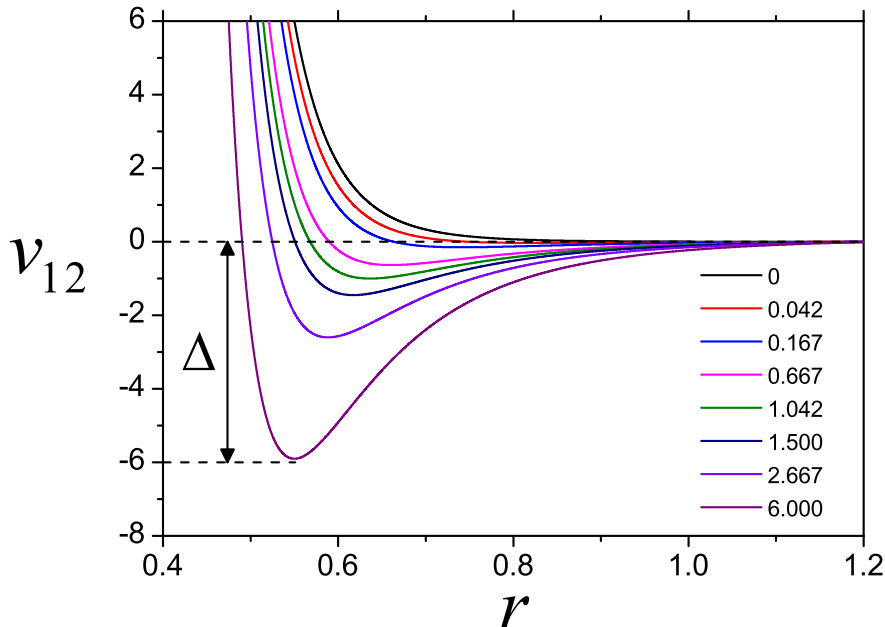


Figure 2.1: The interaction potential between species 1 and 2.  $\Delta = 0$  at the top to  $\Delta = 6$  at the bottom. The original CP model has  $\Delta = 6$ .

In these settings, we perform the molecular dynamics (MD) simulations for several  $\Delta$ 's to confirm the above speculation. We use  $\Delta = 6, 2.667, 1.5, 1.042, 0.167, 1.042, 0.042$  and  $0$  in this study. Simulations are performed at constant density  $\rho = 1.655$ . The number of the particles is  $N = N_1 + N_2 = 3000$ . The *NVE* MD method is used to produce the trajectories. To calculate dynamic properties, we average over four independent simulation runs.

## 2.3 Results

In this Section, we show our results. First, static properties are presented. Then, dynamical properties are shown. Finally, the relation between the static and dynamic properties are discussed.

### 2.3.1 Structural properties

Here we show structural properties of the MCP model. Particularly, we demonstrate that by changing  $\Delta$  from 6 to 0, the local structure changes from a tetrahedral network to an isotropic structure. To characterize the structural properties of the system, we use the radial distribution function  $g(r)$  defined by

$$g(r) = \frac{1}{\rho N} \left\langle \sum_{i=1}^N \sum_{j \neq i}^N \delta(\mathbf{r} - (\mathbf{r}_i - \mathbf{r}_j)) \right\rangle. \quad (2.3.1)$$

$g(r)$  measures the distribution of the neighboring particles at distance  $r$  for a particle at origin. Since the MCP model is a binary mixture, there are three combinations of correlations of particles,  $g_{11}(r)$ ,

$g_{12}(r)$ , and  $g_{22}(r)$  [4]. Fig. 2.2 shows the radial distribution functions for several  $\Delta$ 's. For  $\Delta = 6$  (see Fig. 2.2(g)),  $g_{12}(r)$  has a very sharp peak at  $r \simeq 0.6$  followed by very small value at the first minimum at  $r \simeq \sigma_{11}$  and  $r \simeq \sigma_{22}$  where the first-peak of  $g_{11}(r)$  and  $g_{22}(r)$  are observed. This is an indication that the atoms of species 1 and 2 form a tetrahedral network structure [32, 50]. However, when  $\Delta$  is decreased, the first peak of  $g_{12}(r)$  decreases and broadens, leading to the finite values of the first minimum. Eventually, at  $\Delta = 0$ , the shape of all  $g_{12}(r)$ ,  $g_{11}(r)$ , and  $g_{22}(r)$  becomes similar to those of typical fragile glass formers [7, 30]. This indicates that the bond between species 1 and 2 is weakened by decreasing  $\Delta$ .

To understand the effect of  $\Delta$  on the structure in more detail, we calculate the coordination number  $z_{\alpha\beta}$ .  $z_{\alpha\beta}$  is the averaged number of  $\beta$  particles in the first neighbor shell of a  $\alpha$  particle and defined by

$$z_{\alpha\beta} = \rho_{\beta} \int_0^{r_{\alpha\beta}^*} dr 4\pi r^2 g_{\alpha\beta}(r), \quad (2.3.2)$$

where  $\rho_{\beta}$  is the number density of species  $\beta$  and  $r_{\alpha\beta}^*$  is the position of the first minimum in  $g_{\alpha\beta}(r)$ . Especially,  $z_{12}$  and  $z_{11}$  are useful to characterize the tetrahedral network structure [50]. In  $\text{SiO}_2$ , a single Si atom (species 1) is surrounded by four O atoms (species 2), forming a tetrahedron. Therefore,  $z_{12} = 4$  and  $z_{21} = 2$  are concluded. Each O atom is also bonded with Si atoms to form connected chains tetrahedra, and thus  $z_{11} = 4$ .

In Fig. 2.3, we show  $z_{11}$  and  $z_{12}$  at the lowest temperature for each  $\Delta$ . We use  $\sqrt{\Delta}$  instead of  $\Delta$  simply because to see data clearly. At  $\Delta = 6$  ( $\sqrt{\Delta} \simeq 2.45$ ),  $z_{11} = 4$  and  $z_{12} = 4$  indeed hold, *i.e.*, perfect tetrahedral network structures are formed [32, 50]. As  $\Delta$  decreases, both  $z_{11}$  and  $z_{12}$  increase. Eventually, they become  $z_{11} \simeq 14$  and  $z_{12} \simeq 9$  at  $\Delta = 0$ . This indicates that the network structure is broken. Then, the system becomes more isotropic and has compact configurations by decreasing  $\Delta$ . Here we make two remarks. First, the crystallization takes place at  $\Delta = 0.667$  ( $\sqrt{\Delta} \simeq 0.817$ ) at low temperatures. We show the coordination numbers for the crystalline state by open symbols in Fig. 2.3. The crystal structure has  $z_{12} = 6$  and  $z_{11} \simeq 11$ . They suggest that the observed crystalline structure is Stishovite-like. Indeed, the real  $\text{SiO}_2$  forms Stishovite structure at very high pressure [51]. Second, we observe in Fig. 2.3 an exceptionally large value of  $z_{11}$  ( $\simeq 15$ ) at  $\Delta = 1.042$  ( $\sqrt{\Delta} \simeq 1.021$ ). This is due to the ambiguity to define the first coordination shell. As we see in Fig. 2.2(h), the shape of  $g_{11}(r)$  qualitatively changes around  $\Delta \simeq 1$ , which makes the clear-cut definition of  $r_{11}^*$  difficult. Thus,  $\Delta \simeq 1$  can be regarded as the crossover regime from the network dominated region to the isotropic-compact structure region.

Next we observe the static structure factor  $S(k)$ . As we have explained in Chap. 1,  $S(k)$  is the density correlation function at  $t = 0$  limit,  $S(k) = F(k, t = 0)$ , or a Fourier transform of  $g(r)$ ,

$$S(k) = 1 + \rho \int_0^{\infty} dr 4\pi r^2 (g(r) - 1) \sin(kr)/kr. \quad (2.3.3)$$

In the experiment,  $S(k)$  can be observed in the diffraction measurements. In binary mixtures,  $S(k)$ , as well as  $g(r)$ , has three components,  $S_{11}(k)$ ,  $S_{12}(k)$ , and  $S_{22}(k)$ . We show these components in Fig. 2.4 for several  $\Delta$ 's.

In general, the maximum peak observed in all components of the static structure factor corresponds to a first-peak of  $g(r)$  neighboring particles. The peak position in the wave number corresponds to a distance between a particle and its neighbors. At  $\Delta = 6$ , the original CP model, we observe the maximum peaks around  $k \simeq 8$ , which indicates the tetrahedra are formed in the length scale of  $2\pi/k \simeq 0.79$ . We also recognize weaker peaks at lower wave numbers around  $k \simeq 5$ . This is called the first sharp diffraction peaks (FSDP). The FSDP is known to be an indication that there exists certain structural patterns often called the medium-range order (MRO) at a length scale larger than the neighbor shell. In the tetrahedral network systems, the FSDP can be understood as the result of clustering of the tetrahedra [52]. This FSDP suggests that the structure of the network fluid is hierarchical, *i.e.*, tightly bonded tetrahedra are building blocks at short lengths, and the clusters of these tetrahedra form at larger lengths. However, when  $\Delta$  is decreased, these two peaks merge and become a single peak, indicating such hierarchical structure is broken gradually. At  $\Delta \lesssim 1$ , the static structure

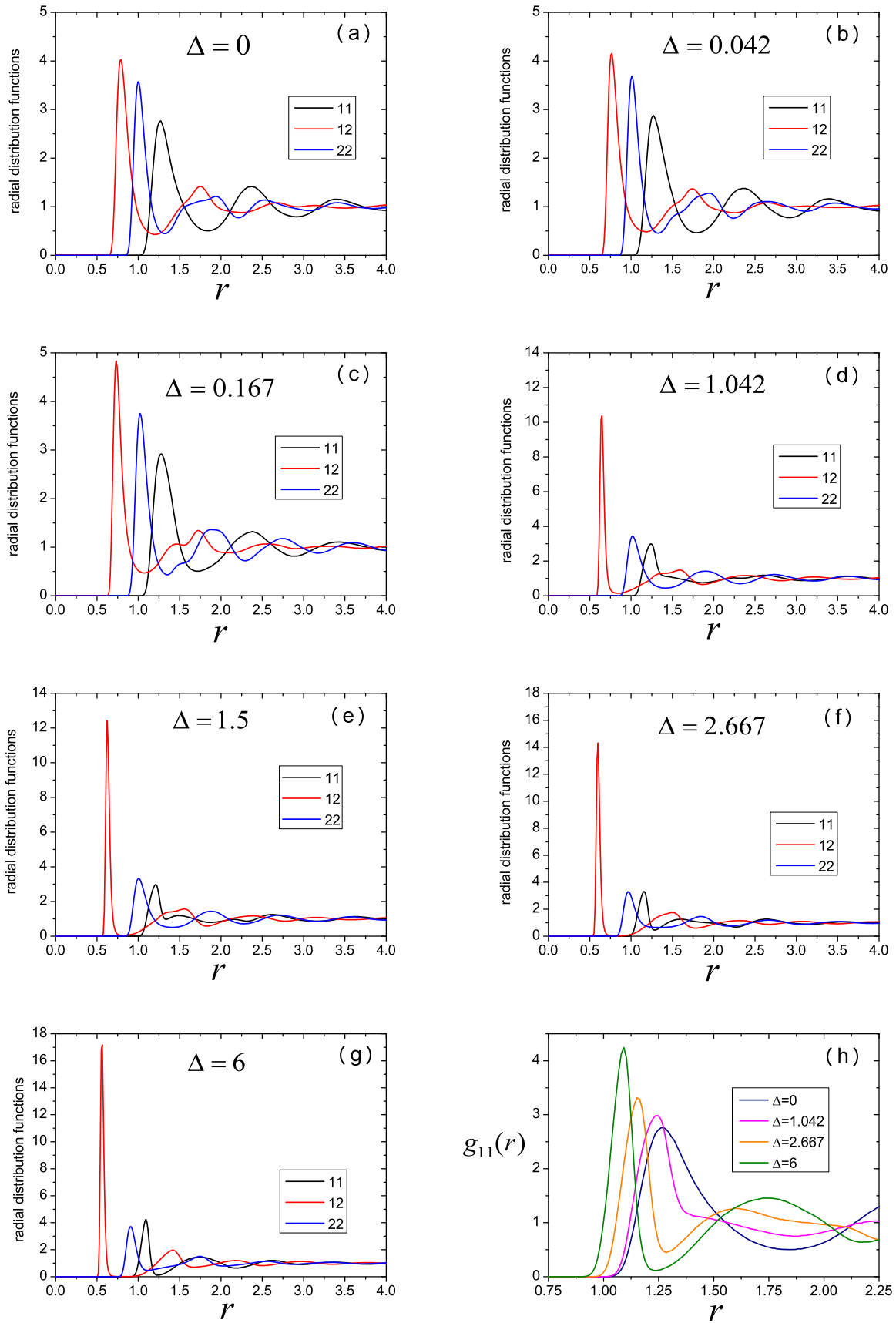


Figure 2.2: (a) - (g) The radial distribution functions,  $g_{11}(r)$ ,  $g_{12}(r)$ , and  $g_{22}(r)$ , for each  $\Delta$ . (h)  $g_{11}(r)$  for several  $\Delta$ 's are plotted. Note that the scales of y-axes are not fixed for each panel. The lowest temperature data we simulated are shown in (a)-(h).

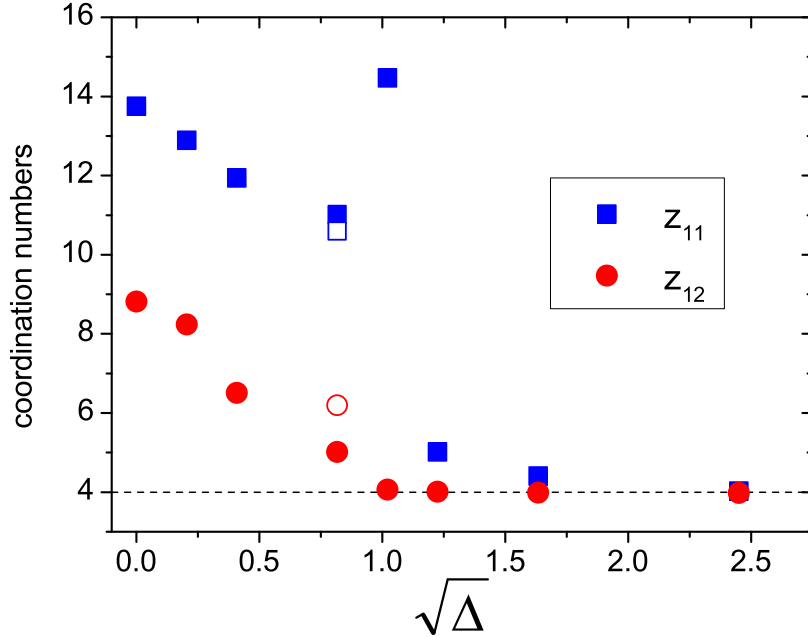


Figure 2.3: The coordination numbers  $z_{11}$  and  $z_{12}$ . The lowest temperature data are shown for each  $\Delta$ . Both the liquid state and the crystal state are shown by the filled symbols and the open symbols respectively for  $\Delta = 0.667$  ( $\sqrt{\Delta} \simeq 0.8167$ ). The original CP model locates on  $\Delta = 6$  ( $\sqrt{\Delta} \simeq 2.45$ ).

factors in analogous to those observed in typical fragile glass formers [6, 53]. The  $\Delta$  dependence of  $S_{11}(k)$  is shown in Fig. 2.4(h). From the figure, we can also understand the fact that the structures of the system qualitatively changes across  $\Delta \simeq 1$ .

### 2.3.2 Dynamic properties

From the above analyses, we have found that as  $\Delta$  is decreased from the value of the original CP model, the bond between species 1 and 2 are weakened and the tetrahedral networks are broken, and eventually, more isotropic structure is formed. Do dynamic properties, especially the fragility, change as the structural changes? In this subsection, we investigate the dynamic properties of the MCP model.

Here we present the temperature dependence of the relaxation time and the self diffusion constant. We define the relaxation time  $\tau_1$  of the system by  $F_s(k, \tau_1) = e^{-1}$ .  $F_s(k, t)$  is the self part of the density correlation function for species 1 [4] and defined by

$$F_s(k, t) = \frac{1}{N} \sum_{i=1}^N \left\langle e^{-i\mathbf{k} \cdot (\mathbf{r}_i(t) - \mathbf{r}_i(0))} \right\rangle, \quad (2.3.4)$$

where  $\mathbf{r}_i$  is the particle coordinate. As we explained in Chap. 1, the density time correlation function is a basic observable to discuss the glassy dynamics. In Fig. 2.5, we show  $F_s(k, t)$  for several  $\Delta$ 's at various temperatures where glassy slow dynamics are observed. To compute  $F_s(k, t)$ , we fix  $k$  at the peak position of the static structure factor,  $S_{11}(k)$ . The peak positions  $k$  we used are summarized in Table 2.1. At high temperatures, for each  $\Delta$ ,  $F_s(k, t)$  shows the exponential decay and rapidly relax to zero. However, at low temperatures, the functional forms are stretched, showing the two-step relaxation which is a sign of the glassy dynamics. Therefore, the relaxation time scale  $\tau_1$  is increasing with decreasing the temperature. The temperature dependence of  $\tau_1$  are plotted in Fig. 2.6(a).

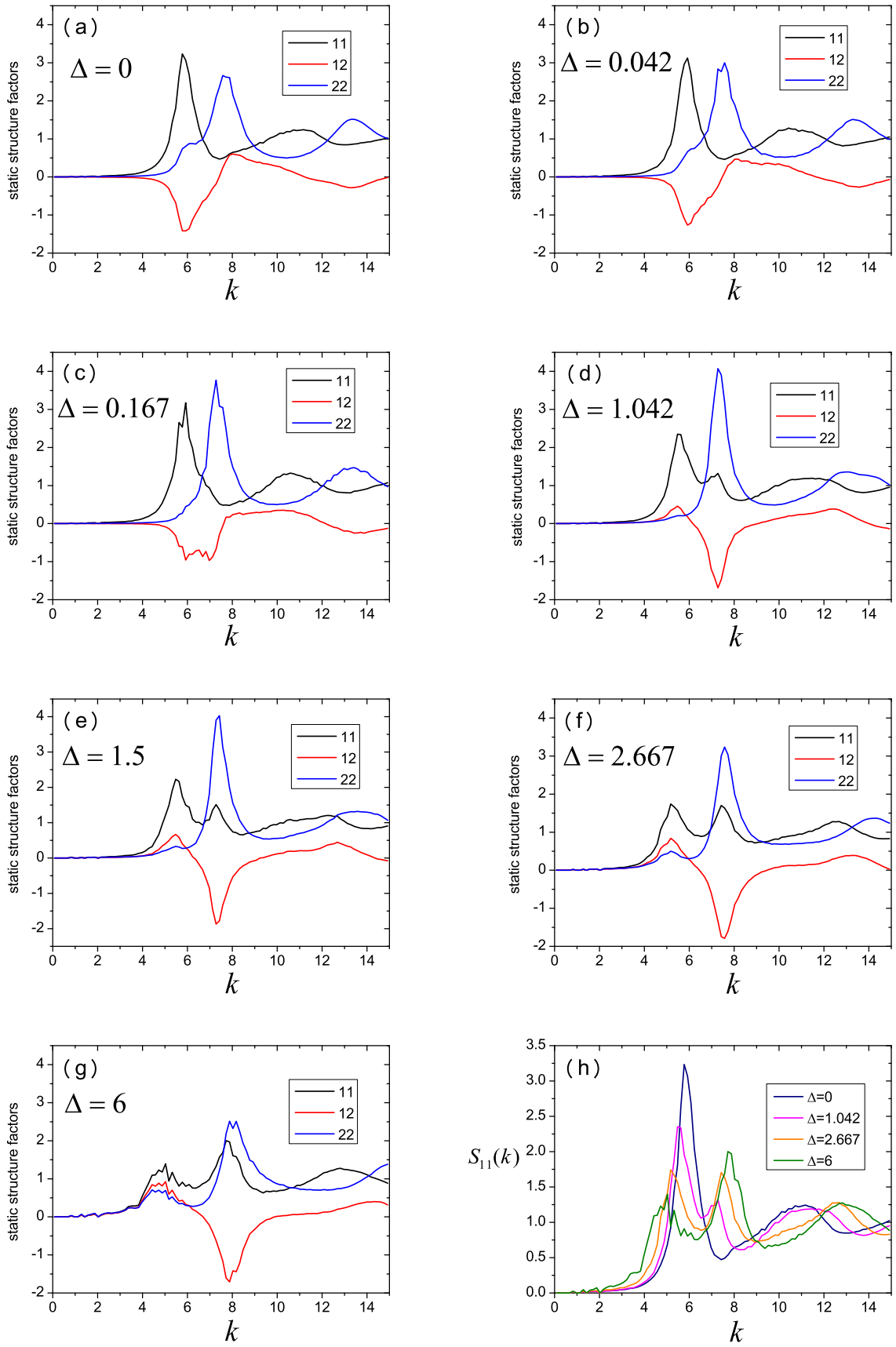


Figure 2.4: (a) - (g) The static structure factors,  $S_{11}(k)$ ,  $S_{12}(k)$ , and  $S_{22}(k)$ , for each  $\Delta$ . (h)  $S_{11}(k)$  for several  $\Delta$ 's are plotted.

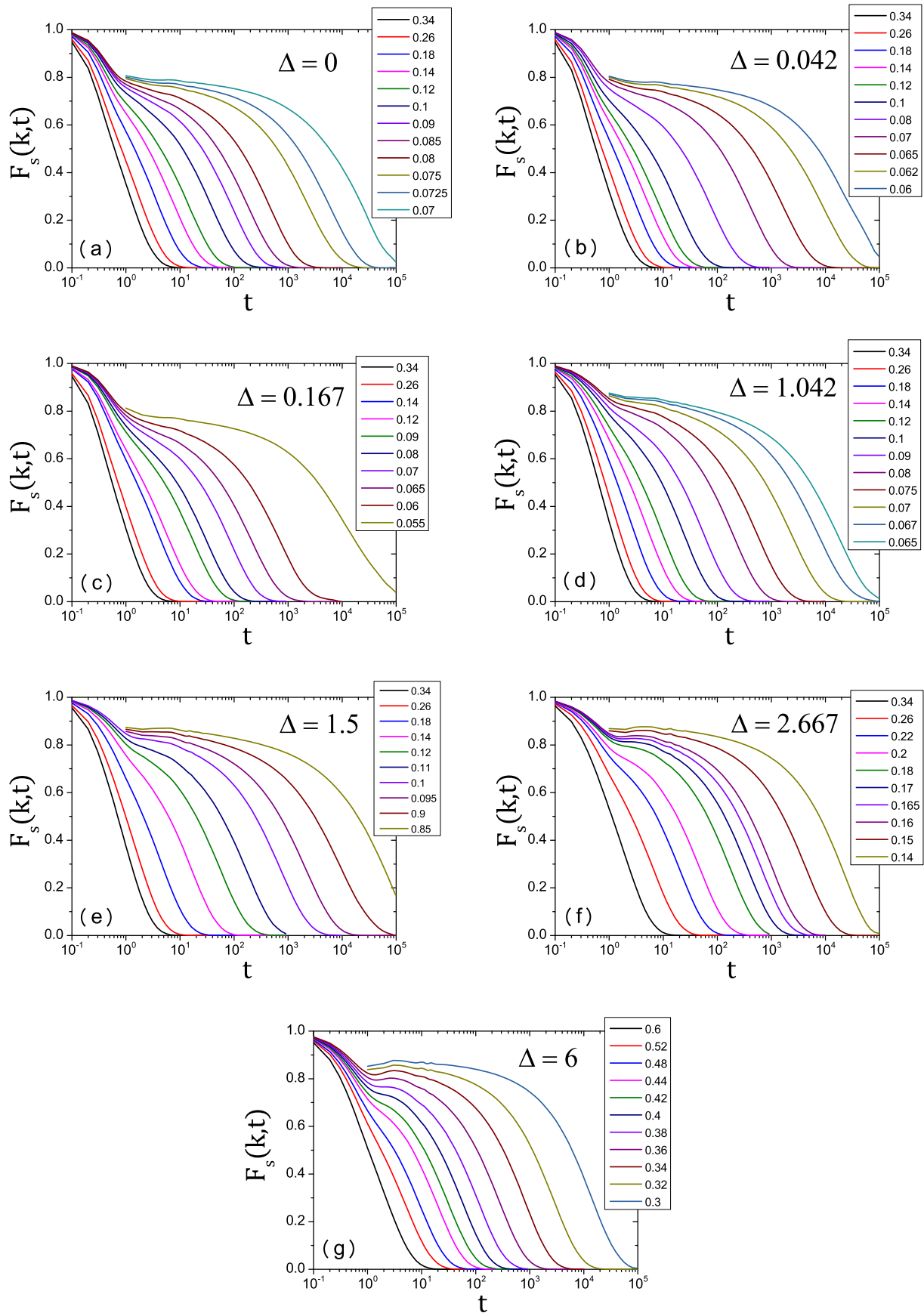


Figure 2.5: The self part of the density correlation function for species 1. The legends show the temperatures we simulated for each  $\Delta$ .

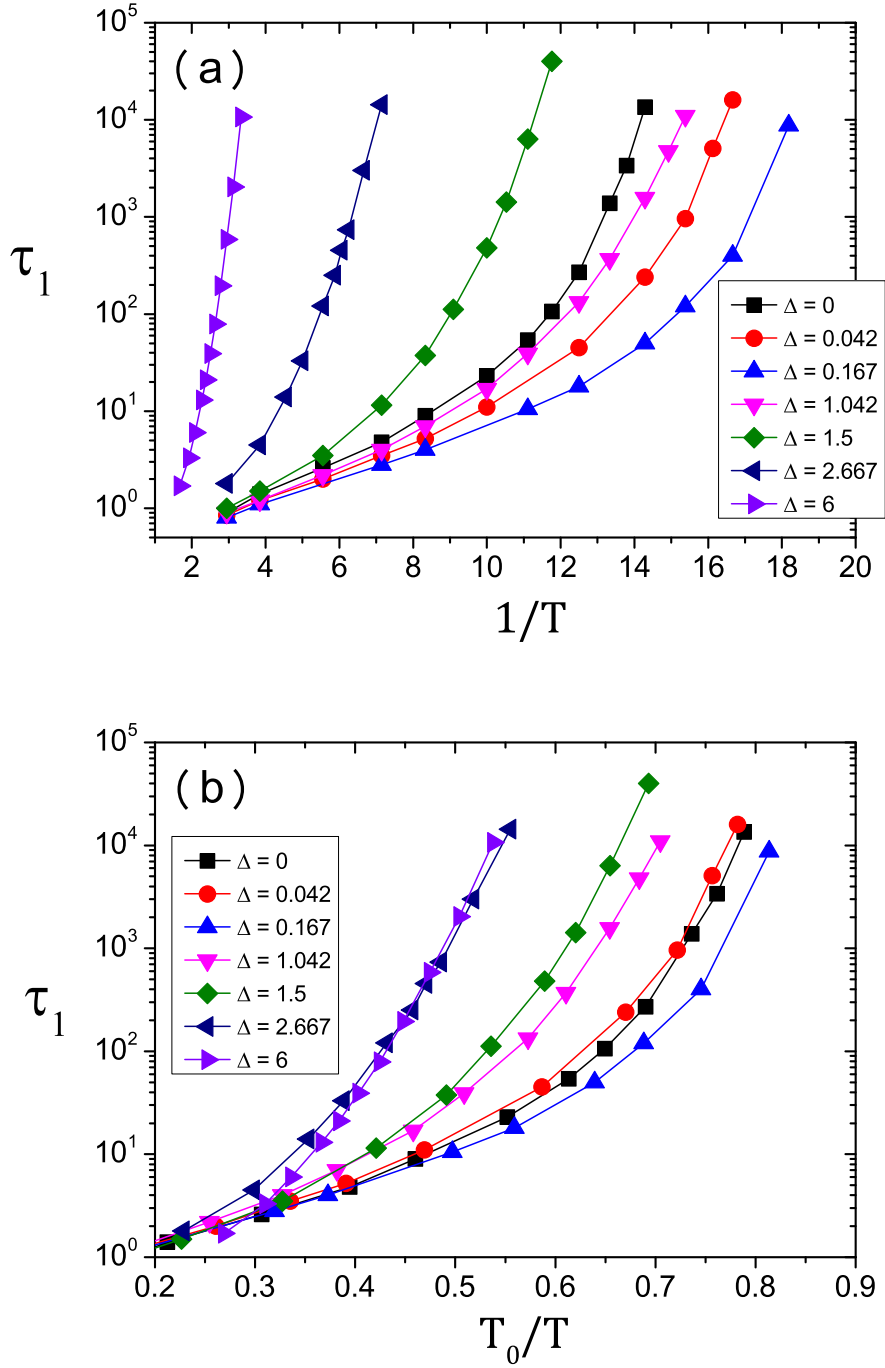


Figure 2.6: The Arrhenius plots of the relaxation time. (a) Data are plotted as a function of the inverse temperature  $1/T$ . (b) The temperature is scaled by  $T_0$ , a fitting parameter of the VFT equation.

$\Delta$	peak position $k$	$T^*$	$T_0$ from $\tau_1$	$T_0$ from $D_1^{-1}$
0	5.8	0.14	0.0552	0.0522
0.042	5.9	0.14	0.0469	0.0438
0.167	5.9	0.12	0.0447	0.0414
1.042	5.6	0.12	0.0458	0.0423
1.5	5.5	0.14	0.0589	0.0544
2.667	5.2	0.26	0.0777	0.0733
6	5.0	0.48	0.161	0.164

Table 2.1: The peak position  $k$  of  $S_{11}(k)$  to compute  $Fs(k, t)$ , the onset temperature  $T^*$  of the two-step relaxation, and  $T_0$  obtained by fitting of the VFT equation.

To quantify the degree of the super-Arrhenius behavior, or the fragility, we use the VFT equation,

$$\tau_1 \propto \exp \left[ \frac{1}{K(T/T_0 - 1)} \right]. \quad (2.3.5)$$

A fitting parameter,  $K$ , is the fragility of the system [10]. In general, the VFT equation fits data well at relatively low temperatures. Thus, we use data points below  $T^*$  for the fitting at which the two-step relaxation of  $Fs(k, t)$  set in.  $T^*$  for each  $\Delta$  is summarized in Table 2.1. Another fitting parameter,  $T_0$ , is used as a characteristic temperature to scale the temperature  $T$  in Fig. 2.6(a). This scaling enable us to see whether the dynamics is the Arrhenius like or not. The obtained rescaled plot is shown in Fig. 2.6(b). At the original CP model ( $\Delta = 6$ ), a straight line is observed except very high temperature region as shown in Fig. 2.6(b). This indicates that the system indeed obeys the Arrhenius law [32, 50]. However, as decreasing  $\Delta$ ,  $\tau_1$  deviates from the straight line, showing super-Arrhenius behavior.  $K$  obtained from Fig. 2.6(b) as a function of  $\Delta$  is shown in filled squares in Fig. 2.7.  $K$  increases with decreasing  $\Delta$ , and eventually exceeds the value of a typical fragile glass former shown in the allow in Fig. 2.7. This clearly demonstrates that the fragility of the MCP model is indeed controlled by  $\Delta$  from the strong to the fragile.

Qualitatively similar behavior is observed for the self diffusion constant. The diffusion constant  $D_\alpha$  ( $\alpha, \beta \in \{1, 2\}$ ) is obtained by the mean squared displacement (MSD) at long time,  $\langle |\mathbf{r}(t) - \mathbf{r}(0)|^2 \rangle \sim 6D_\alpha t$  ( $t \gg 1$ ). The MSD at two limiting cases,  $\Delta = 6$  and  $\Delta = 0$ , are presented in Fig. 2.8. Fig. 2.9(a) is the Arrhenius plot of  $D_1^{-1}$ . The same data plotted against the scaled temperature is shown in Fig. 2.9(b).  $K$  is also obtained from  $D_1$  by using the same manner as  $\tau_1$  and plotted in filled circles in Fig. 2.7.  $K$  from  $D_1$  has a lower value than  $K$  from  $\tau_1$  as shown in Fig. 2.7. However, the overall behavior is qualitatively same.

In order to probe more details of microscopic dynamics at molecular level, we evaluate the ratio of the diffusion constants  $D_2/D_1$ . In  $\text{SiO}_2$  experiments, it has been reported that the diffusion constants for Si and O atoms decouple when the temperature is lowered [54]. To be specific, the ratio  $D_O/D_{\text{Si}}$  increases with decreasing the temperature. Eventually, it becomes about two orders of magnitude near  $T_g$ . This decoupling between  $D_{\text{Si}}$  and  $D_O$  has been also observed in simulations [55, 56]. According to Ref. [56], the decoupling is attributed to a rotational motion of O atom in the tetrahedral structure. In Fig. 2.10, we show  $D_2/D_1$  as a function of  $\tau_1$  for several  $\Delta$ 's. For the original CP model, we confirm that  $D_2/D_1$  increases with increasing  $\tau_1$ , or decreasing the temperature [32]. Fig. 2.10 shows that the growth of  $D_2/D_1$  becomes milder as  $\Delta$  increases and the trend even becomes opposite, *i.e.*,  $D_2/D_1$  decreases at  $\Delta = 0.167$ . Surprisingly, if  $\Delta$  increases beyond  $\Delta = 0.167$ , the trend is reversed, *i.e.*, the decoupling is enhanced again and the growth of  $D_2/D_1$  becomes stronger as  $\Delta$  increases continuously to the target value  $\Delta = 6$ . The extent of the decoupling is much weaker compared to  $\Delta = 0$  case at the same  $\tau_1$ . Such huge decoupling of  $D_1$  and  $D_2$  for the fragile glass former has been reported in a previous study of the SS potential model [57]. We speculate the mechanism of the decoupling at  $\Delta = 0$  is different from that at  $\Delta = 6$ , and it originate from the different structural motifs of the two species in locally packed geometry, often called the correlated rearrange regions (CRR) in the

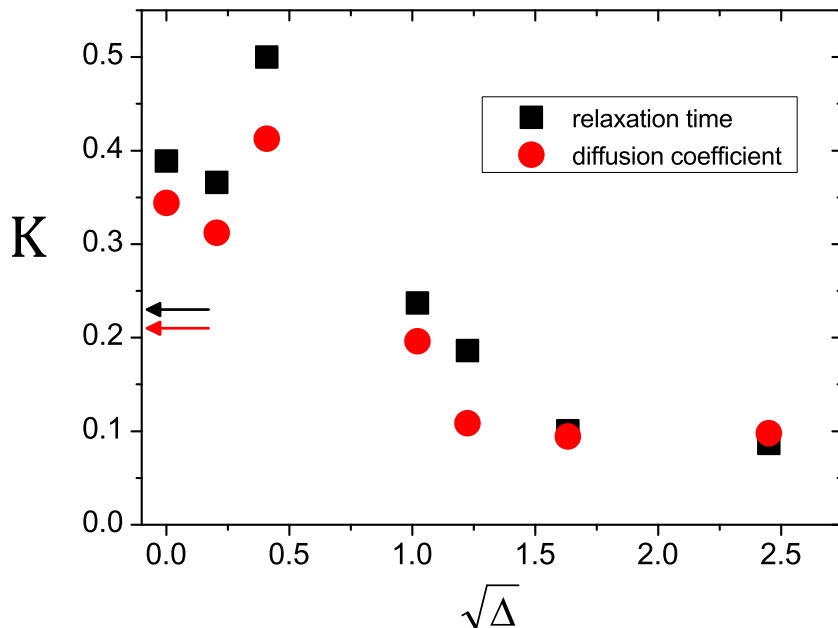


Figure 2.7: The fragility  $K$  as a function of  $\Delta$ . The results of the VFT fitting from  $\tau_1$  and  $D_1^{-1}$  are shown as the square and circle points respectively. The results of the KA mixture are shown by horizontal arrows from Sengupta *et al.*, [41]. The black and red arrows indicate  $K$  from the relaxation time and the self diffusion constant respectively.

original Adam-Gibbs argument [58]. However, further investigation is needed to clarify this behavior quantitatively. Anyway, the non-monotonic behavior of  $D_2/D_1$  with decreasing  $\Delta$  indicates that the relaxation process of the MCP model qualitatively changes when  $\Delta$  is lowered.

### 2.3.3 Dynamical heterogeneities

As we discussed in Chap. 1, the distinct features of the dynamics of the supercooled liquids are not only dramatic slowing down but also a heterogeneous dynamical pattern of mobile and immobile particles which is called the dynamical heterogeneities (DH) [15]. It is empirically known that the fragile glass formers show more pronounced DH than the strong glass formers. According to a phenomenological argument in Appendix A, this is intuitively accepted since the CRR grows more quickly in the fragile glass formers than the strong ones as the temperature is lowered. Here we explore the DH of the MCP model to investigate the relation between the fragility and the DH. To characterize the DH, we evaluate the non-Gaussian parameter (NGP) and then examine the Stokes-Einstein (SE) violation.

In general,  $F_s(k, t)$  becomes almost a Gaussian function in  $k$  for fixed  $t$  at high temperatures like normal liquids [4]. Thus, its Fourier transform of it also becomes a Gaussian function. This function, often denoted as  $G_s(r, t)$ , is referred to as the van-Hove function. The van-Hove function represents the distribution of a particle displacement of atoms at time  $t$  from its definition,

$$G_s(r, t) = \sum_{i=1}^N \langle \delta(|\mathbf{r}_i(t) - \mathbf{r}_i(0)| - r) \rangle. \quad (2.3.6)$$

However, as the temperature is lowered and the system enters the supercooled state, these functions progressively deviate from the Gaussian. It is widely accepted that this non-Gaussianity is a distinct reflection of the DH [15]. Indeed, simulation studies have demonstrated that the coexistence of the mobile and immobile clusters result in the broader distribution of particle displacements. Thus, the

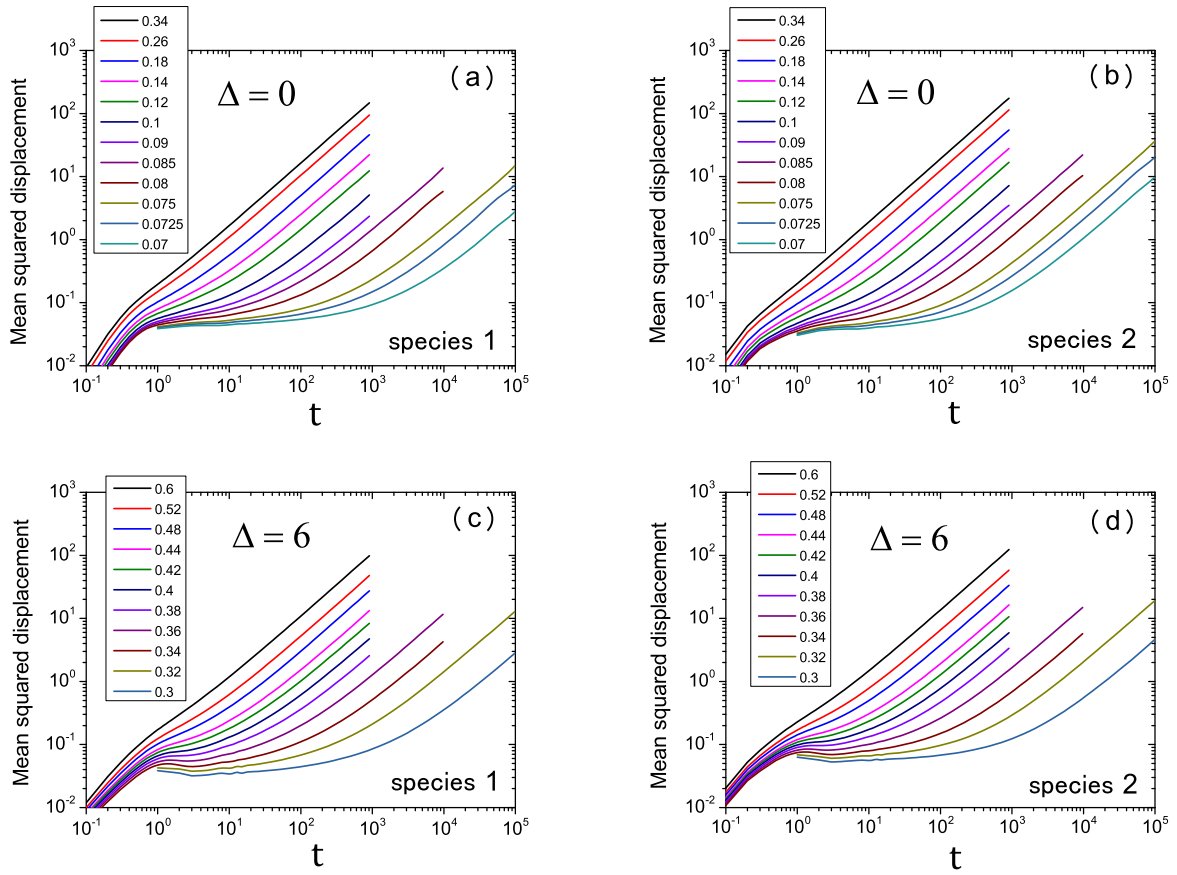


Figure 2.8: The mean squared displacement of the particles belonging to species 1 and 2. We show two limiting cases  $\Delta = 0$  (a)(b), and  $\Delta = 6$  (c)(d).

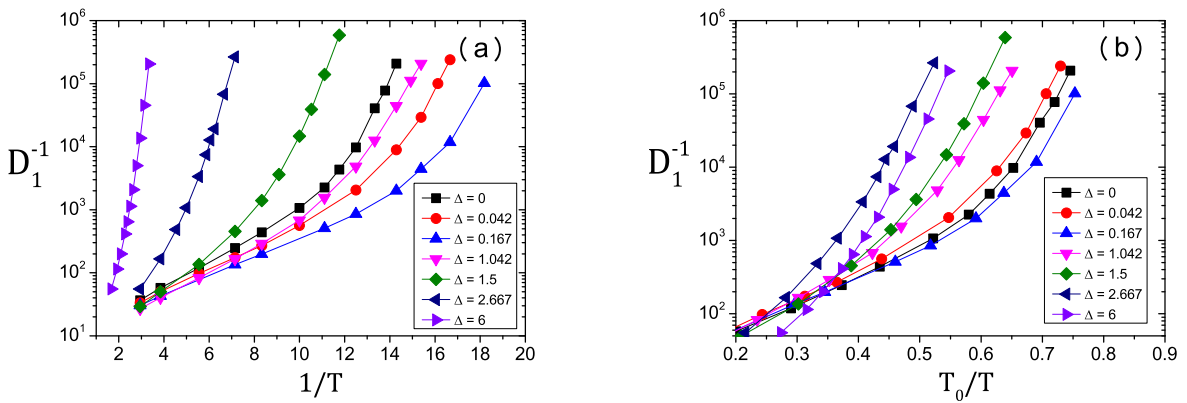


Figure 2.9: The Arrhenius plots of the diffusion constant for species 1. (a) Data are plotted as a function of the inverse temperature  $1/T$ . (b) The temperature is scaled by  $T_0$ , a fitting parameter of the VFT equation.

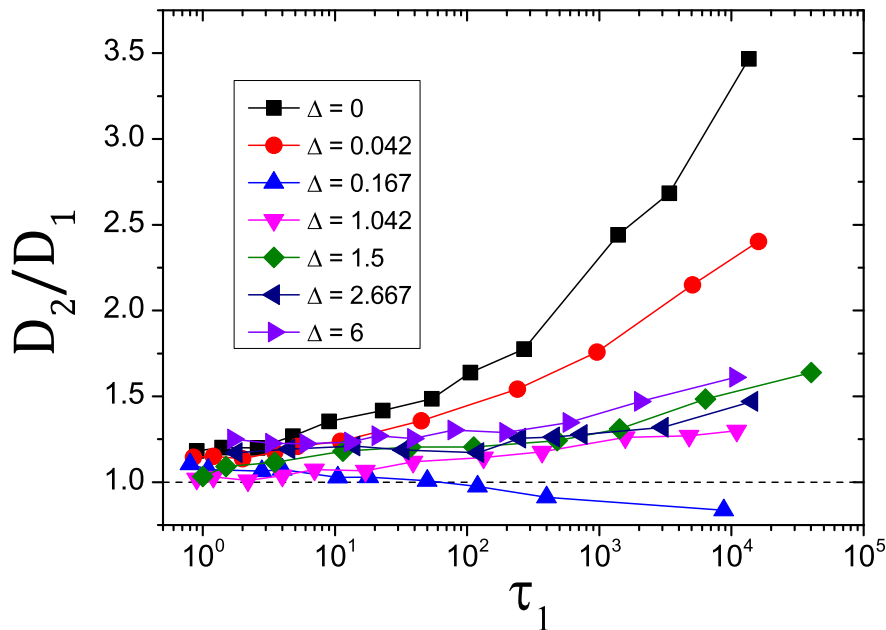


Figure 2.10: The ratio of  $D_2$  to  $D_1$  as a function of  $\tau_1$  for several  $\Delta$ 's.

NGP, a measure of non-Gaussianity of  $G_s(r, t)$ , is a useful indicator of the DH. The NGP  $\alpha(t)$  is defined by

$$\alpha(t) = \frac{3\langle |\mathbf{r}(t) - \mathbf{r}(0)|^4 \rangle}{5\langle |\mathbf{r}(t) - \mathbf{r}(0)|^2 \rangle^2} - 1. \quad (2.3.7)$$

We show  $\alpha(t)$  for two limiting cases,  $\Delta = 0$  and  $\Delta = 6$ , for the species 1 and 2 in Fig. 2.11. At high temperatures,  $\alpha(t)$  is very small, indicating the dynamics is almost Gaussian. However, as the temperature is lowered, pronounced peaks develop. Concomitantly, the time at which the peaks are located also increases. Note that this time is located at an intermediate time region slightly before the relaxation time,  $\tau_1$ .

The peak value of the NGP  $\alpha_{\text{peak}}$ , can be a measure of the DH. We show  $\alpha_{\text{peak}}$  as a function of  $\tau_1$  for several  $\Delta$ 's in Fig. 2.12. Typically,  $\alpha_{\text{peak}}$  increases with increasing  $\tau_1$ , or decreasing the temperature, which indicates a magnitude of the DH grows when the temperature is lowered for all  $\Delta$ 's. Here we find that when  $\Delta$  is lowered, the growth of  $\alpha_{\text{peak}}$  is pronounced. However, at  $\Delta = 0.167$ , where  $K$  has the maximum value, the growth of  $\alpha_{\text{peak}}$  is most pronounced for both species. This result shows the fragility and the magnitude of the DH are well correlated in the MCP model.

We also examine the SE violation which is another indicator of the DH [59]. It is well known that the self diffusion constant  $D$  and the viscosity  $\eta$  are related as  $D \propto 1/\eta$  in normal homogeneous liquids. This is so-called the SE relation [4]. However, it has been widely reported the SE relation is violated in the supercooled liquids near  $T_g$ . The SE violation is also believed to be a manifestation of the DH. Here, imagine that a supercooled liquid consist of highly heterogeneous patterns of mobile and immobile regions. The self diffusion of the target atom would be enhanced at the mobile region and suppressed at the immobile region. But overall, or averaged, diffusion would be affected by the mobile region more effectively than the suppression at the immobile region. On the other hand, the viscosity  $\eta$  is dominated mainly by highly stressed, or immobile, regions. Therefore, the SE relation is violated in the presence of the DH. The relation can be rephrased as  $D \propto 1/\tau_\alpha$  since  $\tau_\alpha$  is proportional to  $\eta$ , as we mention in Chap. 1.

Here we examine the SE violation of the MCP model using  $D_1$  and  $\tau_1$ . In Fig. 2.13, two different plots,  $D_1\tau_1$  vs.  $\tau_1$  (a) and  $D_1$  vs  $\tau_1$  (b) are shown. In Fig. 2.13(a),  $D_1\tau_1$  is normalized by  $D_1^*\tau_1^*$ , where

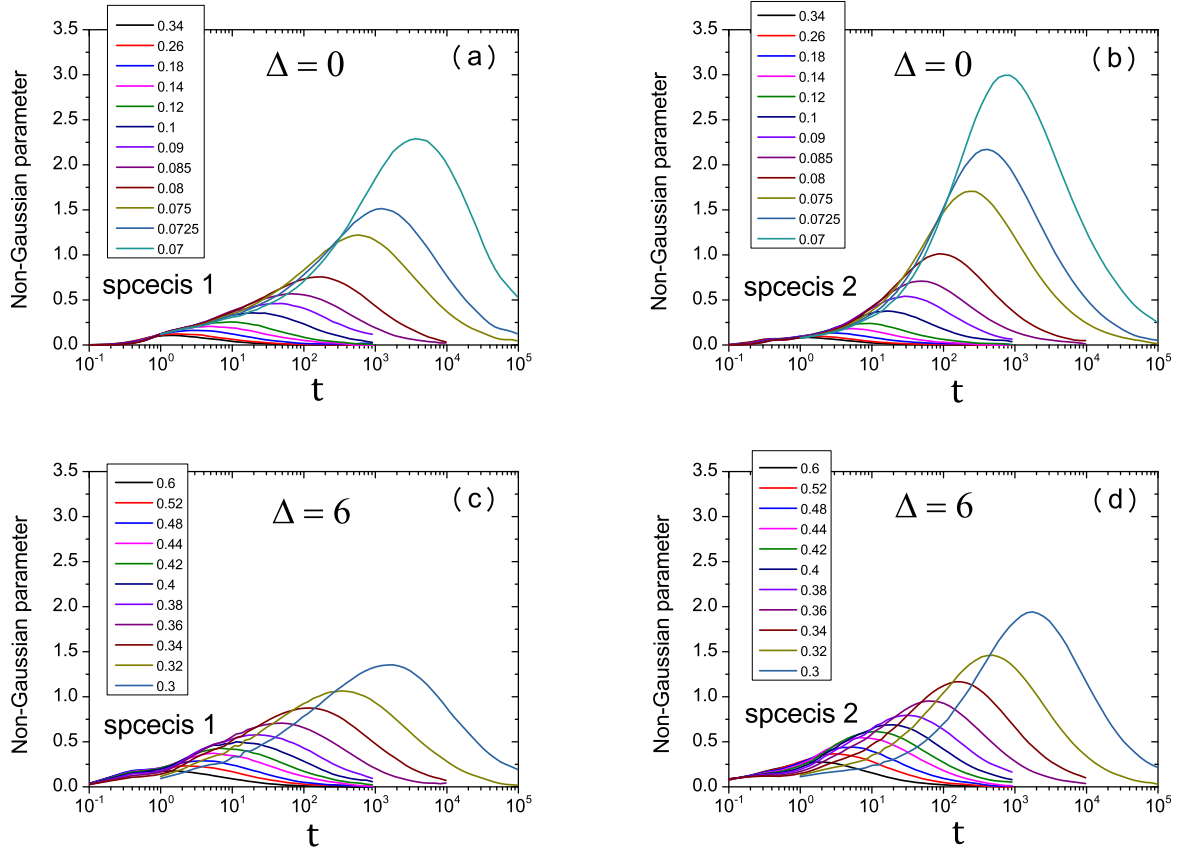


Figure 2.11: The non-Gaussian parameter of the particles belonging to species 1 and 2. Two limiting cases,  $\Delta = 0$  (a)(b) and  $\Delta = 6$  (c)(d), are shown.

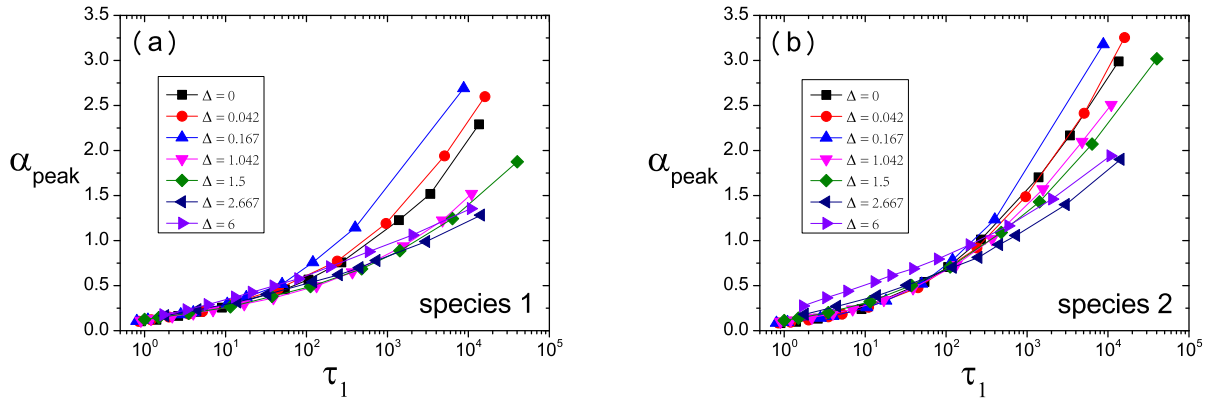


Figure 2.12: The peak value of the NGP  $\alpha_{\text{peak}}$  as a function of  $\tau_1$ .

$D_1^* = D_1(T^*)$  and  $\tau = \tau_1(T^*)$ ,  $D_1^* = D_1(T^*)$  and  $\tau = \tau_1(T^*)$  are diffusion and viscosity at the onset temperature  $T^*$ . Therefore,  $D_1\tau_1/D_1^*\tau_1^*$  takes nearly 1 if the SE relation holds. We find that whereas the SE relation holds at relatively high temperatures, it is apparently violated at low temperatures in all  $\Delta$ 's. Since  $D_1\tau_1/D_1^*\tau_1^*$  can be regarded as an indicator of the DH, we recognize that the DH is pronounced at low  $\Delta$ 's, especially  $\Delta = 0.167$  at which  $K$  is the maximum. This observation is consistent with the analyses of the NGP, which means the fragility and the DH is correlated in the MCP model. In Fig. 2.13(b),  $D_1$  is plotted as a function of  $\tau_1$ . The solid line is a line with slope -1 and represents the SE relation  $D_1^{-1} \propto \tau_1$ . The solid line in the figure indicates the SE relation,  $D_1^{-1} \propto \tau_1$ . While the data points converge to this solid line at high temperatures, they deviate from the line at low temperatures. The points at this high  $\tau_1$  and low  $D_1$  region look to ride on a single line. By fitting, we find that  $D_1^{-1} \propto \tau_1^{0.85}$ . The relation,  $D_1^{-1} \propto \tau_1^\zeta$ , is called the fractional SE relation. Our data suggest this relation holds with  $\zeta \simeq 0.85$  and similar value has been reported in experiments [60]. However, the physical meaning of the fractional SE relation is still unclear and thus further investigation is required [61] in the future.

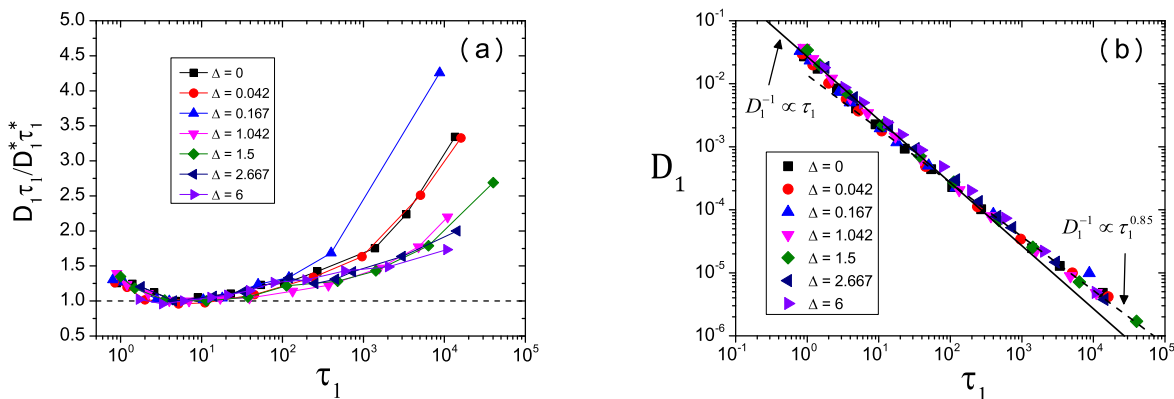


Figure 2.13: The Stokes-Einstein violation. (a)  $D_1\tau_1/D_1^*\tau_1^*$  as a function of  $\tau_1$ .  $D_1^* = D_1(T^*)$  and  $\tau_1^* = \tau_1(T^*)$ . (b)  $D_1$  vs.  $\tau_1$  plot. The solid and the dashed lines indicate  $D_1^{-1} \propto \tau_1$  and  $D_1^{-1} \propto \tau_1^{0.85}$  respectively.

## 2.4 Discussion and Future work

We summarize our results and discuss the future works.

In this Chapter, we have constructed a new model, the MCP model, whose fragility can be systematically controlled by tuning the single parameter  $\Delta$ , that is the depth of the pair interaction potential. The model enable us to bridge the gap between the tetrahedral network and the isotropic glass formers, showing the variation of the fragility from strong to fragile. The qualitative change of the structure is examined by using the radial distribution functions, the coordination numbers, and the static structure factors. We have found that the fragility is in harmony with these structural changes. This implies that the super-Arrhenius behavior can be attributed to static configuration of the system. Here we discuss the mechanism of the variation of the fragility in the MCP model. In the previous studies, it has been reported that the fragility of the network glass formers can be increased by increasing of the density (or pressure) [32, 62, 63]. Decreasing of  $\Delta$  might be related to the increasing of the density of the network systems [32, 62, 63] since at high densities, the attractive potential is less relevant. However, the variation of the fragility in the MCP model is much larger, because the density and other thermodynamic condition are fixed and a sole parameter  $\Delta$  has been changed.

Moreover, the correlation between the fragility and the DH has been also demonstrated. The MCP model have produced an empirical fact more fragile systems show larger heterogeneous dynamics.

As we explain in Chap. 1, the study of the fragility has long history. Several observables which correlate with the fragility have been reported in the past [10]. For example, mechanical constants, anomalous vibrational properties of the glass state [64], an exponent of the stretched exponential relaxation [13], and a temperature dependence of microscopic structure [65]. By using the MCP model, we shall verify these experimental facts and investigate microscopic origin of the correlations in future work.

## Chapter 3

# Ideal Glass Transition of Randomly Pinned Fluids

### 3.1 Motivation

In this Chapter, we investigate the issue of the ideal glass transition. The existence of the ideal glass transition temperature  $T_K$  has not been proved yet despite of intensive experimental and numerical studies. In this section, we review the nature of the ideal glass transition and the random first order transition theory (RFOT) which describes the ideal glass transition semi-quantitatively. Then, we explain the method to detect  $T_K$  in the computer simulation.

As we have explained in Chap. 1, the supercooled liquids show dramatic increase of the relaxation time and the viscosity before they eventually fall out of equilibrium at the empirical glass transition temperature  $T_g$  [1]. The thermodynamic description of the glass transition such as the Adam Gibbs theory (AGT) and its refined version, the RFOT, assume existence of a singular point, the ideal glass transition temperature  $T_K$  ( $< T_g$ ), at which the configurational entropy  $S_c$  (the logarithm of the number of the states which the system explores) vanishes and explain the slow dynamics in terms of this singularity [17, 66]. The AGT and RFOT are not the established theories of the glass transition. There are varieties of theories and scenarios explaining the glassy behaviors. These theories are often conflicting with each other and still remain highly controversial. One of such scenarios is the purely kinetic scenario of the glass transition which describes the slow dynamics without resorting on any thermodynamic singularity [67, 68]. The concept of the kinetic scenario has been built based on the studies of lattice models whose Hamiltonian has no interaction between the particles. Instead, an esoteric dynamical rule (called the constrained dynamics) is imposed to the model. Thus, the dynamical rule is the only ingredient to cause the slowing down. This model is called the kinetic constrained model (KCM). From intensive studies of several KCMs, the scenario claims that the slow dynamics of the glass formers can be explained as the facilitated dynamics of mobile regions of particles, called "defects" [67, 68]. The KCM does not show any thermodynamic singularity, *i.e.*,  $T_K$  does not exist. Indeed, most of the KCMs do not completely freeze at a finite temperature.

So far, both the thermodynamic scenarios such as the AGT and RFOT and purely kinetic scenario can explain the slow dynamics equally well [20, 68]. Any conclusive results which discriminate these conflicting scenarios are lacking. Thus, the ultimate goal of the study of the glass transition is to answer whether there exists  $T_K$  at which the dynamics completely freezes. However, identifying  $T_K$  is very difficult because the astronomical time scale is needed to reach  $T_K$  by experiments and simulations. Previous studies on  $T_K$  resorted on questionable fittings and extrapolations from the data at higher temperatures. Recently a novel idea, the random pinning, to bypass this difficulty has been proposed based on the RFOT [69–71]. Before going to explain the random pinning, we introduce the RFOT in the next section.

### The random first order transition theory

A promising candidate of the theory of the glass transition is the random first order transition theory (RFOT) inspired by the exact solution of the mean-field model of a spin glass [17, 66]. The RFOT inherits the basic concepts of the Adam Gibbs theory (AGT) (see Appendix A). In the mean-field limit, the RFOT offers microscopic basis for the concepts such as the ideal glass transition and the notion of the number of the states which are somewhat ambiguous in the phenomenological AGT. In the RFOT, the ideal glass transition is characterized by vanishing of  $S_c$  and growth of an order parameter, the overlap  $q$ .  $q$  quantifies similarity between two configurations in the phase space. A precise definition of  $q$  will be given later. The RFOT predicts that, at  $T_K$ ,  $q$  grows sharply from zero or small value (the fluid phase) to a large value (the ideal glass phase). Intuitively, in the glass phase, the system resides in very limited region in the phase space and takes similar configurations inside the region, and thus  $q$  is large. On the other hand, in the fluid phase,  $q$  is small since the system explores the phase space freely and takes many different configurations. When the glass transition from the fluid state to the ideal glass state takes place, a distribution function  $P(q)$  changes qualitatively.

The RFOT reconciles the (free) energy-landscape picture [72, 73] and the dynamic theory called the mode-coupling theory (MCT) [74]. We briefly explain the MCT in Appendix B. According to the RFOT scenario, the MCT temperature  $T_d$  which the MCT predicts as the temperature at which dynamics freezes is interpreted as the point at which exponentially large number of metastable states appear in the free energy landscape [66].  $T_d$  is also called the dynamic transition temperature since at this point, the thermodynamics is normal, *i.e.*, any thermodynamic singularity is absent. Hereafter, we call  $T_d$  the dynamic transition temperature instead of the MCT temperature. In general,  $T_d$  is located on relatively high temperatures compared to  $T_g$ . In practice,  $T_d$  can be measured as a point at which the unstable saddle modes vanish in the potential energy landscape [75, 76]

As we have explained above, the RFOT predicts that there are two important temperatures,  $T_K$  and  $T_d$ , to characterize the glass transition. Here, we briefly summarize what happens at these two transition points in the RFOT scenario. When  $T > T_d$ , the system can explore entire phase space freely. At  $T = T_d$ , the nature of the phase space qualitatively changes. The phase space splits into many small regions and the system can not move from one region into another region without activation processes. These fractured regions are regarded as metastable states. When  $T < T_d$ , the slow dynamics is dominated by the activation hopping processes between disconnected metastable states. Decreasing  $T$  further, the number of metastable states  $\mathcal{N}$  and thus the configurational entropy  $S_c = \log \mathcal{N}$  decrease. Eventually, at  $T = T_K$ , the ideal glass transition, or the Kauzmann transition, takes place at which  $S_c$  vanishes.

We emphasize that the above scenario is confirmed only in the mean-field limit. Thus, the crucial question is that whether the mean-field scenario holds even in finite dimensional systems. The RFOT predicts that in finite dimension, whereas the dynamic transition at  $T_d$  is smeared out and becomes a cross-over, the ideal glass transition still exists at  $T_K$ . However, as we have discussed several times in this thesis, the existence of the ideal glass transition in finite dimension has not been proved yet. This is largely because the dramatic increase of the relaxation times prevents the systems approaching  $T_K$ .

### Random pinning

Random pinning has been proposed to bypass this difficulty to identify  $T_K$  [69–71]. The random pinning is the way that freezing randomly a fraction of the degrees of freedom  $c$  of the system. For particulate system, a fraction of the particles of randomly chosen and their position is completely frozen. Originally, this method was introduced to model porous media environments [77]. For the randomly pinned system, the fraction,  $c$ , plays a role as a new control parameter of the glass transition, and hence the random pinning adds new axis in the thermodynamic phase diagram of temperature and pressure. In Ref. [69, 70], the effect of the random pinning in a mean-field spin glass model which is known to exhibit the ideal glass transition has been analyzed. It was shown that, by randomly pinning a fraction of the degrees of freedom from the equilibrium configuration, both  $T_K(c)$  and  $T_d(c)$  increase as  $c$  increases. Since the system generated by this protocol is already in equilibrated from

the beginning, one can access the ideal glass state by the computer simulation. Besides, the two lines of  $T_K(c)$  and  $T_d(c)$  eventually merge and terminate at a critical point in much the same way as the gas-liquid transition line terminates at the critical point. The universality of this critical point is predicted to belong to the random-field Ising model [78, 79].

### Outline of this Chapter

In this Chapter, we use the computer simulation to investigate thermodynamic properties of a model glass former in three dimensions in the presence of the pinned particles. The configurational entropy  $S_c$  and the overlap  $q$  are calculated to identify  $T_K$ . Moreover, the potential energy landscape (PEL) is analyzed to determine  $T_d$  as the point at which the saddle modes in the PEL vanish. The methods to compute  $S_c$ ,  $q$ , and geometrical properties of the PEL are explained in Sec. 3.2. The results of this Chapter are presented in Sec. 3.3. Finally, we summarize our results and discuss the future works in Sec. 3.4.

## 3.2 Methods

### Model

We use the binary mixture of the Lennard-Jones potential [6]. The model is often referred to as the Kob-Andersen (KA) model. Both species  $A$  and  $B$  have the same mass and the composition ratio is  $N_A : N_B = 80 : 20$ . The interaction potential between two particles is given by

$$v_{\alpha\beta}(r) = 4\epsilon_{\alpha\beta} \left\{ \left( \frac{r}{\sigma_{\alpha\beta}} \right)^{12} - \left( \frac{r}{\sigma_{\alpha\beta}} \right)^6 \right\}, \quad (3.2.1)$$

where  $\alpha, \beta \in \{A, B\}$ . We set  $\epsilon_{AA} = 1.0$ ,  $\epsilon_{AB} = 1.5$ ,  $\epsilon_{BB} = 0.5$ ,  $\sigma_{AA} = 1.0$ ,  $\sigma_{AB} = 0.8$  and  $\sigma_{BB} = 0.88$ .  $v_{\alpha\beta}(r)$  is truncated and shifted at  $r = 2.5\sigma_{\alpha\beta}$ . In the following, we will use  $\epsilon_{AA}$  and  $\sigma_{AA}$  as the units of energy and length. We set  $k_B = 1$ . Time units are defined by Monte Carlo steps (see below). Simulations are performed at constant density  $\rho \approx 1.2$ . The number of particles is  $N = 150$  and  $300$ , and most of the results in the present study are for  $N = 300$ .

### Making pinned configurations

Here we explain the method to generate the configuration of the pinned particles. First, we generate an equilibrium configuration of the bulk system, *i.e.*,  $c = 0$ . The next step is choosing  $cN$  particles that will be permanently pinned. One may choose the particles randomly from the equilibrium configuration. However, it has been reported that this way induces density inhomogeneity of the pinned particles, *i.e.*, there are dense or empty regions of the pinned particles in a simulation box. This inhomogeneity causes unwanted sample-to-sample fluctuations of the thermodynamic properties of the system. Therefore, we employ a "template" of the  $cN$  particles to avoid the inhomogeneity [80]. The template is the configuration whose  $cN$  particles are homogeneously distributed like normal liquids. To choose  $cN$  particles from a equilibrium configuration, once we map the equilibrium configuration to the template one and then pick up the closet particles with the  $cN$  particles in the template. Details on how to create the template is the following. To make a template configuration for  $cN$  particles, we use a monoatomic harmonic spheres. The interaction potential  $v_{\text{harm}}$  is given by,

$$v_{\text{harm}}(r) = \frac{\epsilon}{2} \left\{ 1 - \left( \frac{r}{\sigma} \right) \right\}^2, \quad (3.2.2)$$

where  $\epsilon$  and  $\sigma$  are energy and length scales for the template system. We equilibrate the  $cN$  particles by using standard molecular simulations in the periodic boundary condition. We set density  $\rho = 0.675$  and temperature  $T = 0.0015$ . This choice generates modestly high temperature liquid state and enables us to make relatively uniform template configurations. One can also use another potential system such as the LJ and the hard sphere instead of the harmonic one described the above to make the template configuration.

## Integrators

- Thermodynamics: In order to sample thermodynamic properties efficiently at low  $T$  and large  $c$  region, we use the replica exchange method [81, 82]. Here we describe the details of the replica exchange method. In this approach, one simulates simultaneously several copies of the system. All copies, or replicas, share the same Hamiltonian, but different temperatures  $T_i$  and energies  $E_i$  are assigned to each replica. The subscript  $i$  is the label for the  $i$ -th replica. In this study, we use up to 24 replicas and simulate the molecular dynamics (MD) for a single replica. We periodically attempt to exchange the configurations of two replicas at different temperatures in such a way that the Boltzmann distribution is achieved at long time and the detailed balance condition is guaranteed at each exchange step. The exchange probability  $p$  is given by

$$p = \min \left\{ 1, \frac{\exp \left[ -\frac{E_j}{k_B T_i} - \frac{E_i}{k_B T_j} \right]}{\exp \left[ -\frac{E_i}{k_B T_i} - \frac{E_j}{k_B T_j} \right]} \right\} = \min \left\{ 1, \exp \left[ (E_i - E_j) \left( \frac{1}{k_B T_i} - \frac{1}{k_B T_j} \right) \right] \right\}. \quad (3.2.3)$$

Due to stochastic nature of the exchange, a replica undergoes a random walk in the temperature space. Fast relaxation at high  $T$  induces to an efficient relaxation of the system at low  $T$ . The smallest difference in temperature between the two neighboring replicas is set to  $\Delta T = 0.018$ , which guarantees a good overlap of the two potential energy distributions. We try to switch the two neighboring replicas every 50000 time steps. A typical path of a replica in temperature space is shown in Fig. 3.1 (a). The figure shows that the replicas are exchanged frequently down to  $T = 0.44$  even when the concentration of pinned particles,  $c$ , is large. We also show the mean squared displacement (MSD) of the particles for the species  $A$  and  $B$  particles as a function of time in Fig. 3.1(b). The figure shows that at sufficiently long time the MSD becomes very large, indicating that the particles move through the simulation box also at high values of  $c$ . To calculate physical quantities, we monitor a given replica in the temperature space and use the replica only the time intervals at which this replica is at the target temperature.

- Dynamics: We employ the Monte Carlo (MC) dynamics simulation to calculate dynamical observables [28]. The rule of the MC dynamics is the following: In an elementary move, one of the  $(1 - c)N$  unpinned particle is chosen at random. Then the particle is displaced at random within a cubic box of linear size  $\delta = 0.15$  and the standard Metropolis rule is used to decide whether or not the move is accepted. One MC step consists of  $(1 - c)N$  such attempts and we set this step as a unit of time scale. The relaxation time  $\tau_\alpha$  is determined by  $F^A(k, \tau_\alpha) = e^{-1}$ , where  $F^A(k, t)$  is the density correlation function for the species  $A$  mobile (unpinned) particles. We have averaged over 30 different realizations of pinned particles to calculate  $F^A(k, t)$ .

## Entropy

In order to calculate the configurational entropy  $S_c = S - S_{\text{vib}}$  of the pinned system, we evaluate the (total) entropy of the system  $S$  and the vibrational entropy for the corresponding solid state  $S_{\text{vib}}$  independently [21, 83, 84].  $S$  is obtained by the thermodynamic integration of the energy from the target temperature  $T$  to the ideal gas limit,  $T \rightarrow \infty$ . For  $S_{\text{vib}}$ , the harmonic approximation is used. Although these methods are standard for the bulk system [21, 83, 84], the pinned system needs special cares. Technical details of the calculation of  $S_c$  for the pinned system is explained in Appendix C.

## Overlap

To evaluate the overlap of the system, we employ the following method [80]. We introduce  $q_{ab}$  measuring the degree of similarity between two arbitrary configurations  $a$  and  $b$  in the trajectory. In this thesis,  $q_{ab}$  is given by

$$q_{ab} = \frac{1}{N} \sum_{i,j} \theta(r_{\text{th}} - |\mathbf{r}_i^a - \mathbf{r}_j^b|), \quad (3.2.4)$$

where  $\theta(x)$  is the Heaviside function,  $\mathbf{r}_i^a$  is the position of particle  $i$  in configuration  $a$ , and the length scale  $r_{\text{th}}$  is 0.3. Hereafter, we drop off the subscripts  $ab$  from  $q_{ab}$  and simply express it as  $q$ .

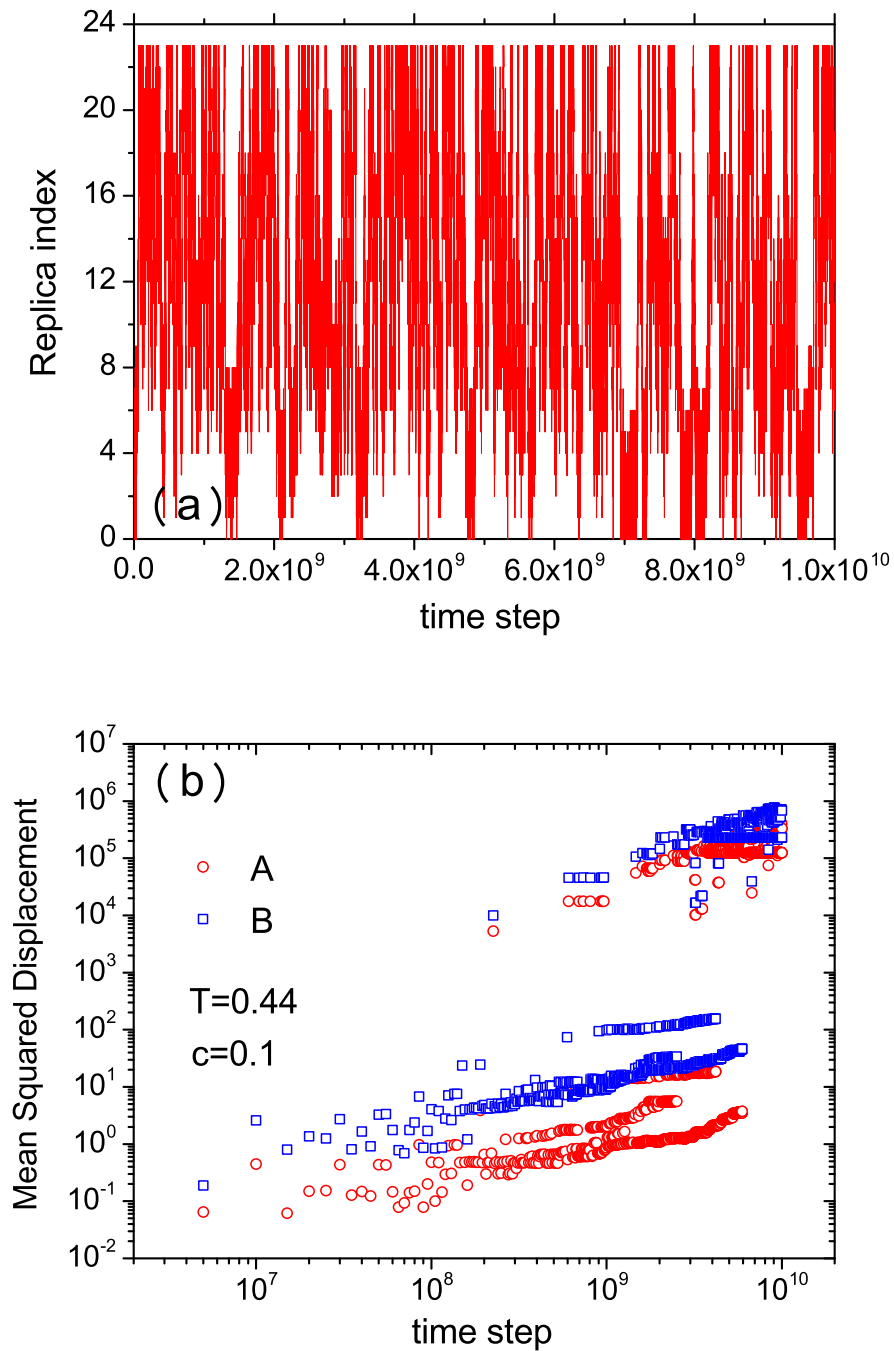


Figure 3.1: (a) Time dependence of the trajectory of a typical replica in temperature space for  $T = 0.44$ ,  $c = 0.1$ . The replica index labels the temperature of each replica from 0 (the lowest temperature) to 23 (the highest temperature). (b) The mean squared displacement of A and B particles for  $T = 0.44$ ,  $c = 0.1$ .

### Potential energy landscape analysis

To locate the system on the minima of the PEL, or the inherent structures (IS), in the pinned environment, we use the standard conjugate gradient method [85]. We minimize the potential energy  $U$  of the system including pinned particles, but only the positions of the unpinned particles are optimized during the minimization process and the positions of the pinned particles are fixed.

Another important quantity in the PEL analysis is the saddle modes. As we have explained,  $T_d$  is interpreted as the point at which the saddle modes in the PEL vanish. Thus, we determine  $T_d$  through the PEL analysis. To locate the system on the saddle of the PEL, we use a minimization of the squared gradient potential defined by  $W = \frac{1}{2}|\nabla U|^2$  [75, 76]. The minimization of  $W$  is performed by the BFGS method [85]. Similar to the minimization of  $U$  used to calculate the IS,  $W$  includes the position of the pinned particles as well as unpinned ones, but only the position of the latter are optimized. Once one locates a saddle with energy  $e_{\text{SP}}$ , the Hessian matrix of the potential energy at the saddle is diagonalized and we count the fraction of negative eigenvalues  $k(e_{\text{SP}})$ . The raw data is shown in Fig. E.1(a) in Appendix E. The threshold energy  $e_{\text{th}}$  is defined by  $k(e_{\text{th}}) = 0$ . Mapping of  $e_{\text{th}}$  to  $T_d$  is somewhat technical, we explain the details of this in Appendix E.

## 3.3 Results

### 3.3.1 Entropy and configurational entropy

We employ the thermodynamic integration (TI) method to calculate the entropy  $S$  of the pinned systems. First, we obtain  $S$  for a given configuration of pinned particles and then average over the realizations of the pinned particles.  $S$  as a function of  $c$  for several temperatures is shown in Fig. 3.2(a). Note that we show  $s = S/N(1-c)$  per (unpinned) particle. We find that when  $c$  increases,  $S$  decreases rapidly. For all temperatures which we simulated, the decrease is almost linear at small  $c$ . However, the lines "bent" at large but finite  $c$ , and then they follow the milder  $c$  dependence. This bending is especially sharp at low temperatures,  $T \lesssim 0.5$ . These results strongly indicate the existence of a thermodynamic anomaly taking place at finite  $c$ .

In order to characterize those high  $c$  phases, we calculate the entropy of the corresponding solid state. Since the entropy of the solid state is dominated by the vibrational entropy, we evaluate it by using the harmonic approximation [21, 83, 84],

$$S_{\text{vib}} = \sum_a \{1 - \log(\beta \hbar \omega_a)\}, \quad (3.3.1)$$

where  $\beta$ ,  $\hbar$ , and  $\omega_a$  are the inverse of the temperature, the Planck constant, and the square root of the eigen value of the Hessian matrix (see below), respectively. We obtain the configurations of the solid states (the inherent structures) by applying the minimization of the potential energy and calculate the vibrational entropy  $S_{\text{vib}}$  through the diagonalization of  $3N(1-c) \times 3N(1-c)$  Hessian matrix. We show  $S_{\text{vib}}$  in Fig. 3.2(a). One sees that  $S_{\text{vib}}$  also decreases as  $c$  increases. This decrease can be understood to be the consequence of the suppression of the low frequency modes in  $S_{\text{vib}}$  (see Appendix D). The decrease of  $S_{\text{vib}}$  is more modest than the total entropy  $S$  in the low  $c$  side. Increasing  $c$ , we find that  $S$  merges to  $S_{\text{vib}}$  around the point where  $S$  shows the bending.  $S_{\text{vib}}$  coincides with  $S$  at this bending point for  $T \lesssim 0.5$ . This means that the total entropy in high  $c$  phase is dominated by only vibrational contribution of the solid. For  $T \gtrsim 0.55$ , the bending of  $S$  are somewhat milder, which indicates that the transition becomes a crossover. According to the inherent structure (IS) formalism, the configurational entropy  $S_c$  is defined by the difference between the fluid and solid entropies [21]. In Fig. 3.2 (b),  $S_c = S - S_{\text{vib}}$  at several temperatures are plotted as a function of  $c$ . It is clearly demonstrated that  $S_c$  vanishes at a finite  $c$ . Note that  $S_c$  slightly overshoot the zero axis and become negative. This may be attributed to the overestimation of  $S_{\text{vib}}$  calculated based on the harmonic approximation. We discuss the anharmonic correction to  $S_{\text{vib}}$  in Appendix C. We roughly estimate the nonlinear contribution of the potential energy at the IS [73] and find that the corrections are small but negative so that the true  $S_{\text{vib}}$  should be slightly smaller than those obtained by the harmonic

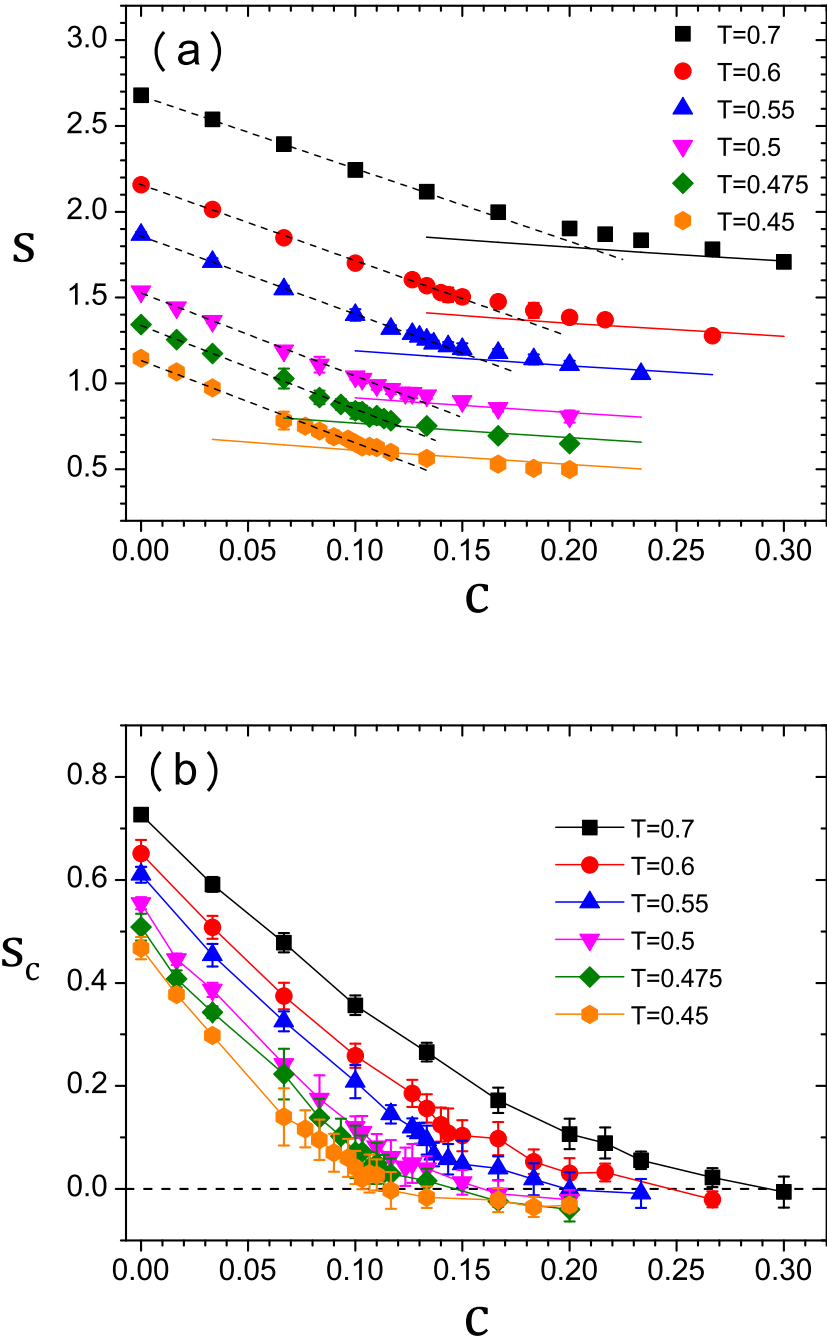


Figure 3.2: (a) The entropy of the systems evaluated using the thermodynamic integration as a function of  $c$ . The entropy of the solid states evaluated using the harmonic approximation are drawn in solid lines. The dashed lines are linear extrapolation from the low  $c$  sides. (b) The configurational entropy. Note that these plots are shown as the intensive values.

approximation. Evaluation of the exact values of the corrections, however, are difficult and beyond the scope of this thesis.

We define the ideal glass transition point  $c_K(T)$ , or  $T_K(c)$ , as the point at which  $S_c$  becomes zero. As the temperature is lowered,  $c_K(T)$  also decreases. In other words,  $T_K(c)$  increases as  $c$  increases. The phase diagram in the  $c$ - $T$  plane is shown in Fig. 3.6. It is important to realize that the bending of  $S_c$  (or  $S$ ) at  $c_K(T)$  becomes less clear at higher  $T$ . This will be discussed in details later. The results shown here are for the system size of  $N = 300$ . We also simulate the system of  $N = 150$  and confirm the finite size effect is small at least for these two sizes (see Appendix C).

As we have discussed in Chap. 1, similar bending of the (residual) entropy curve has been observed in bulk systems when the temperature is lowered below  $T_g$  [1]. But they are not the thermodynamic anomalies. It is simply that the system falls out of equilibrium due to the lack of the equilibration time. In these experiments, the (total) entropy at the low temperatures does not match with the solid entropy and hence the residual entropy is always finite. Therefore the bending we observe at the high  $c$  and ones reported in the experiments have completely different natures.

### 3.3.2 Overlap approach

The alternative method to identify the ideal glass transition point is to measure the overlap  $q$  [80]. According to the RFOT scenario, at the ideal glass transition point,  $q$  sharply increases from the value of the fluid phase to that of the ideal glass phase. We evaluate the overlap distribution  $P(q)$  for a given realization of the pinned particles, and  $\overline{P(q)}$  is the average of  $P(q)$  over the realizations of the pinned particles. Note that  $\langle(\dots)\rangle$  and  $\overline{(\dots)}$  are the thermal average and the average over the realizations, respectively. In Figs. 3.3(a) and (b),  $\overline{P(q)}$  at high and low temperatures,  $T = 0.7$  and  $0.45$ , are shown. For  $T = 0.7$ ,  $\overline{P(q)}$  has single-peak shape for all  $c$ , and its peak position shifts towards larger  $q$  as  $c$  increases. However, a qualitatively different behavior is observed at  $T = 0.45$ . Whereas,  $\overline{P(q)}$  has single-peak shape at low  $c$  side, suddenly, it splits into the two peaks at intermediate  $c$ . The low and high  $q$  peaks correspond to the fluid and glass phases, respectively and the transition from the fluid phase to the ideal glass phase is first order-like [80].

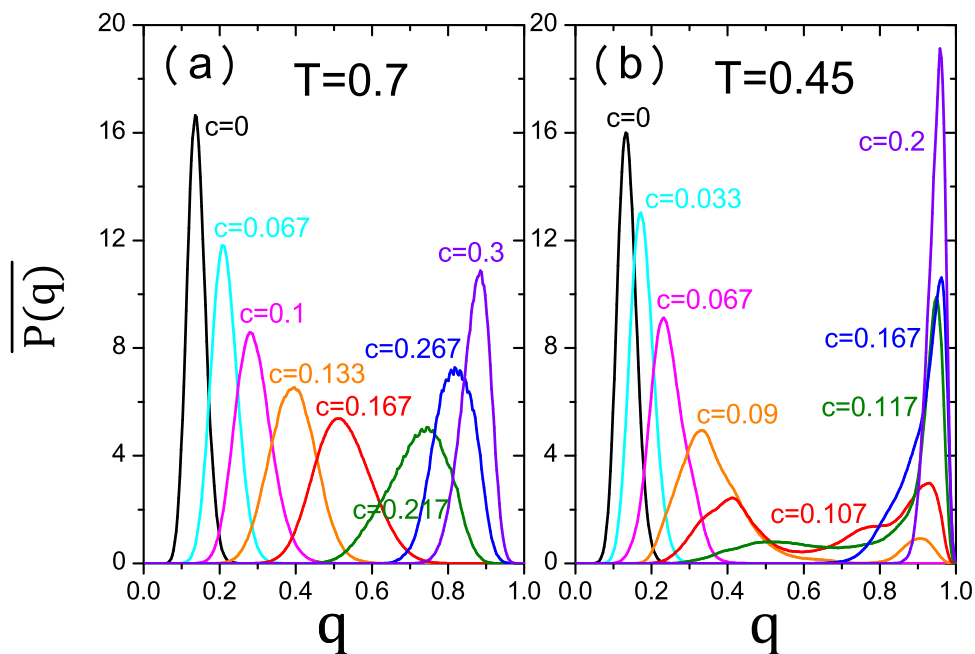


Figure 3.3: Distribution of the overlap  $\overline{P(q)}$  for  $T = 0.7$  (a) and  $T = 0.45$  (b).

In Fig. 3.4(a), we show the (double) average overlap  $\overline{\langle q \rangle}$  as a function of  $c$  for several  $T$ 's. For high

temperatures,  $T \gtrsim 0.6$ ,  $\overline{\langle q \rangle}$  smoothly increases with  $c$ , which reflects the continuous shift of the single peak of  $\overline{P(q)}$  shown in Fig. 3.3(a). For  $T \lesssim 0.5$ ,  $\overline{\langle q \rangle}$  steeply increases at intermediate  $c$ , in accordance with the double peak shape of  $\overline{P(q)}$  observed in Fig. 3.3(b). This sudden increase of  $\overline{\langle q \rangle}$  also suggests that a first-order-like transition takes place at intermediate  $c$ .

We extract the ideal glass transition temperature  $T_K^{(q)}(c)$  from the sudden, first-order-like, change of  $\overline{P(q)}$ . Note that we add the subscript  $(q)$  for distinguishing from  $T_K$  defined by  $S_c(T_K) = 0$ . In practice, we define  $T_K^{(q)}(c)$  by the temperature where the skewness of  $\overline{P(q)}$  vanishes, which means at  $T_K^{(q)}(c)$ ,  $\overline{P(q)}$  has equally weighted, or symmetric, double-peaks structure, *i.e.*, coexistence of the fluid and the ideal glass phases. The skewness  $\gamma(c, T)$  is the third moment of  $\overline{P(q)}$  and given by

$$\gamma = \frac{\int_0^1 dq \overline{P(q)} (q - \overline{\langle q \rangle})^3}{\left( \int_0^1 dq \overline{P(q)} (q - \overline{\langle q \rangle})^2 \right)^{3/2}} . \quad (3.3.2)$$

The  $T$  and  $c$  dependence of  $\gamma$  is shown in Fig. 3.4(b). The point at which  $\gamma$  is zero is used to define the ideal glass transition temperature  $T_K^{(q)}$ . In Fig. 3.6, we compare  $T_K$  and  $T_K^{(q)}$  in the  $c$ - $T$  plane. For small and intermediate  $c$ , we find a very good agreement between  $T_K(c)$  and  $T_K^{(q)}(c)$ , which means that the two different approaches detect the same ideal glass transition temperature. This is strong evidence that at this temperature the system undergoes a (equilibrium) thermodynamic phase transition from the fluid state to the ideal glass state. For temperatures,  $T \gtrsim 0.55$ , the two curves,  $T_K(c)$  and  $T_K^{(q)}(c)$ , depart from each other. We will discuss this behavior later. Finally, we mention that the curves,  $T_K(c)$  and  $T_K^{(q)}(c)$ , seem to extrapolate to  $T_K$  of the bulk system which has been estimated from extrapolation [21]. This shows that the present estimation of the bulk  $T_K$  is compatible with the one from previous estimates.

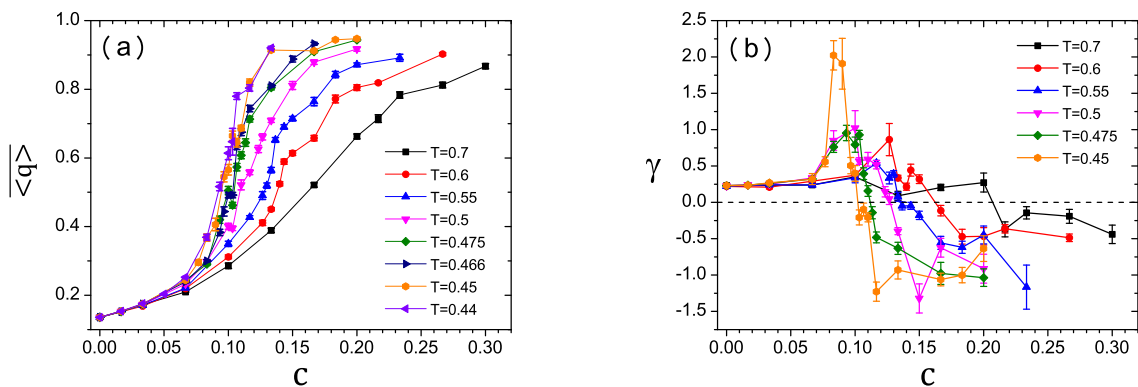


Figure 3.4: (a) The average overlap  $\overline{\langle q \rangle}$  obtained from  $\overline{P(q)}$  as a function of  $c$  for several temperatures. (b) The skewness  $\gamma$  of the distribution function  $\overline{P(q)}$ . The horizontal dashed line is the zero-axis and used to define  $T_K^{(q)}$ .

### 3.3.3 Potential energy landscape and its saddle points

One of the approaches to understand the slow dynamics and the glass transition is to investigate an influence of the ragged potential energy landscape (PEL) [72, 86]. Geometrical properties of the PEL and their relation with the glassy dynamics have been intensively examined in the previous studies [73, 87]. Analyzing the local minima, or the inherent structures (IS), and the saddle points are the basic methods to characterize the PEL. Here we investigate the influence of the pinning particles on the PEL. We analyze the ISs and the saddle points to determine the dynamic transition temperature  $T_d$  as an indicator of a geometrical property of the PEL.

It has been established that, for the bulk supercooled liquids, the onset of slow dynamics is correlated with the sudden decrease of the IS energy  $e_{\text{IS}}$  (the depth of local minima of the PEL) as the temperature is lowered [73,88]. In Fig. 3.5(a), the inherent structure energy averaged over the pinning configuration  $\overline{\langle e_{\text{IS}} \rangle}$  is plotted as a function of the temperature for several  $c$ 's. For the bulk system,  $c = 0$ ,  $\overline{\langle e_{\text{IS}} \rangle}$  is almost constant at high temperature but it suddenly decreases below a crossover temperature  $T \approx 1$  [88]. As  $c$  increases, the baseline of  $\overline{\langle e_{\text{IS}} \rangle}$  is raised up. This is because more optimized, or lower energy, configurations are prohibited due to the presence of the pinned particles<sup>1</sup>. Concomitantly, the crossover temperature from the low  $T$  slope to high  $T$  plateau increases with  $c$ , but the crossover is gradually smeared out.

In the inset of Fig. 3.5(a),  $\overline{\langle e_{\text{IS}} \rangle}$  at lower temperatures is shown. It demonstrates that  $\overline{\langle e_{\text{IS}} \rangle}$  is inversely proportional to  $T$  for all  $c$ 's. This is an indicator that the distribution of  $e_{\text{IS}}$  is Gaussian [89]. The relation between the shape of the distribution of  $e_{\text{IS}}$  and the existence of the ideal glass transition has been argued theoretically [89] and numerically [90]. According to Ref. [89], a model whose distribution is the Gaussian shows the ideal glass transition, but another model, a binomial distribution model, does not have the singularity at finite temperature. Moreover, it has been confirmed numerically a strong glass former model whose distribution is non-Gaussian does not show the ideal glass transition [90]. Therefore, the Gaussian distribution observed in the pinned system also supports the existence of the ideal glass transition from the PEL point of view.

Another important quantity to characterize the PEL is the saddle index  $K$ , *i.e.*, the number of negative eigenvalues of the Hessian matrix at a stationary point of the PEL. For the bulk systems, it has been empirically reported that  $K$  shows a linear dependence on the bare energy of a saddle point  $e_{\text{SP}}$  [75,76]. It is known that the threshold energy  $e_{\text{th}}$  at which  $K$  goes to zero corresponds to the average energy of the inherent structures  $\langle e_{\text{IS}} \rangle$  at the dynamical transition temperature  $T_d$ . Thus, one can extract  $T_d$  from two characteristic observables of the PEL,  $e_{\text{th}}$  and  $\langle e_{\text{IS}} \rangle$  [75,76]. In Fig. 3.5(b), we plot the average normalized saddle index  $k = K/3N(1 - c)$  as a function of its corresponding  $e_{\text{SP}}$ . We observe that  $k$  decreases linearly as a function of  $e_{\text{SP}}$  and hence we can determine  $e_{\text{th}}(c)$  via a linear fitting from high  $e_{\text{SP}}$  side. We find that  $e_{\text{th}}$  increases with  $c$ . By using  $\overline{\langle e_{\text{IS}} \rangle}$  curves in Fig. 3.5(a), we can extract  $T_d(c)$  as  $e_{\text{th}}(c) = \overline{\langle e_{\text{IS}} \rangle}(T_d(c))$ . More details of the method to map  $e_{\text{th}}(c)$  to  $T_d(c)$  is explained in Appendix E. We can conclude that  $T_d(c)$  indeed increases with  $c$  and the  $c$  dependence of  $T_d$  is shown in Fig. 3.6.

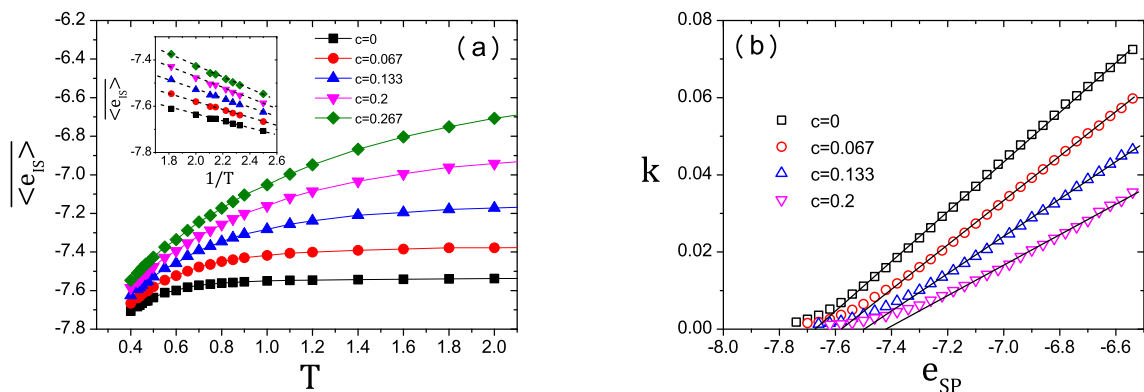


Figure 3.5: (a)  $T$  dependence of the averaged inherent structure  $\overline{\langle e_{\text{IS}} \rangle}$  for several  $c$ 's. The inset shows that  $\overline{\langle e_{\text{IS}} \rangle}$  at low  $T$  regimes are proportional to  $1/T$ , indicating that the distribution of  $e_{\text{IS}}$  is Gaussian for all  $c$ 's we simulated. (b) The averaged fraction of saddle modes,  $k$ , as a function of the saddle energy,  $e_{\text{SP}}$  for several  $c$ 's. The threshold energies,  $e_{\text{th}}$ , are defined by a linear extrapolation (the solid line) from the high energy side.

<sup>1</sup>Note that  $\overline{\langle e_{\text{IS}} \rangle}$  contains contribution of all interactions between particles including the interactions between pinned particles (see Appendix C).

## 3.3.4 Phase diagram

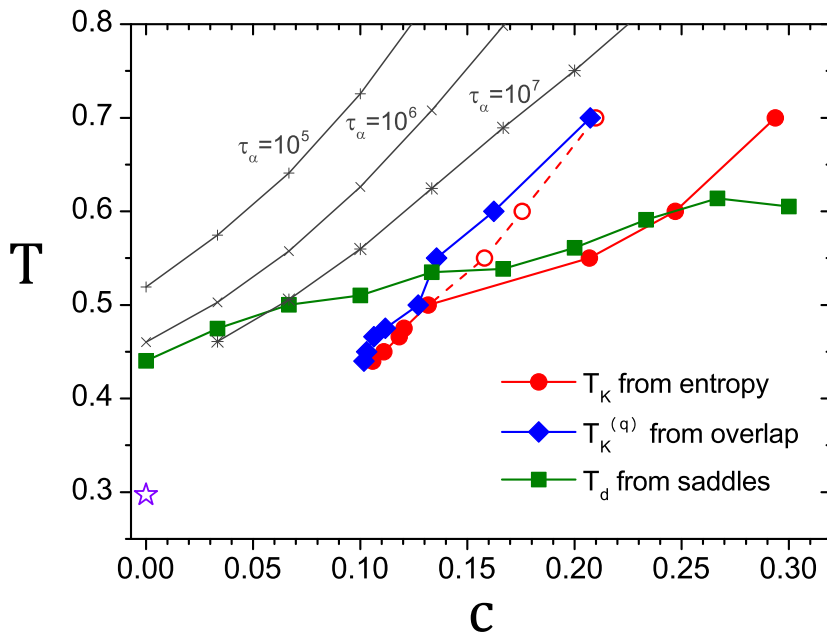


Figure 3.6: The phase diagram of the randomly pinned system. The filled circles show the ideal glass line  $T_K$  at which the configurational entropy vanishes. The diamonds show  $T_K^{(q)}(c)$  determined from the skewness of  $\overline{P(q)}$ . The squares are dynamic transition points  $T_d(c)$ . The open circles show the ideal glass line  $T'_K$  determined by the linear extrapolation of  $S_c(c)$  to vanish from Fig. 3.2(b). The iso-relaxation-times are drawn by +, ×, and \*. The star denoted at  $c = 0$  is a putative ideal glass transition point  $T_K \approx 0.3$  for the bulk reported in Ref. [21].

In Fig. 3.6, we summarize our results of the previous subsections in the  $c$ - $T$  plane. The ideal glass transition point  $T_K(c)$  determined from  $S_c = 0$  and  $T_K^{(q)}(c)$  obtained from  $\overline{P(q)}$  are plotted as the filled circles and diamonds, respectively. The two temperatures almost coincide at low  $T$  and low  $c$ . However, around  $(T, c) \sim (0.55, 0.16)$ , they depart from each other. Beyond this region,  $T_K(c)$  bends toward higher  $c$  region and its  $c$  dependence becomes milder. On the other hand,  $T_K^{(q)}(c)$  increases almost straightly. It has been predicted from a theoretical analysis of a mean-field spin glass model that  $T_K(c)$  terminates at a finite  $c$  (and  $T$ ) and this end point is a critical point [69–71]. Besides,  $T_K(c)$  line and spinodal line,  $T_d(c)$  line, merge and terminate at this critical point. We plot  $T_d(c)$  obtained from the saddle points analysis as filled squares in Fig. 3.6. Surprisingly  $T_d(c)$  passes through the region where  $T_K(c)$  and  $T_K^{(q)}(c)$  depart from each other. This means that three transition lines evaluated independently meet at the same end point as theoretically predicted [69–71]. Therefore, our results strongly support the existence of the critical point in the  $c$ - $T$  phase diagram. According to the RFOT, the nature, or universality class, of the critical point is predicted to be the random filed Ising model (RFIM) universality class [69, 70, 79]. Interestingly,  $T_K$  obtained from  $S_c = 0$  almost matches with  $T_d$  beyond the endpoint except very high  $c$ . This may be because, beyond the end point, the system resides at the bottom of the PEL where both the configurational entropy and the number of the saddle modes vanish simultaneously. Physics at very high  $c$  ( $\gtrsim 0.3$ ) region may be somewhat different from the prediction of the RFOT. Because at this region, the concentration of the pinned particles are so dense that dynamics of the system is dominated by hopping among (rare) holes surrounded by the pinned particles like the Lorentz gas model [91]. On the other hand, the continuous increase of  $T_K^{(q)}$  beyond the endpoint may be interpreted as a result that the coexistence line can extend beyond the

critical point, much the same way as the Widom line in the gas-liquid phase diagram [92, 93]. The Widom line is characterized as the line where the equation of state, or the derivative of the free energy, has the inflection point with respect to the order parameter [92, 93]. As Fig. 3.2(a) shows,  $T_K$  defined as the point where  $S_c = S - S_{\text{vib}} = 0$  is somewhat ambiguous beyond the endpoint ( $T \gtrsim 0.55$ ). In Fig. 3.6, we also plot  $T'_K$  (the empty circles) defined by the linear extrapolation of  $S_c$  in Fig. 3.2(b) from the low  $c$  side. Below the end point  $T \lesssim 0.5$ ,  $T'_K$  is indistinguishable from  $T_K$  but, beyond the end point  $T \gtrsim 0.55$ , they bifurcate and  $T'_K$  becomes comparable with  $T_K^{(q)}$ .

So far, we have drawn the phase boundaries in Fig. 3.6 from the purely thermodynamic variables. Finally, we compare them with a dynamic observable, the relaxation time  $\tau_\alpha$ .  $\tau_\alpha$  is extracted from the density correlation functions for various  $T$ 's and  $c$ 's. In Fig. 3.6, the iso- $\tau_\alpha$  lines are shown. This shows that the relaxation time also increases as  $c$  increases and the lines asymptotically approach to  $T_K$  lines from above.

### 3.4 Conclusion and discussion

In this study, we have succeeded to reach the ideal glass state, or zero-entropy state, at a finite temperature in finite dimension for the first time. The ideal glass transition temperature reported in the previous studies always relied on questionable extrapolation procedures and fittings from high temperatures [21, 83, 84, 94]. They left a wide room for debate about the existence of the ideal glass transition because other theories such as the purely kinetic scenario can explain the observed dynamic and thermodynamic behavior equally well without resorting on any thermodynamic singularity [95, 96]. We speculate that there are mainly two reasons why we could have reached the ideal glass states with a standard simulation method, the replica exchange method. (1) Equilibrium configurations are guaranteed from the outset of the simulation. (2) Sampling (phase) space is significantly reduced by the random pinning. So far, we have not known a question that which reason is dominant, qualitatively or quantitatively. However, if the reason (2) is crucial for the sampling of the ideal glass state, one can reach the ideal glass state in different pinning protocols such as choosing from the poisson distribution.

The "equilibrium" phase diagram in the  $c$ - $T$  plane which we drew in Fig 3.6 indicates that three independent observables, the configurational entropy, the overlap, and the saddle modes in the PEL, consistently point out the same end point. We could roughly estimate the position of the end point,  $(T, c) \sim (0.55, 0.16)$ , for the first time.

One of the next targets of the study is to understand the critical behavior in the vicinity of the endpoint and investigate its universality class. Theoretical analysis of the mean-field theory and the renormalization group analysis suggest that the endpoint is in the random field Ising model universality class [78, 79]. However, this has not been detected directly in real systems. Careful analysis of the finite-size scaling is necessary to verify this prediction. Another target is to detect the static length scale  $\xi$  predicted by the RFOT which governs the glassy dynamics [66]. Recently, an idea to probe such a static length from a vibrational property of the inherent structure has been proposed [97, 98]. One can apply this method for the pinned systems to detect  $\xi$  down to the ideal glass transition point, and then the  $c$ , or  $T$ , dependence of  $\xi$  can be used to determine the exponent of the RFIM universality class [70].

## Chapter 4

# Jamming Transition of Hard Spheres

### 4.1 Motivation

In this Chapter, we explore the relation between the glass and jamming transitions on the basis of the random first order transition theory.

It has been believed that the jamming transition takes place at a unique value of the volume fraction, the jamming transition point  $\varphi_J$ , since more than 50 years ago [99]. Intensive computer simulation studies reported that the frictionless spherical particulate systems such as the hard spheres always jam around  $\varphi_J \simeq 0.64$  [23, 100, 101]. In addition to its uniqueness, the point,  $\varphi_J$ , is involved with unusual properties such as the isostaticity. As we have discussed in Sec. 1.4, at a jammed packing with the isostaticity, the averaged contact number is  $Z_J = 2d$ , where  $d$  is the spacial dimension, which indicates that the number of degrees of freedoms matches with the number of constrains, *i.e.*, the system is marginally stable [101]. However, series of numerical and theoretical works have claimed that  $\varphi_J$  is protocol dependent and its uniqueness have been criticized [102–104]. Several numerical studies have also shown that the jamming transition of frictionless spheres takes place along a continuous range of volume fractions with their isostaticity intact [26, 105–109]. This fact implies that, the jamming transition "line" instead of point exists [26].

This fact should be explained by an unified theory of the glass and jamming transitions, if such a theory exists. As we have discussed in Chap. 3, a promising candidate of the theory of the glass transition is the random first order transition theory (RFOT). The RFOT is originally inspired by the mean-field theory of a spin glass model [17, 66]. The RFOT scenario unifies the glass and jamming transitions of frictionless particle systems, and thus the protocol dependence of  $\varphi_J$  can be understood to be a natural consequence of the scenario [110–112]. Here we briefly mention again the basic ideas of the RFOT. The RFOT integrates the classic idea of the (free) energy landscape pictures of the Adam Gibbs theory (AGT) [58, 72, 86], the concept of the ideal glass transition [19], the thermodynamic description of the disordered systems such as the replica theory [111], and the mode-coupling theory (MCT) [74].

In the mean-field limit, the RFOT predicts that when the temperature is lowered, the fluid first undergoes the dynamic transition at a temperature  $T_d$  followed by the thermodynamic transition at a lower temperature  $T_K$ , called the ideal glass transition temperature. Below  $T_d$ , the system starts exploring the rugged energy landscape and hence the dynamics of the system becomes sluggish. The energies at local minima of the landscape, the inherent structures (IS),  $e_{IS}$ , is obtained by quenching the system rapidly,  $T \rightarrow 0$ . When  $T > T_d$ , corresponding (averaged)  $e_{IS}$  is almost constant, but it suddenly starts decreasing below  $T_d$ , which reflects the qualitative change of the landscape. The MCT describes dynamics near  $T_d$  and predicts that the structural relaxation time  $\tau_\alpha$  diverges with a power law  $|T - T_d|^{-\gamma}$ , where  $\gamma$  is an exponent determined by the MCT equation [74]. In finite dimensions, however, the dynamic transition is smeared out by activation hoppings between local minima separated by finite barriers and becomes a mere crossover.

This argument can be translated to the hard sphere systems by replacing the temperature  $T$  and the (normalized) energy  $e = E/N$  with the inverse of the pressure  $P^{-1}$  and the (normalized) volume,

or the inverse of the density  $\rho^{-1} = V/N$ , respectively [113]. Instead of the inverse of the density, we shall adopt the inverse of the volume fraction  $\varphi^{-1}$ .

So the correspondence is  $T \leftrightarrow P^{-1}$ ,  $e \leftrightarrow \varphi^{-1}$ . Using this correspondence, the above statement about the inherent structure can be translated to the hard sphere systems as follows: The inherent structure  $\varphi_{\text{IS}}^{-1}$  is obtained by compressing a parent fluid equilibrated at a finite  $P$ , which means letting  $P \rightarrow \infty$ . This is nothing less than a process to generate the jammed packing for the frictionless hard sphere system and thus  $\varphi_{\text{IS}}$  should be identical to  $\varphi_{\text{J}}$ . Therefore, the RFOT scenario predicts that  $\varphi_{\text{IS}}^{-1}$ , or  $\varphi_{\text{J}}^{-1}$ , is constant if  $P$  of the parent fluid equilibrated at a volume fraction  $\varphi_{\text{eq}}$  is low, but starts decreasing as  $P$  or  $\varphi_{\text{eq}}$  exceeds  $P_d$  or  $\varphi_d$  in much the same way as that  $e_{\text{IS}}$  starts decreasing below  $T_d$ . In other words,  $\varphi_{\text{J}}$  is constant if  $\varphi_{\text{eq}} < \varphi_d$  but starts *increasing* when  $\varphi_{\text{eq}} > \varphi_d$ . This means that  $\varphi_{\text{J}}$  is not a unique value but a function of  $\varphi_{\text{eq}}$  and can be varied over a continuous range [110–112]. The largest jamming transition point, called the glass close packing point  $\varphi_{\text{G}}$ , would correspond to the inherent structures of the fluid at the thermodynamic transition point, *i.e.*,  $\varphi_{\text{eq}} = \varphi_{\text{K}}$  [111].

It has been believed that for finite dimensional systems, the dynamic transition point  $\varphi_d$  becomes a crossover region  $\varphi \in [\varphi_d^{(\text{theory})}, \varphi_d^{(\text{fit})}]$ , where  $\varphi_d^{(\text{theory})}$  is calculated from the MCT equation (see Appendix B) and  $\varphi_d^{(\text{fit})}$  is obtained by fitting simulation data for the relaxation times,  $\tau_\alpha \sim |\varphi_d^{(\text{fit})} - \varphi_{\text{eq}}|^{-\gamma}$ . Also, it has been speculated that the number of the saddle modes in the landscape vanishes at  $T_d^{(\text{fit})}$  and  $\varphi_d^{(\text{fit})}$  [75, 76, 114], whereas the inherent structures  $e_{\text{IS}}$  and  $\varphi_{\text{J}}^{-1}$  start decreasing at  $T_d^{(\text{theory})}$  and  $\varphi_d^{(\text{theory})}$ , respectively [88, 115]. Therefore, according to the RFOT scenario,  $\varphi_{\text{J}}$  should increase if we prepare a dense parent fluid such that  $\varphi_{\text{eq}} > \varphi_d^{(\text{theory})}$ .

The main purposes of this Chapter are to verify the above prediction of the RFOT by using the computer simulation of the jamming transition and analyzing the MCT equation in finite dimensional systems [116] and to investigate the mechanism of denser jammed packings by analyzing structural, or geometrical, and vibrational properties.

Here, we briefly mention the outline of this Chapter. We explain the simulation methods of the jamming transition in Sec. 4.2. The method of numerical analysis of the MCT equation is explained in Appendix B. In Sec. 4.3, we show the dependence of  $\varphi_{\text{J}}$  on the initial configurations of the parent fluid at  $\varphi_{\text{eq}}$ . We also examine the structural and vibrational properties of the jammed states. Moreover, we present the correlation with the denser jammed packings and other variables such as the bond-orientational order and the locally preferred structures. Finally, we summarize and discuss the results in Sec. 4.4.

## 4.2 Methods

### Model

Throughout this Chapter, we employ a binary mixture of the hard spheres in 3D (3 dimensions) and 2D (2 dimensions) with the size ratio  $R = \sigma_{\text{L}}/\sigma_{\text{S}}$  and the mole fraction of the smaller sphere  $x_{\text{S}} = 0.5$ .  $\sigma_\alpha$  is the diameter of the sphere for species  $\alpha$ , where  $\{\alpha, \beta\} \in \{\text{L}, \text{S}\}$ . We adopt  $R = 1.0, 1.4, 1.7$ , and  $2.0$  ( $R = 1.0$  is monodisperse system) but we mainly use  $R = 1.4$ .

### Monte-Carlo method

We use the standard Monte-Carlo (MC) method with the periodic boundary condition to prepare equilibrium states of the hard spheres. The dynamic rule to move the particles in the MC simulation is explained in the following. First,  $N$  hard spheres (disks) are distributed randomly over cubic (square) box with the volume fraction  $\varphi_{\text{eq}}$ . In every steps, a particle is chosen at random from  $N$  particles. Then, the particle is displaced at random within a small cubic (square) box of linear size  $0.1\sigma_{\text{S}}$  centered around the original position. The move is accepted if the hard sphere (disk) constraint is satisfied. One MC step consists of  $N$  such attempts. We use a MC step as a time unit. This mixture is known to be a model of the colloidal glass formers [117]. In order to equilibrate the state, we repeat the MC steps more than  $30\tau_\alpha$ , where  $\tau_\alpha$  is the structural relaxation time defined by  $F_s(k, \tau_\alpha) = e^{-1}$ .

$F_s(k, t)$  is the self part of the density correlation function for the large particles given by

$$F_s(k, t) = \frac{1}{N} \left\langle \sum_{j=1}^N \exp[i\mathbf{k} \cdot (\mathbf{r}_j(t) - \mathbf{r}_j(0))] \right\rangle, \quad (4.2.1)$$

where  $\mathbf{k}$  is the wave vector, and we set  $k = |\mathbf{k}|$  as the inverse of the large particle diameter,  $k = 2\pi/\sigma_L$ .

### Generating jammed states

Here we explain the method to generate the hard sphere jammed packings [23, 100, 118]. There are several procedures to generate the jammed packing in the computer simulation. Among them, we use a standard algorithm developed by Ref. [100]. In short, this method replaces the hard sphere potential with the harmonic sphere one (see below) for technical convenience and compresses the system rapidly. Allowing the spheres to be deformed slightly enables us to reach jammed configurations with low computational costs. In actual experiments, the hard spheres are thrown in box randomly or the box is compressed with the size of the spheres unchanged. On the contrary, we inflate the spheres with the box size fixed to increase the volume fraction of the system homogeneously. This is the frame work of the packing algorithm. The details of the algorithm is explained below.

First, we prepare an equilibrium configuration by the MC simulation of hard spheres (disks). Next, we switch the hard sphere potential to the harmonic sphere one given by

$$v(r_{ij}) = \frac{\epsilon}{2} \left\{ 1 - \left( \frac{r_{ij}}{\sigma_{ij}} \right) \right\}^2 \theta(1 - r_{ij}/\sigma_{ij}), \quad (4.2.2)$$

where  $\epsilon$  is the energy scale,  $r_{ij}$  is the distance between  $i$ -th and  $j$ -th spheres,  $\sigma_{ij} = (\sigma_i + \sigma_j)/2$  is the distance of the two spheres at contact, and  $\theta(x)$  is the Heaviside function. In the following, we will use  $\epsilon$  and  $\sigma_S$  as the units of energy and length. Then, we inflate the spheres instead of shrinking the simulation box. We increase the volume fraction of the system  $\varphi$  with  $\delta\varphi = 0.0025$ . This compression process makes overlaps among spheres and results in the finite value of the total potential energy  $U = \sum_{i<j} v(r_{ij})$ . These overlaps are eliminated by applying the conjugate gradient (CG) method to minimize  $U$  [85]. The CG method is stopped when the following condition holds,  $\|\nabla U\|/(2N) < \epsilon_{\text{tol}}$ . We set  $\epsilon_{\text{tol}} \in [10^{-7}, 10^{-9}]$ . For larger systems, the smaller value of  $\epsilon_{\text{tol}}$  is used. If  $U$  still has finite value after minimization, we decrease  $\delta\varphi$  and repeat compression and decompression until  $U$  becomes zero. This process is interpreted as pulling the system from trivial local potential energy minima. We stop the algorithm when  $\delta\varphi < 10^{-6}$ , and the resultant system is the hard sphere jammed packing. More detailed flowchart of this algorithm is seen at Fig. 1 of Ref. [118]. We use the system sizes  $N=64, 128, 256, 512, 1024$ , and  $2048$  in 3D and 2D. We mainly use  $N = 1024$  to compute structural properties of the jammed states.

## 4.3 Results

### 4.3.1 Onset of denser jamming transition points and the dynamic transition

Here we show the  $\varphi_{\text{eq}}$  dependence of the jamming transition point  $\varphi_J$ , and we compare the onset density at which  $\varphi_J$  start increasing and the dynamic transition point  $\varphi_d^{(\text{theory})}$  obtained by the numerical analysis of the MCT equation. First, we prepare the equilibrium configuration of the hard spheres at  $\varphi_{\text{eq}}$ . Then, we quench this configuration by using the packing algorithm described in Sec. 4.2.

In Figs. 4.1(a) and (b), we present the system size  $N$  dependence of  $\varphi_J(N)$  as a function of  $\varphi_{\text{eq}}$  for the binary mixture with  $R = 1.4$  in 3D and 2D. Using these finite size data, we estimate the large  $N$  limit value of  $\varphi_J$ . In Figs. 4.1(c) and (d),  $\varphi_J$  in the large  $N$  limit is evaluated by using the standard finite-size scaling,  $|\varphi_J - \varphi_J(N)| \sim N^{-1/\nu d}$ , where  $\nu$  is a scaling exponent and  $d$  is the spatial dimension. The results of O'Hern *et al.* [100] and Chaudhuri *et al.* [26] are also shown as the horizontal dotted lines and the square points, respectively. We confirm that our results are consistent with those of the

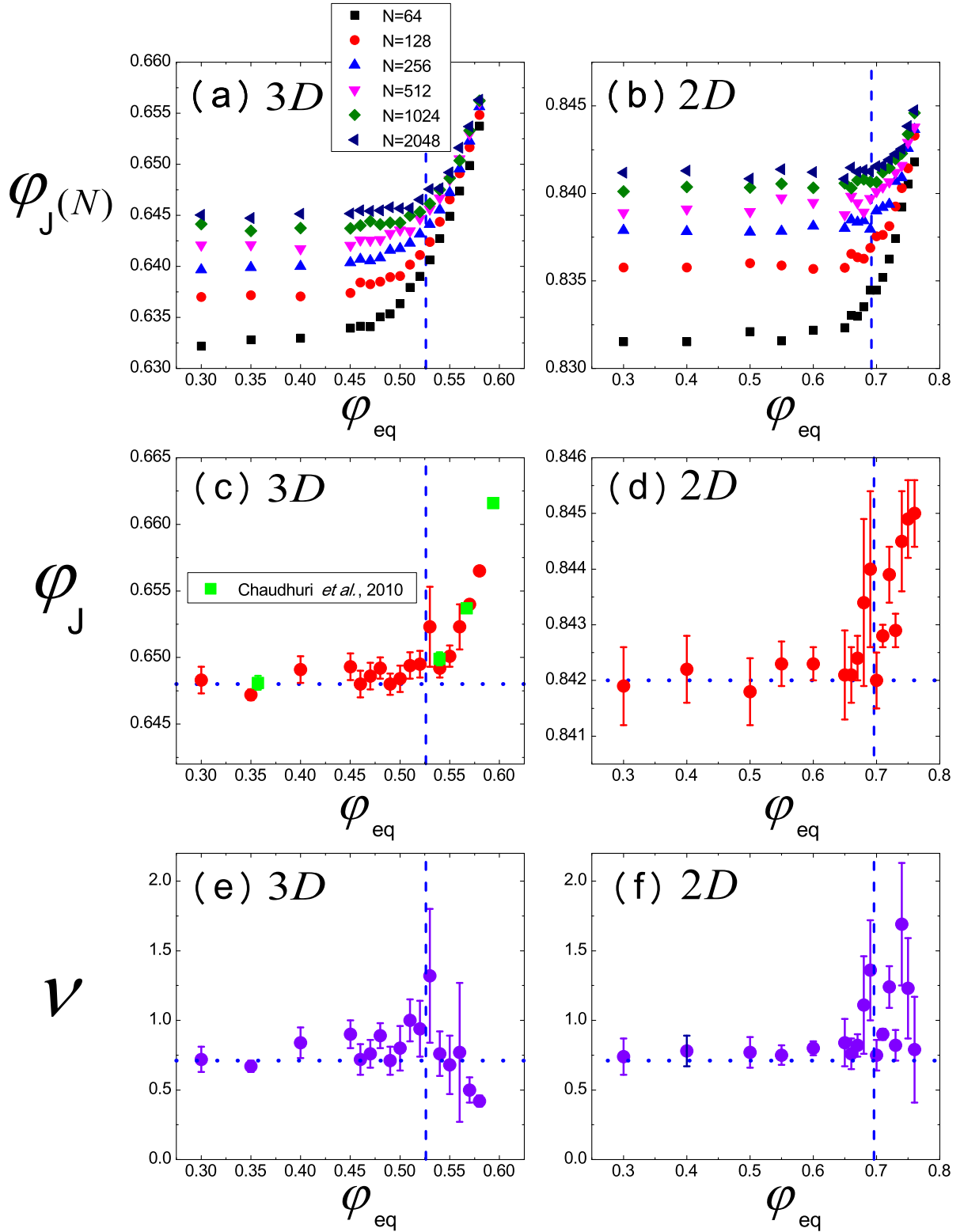


Figure 4.1: (a), (b) Finite size value  $\varphi_J(N)$  as a function of  $\varphi_{eq}$  for the binary mixture with  $R = 1.4$  in (a) 3D and (b) 2D. (c), (d) Estimation of  $\varphi_J$  by using the finite size scaling from the data of (a) and (b). The square points in (c) are  $\varphi_J$  reported by Chaudhuri *et al.* [26]. (e), (f) The finite size scaling exponents  $\nu$ . The vertical dashed lines in (a) - (f) are the positions of  $\varphi_d^{(theory)}$ . The horizontal dotted lines in (c) - (f) are  $\varphi_J$  and  $\nu$  reported by Ref. [100].

previous studies. The finite size scaling exponents  $\nu$  are shown as a function of  $\varphi_{\text{eq}}$  in Figs. 4.1(e) and (f). We notice that fitting precision become worse at high  $\varphi_{\text{eq}}$  region in both 3D and 2D, and this uncertainty leads to the larger error bars of  $\varphi_J$  as seen in Figs. 4.1(c) and (d). Therefore, we fix the exponents to  $\nu = 0.72$  (3D) and  $0.74$  (2D). We replot the data using this  $\nu$ -values in Figs. 4.2(a) and (b). The  $\varphi_J$  curves become smooth by fixing  $\nu$ 's to these values both in 3D and 2D. At lower  $\varphi_{\text{eq}}$ , corresponding  $\varphi_J$ 's are identical with those already reported in the literatures [23, 100]. However,  $\varphi_J$  abruptly starts increasing at higher  $\varphi_{\text{eq}}$ . Notable dependence of  $\varphi_J$  on  $\varphi_{\text{eq}}$  is consistent with the result of Chaudhuri *et al.* [26]. Remarkably, the onset point where  $\varphi_J$  starts increasing is found to be very close to  $\varphi_d^{(\text{theory})}$  independently evaluated by the MCT equations. Thus, we confirm the prediction of the RFOT quantitatively in 3D and 2D.

We find that this trend is also observed at different systems by changing the size ratio  $R$ . In Fig. 4.3, we show  $\varphi_J(N)$  as a function of  $\varphi_{\text{eq}}$  and  $R$  for  $N = 1024$  in 3D. We observe that the increase of  $\varphi_J$  becomes mild with increasing  $R$ . This is consistent with the case for the IS of the continuous potential model [119]. However, the onset points found in the simulation data and  $\varphi_d^{(\text{theory})}$ 's barely change with increasing  $R$ .

Here we discuss two issues. One thing is the failure of the finite size scaling. The failure of the naive finite size scaling at higher  $\varphi_{\text{eq}}$  is suggestive. We argue that  $\varphi_d^{(\text{theory})}$  may also mark the point beyond which the finite size scaling law is qualitatively altered due to the emergence of another competing length scale. According to the RFOT scenario, at the crossover region where the MCT's critical dynamics and activation hoppings coexist, the finite size effect is highly nontrivial [47]. Thus, we presume that the failure of the finite size scaling at  $\varphi > \varphi_{\text{eq}}$  is another, though indirect, evidence supporting the RFOT scenario. To improve the finite size scaling argument further, we need larger system size data and thorough inspection of the finite size scaling law and its correction [120].

Another issue is an inconsistent result reported in another model system. Correspondence of the onset of the IS to theoretical dynamic transition point has been reported for various short-ranged potential models [115]. However, the opposite trend has observed at a fully-connected, mean-field, models [121]. Mari *et al.* [121] reported that the onset volume fraction at which  $\varphi_J$  starts increasing is considerably lower than  $\varphi_d^{(\text{theory})}$  obtained from the simulated relaxation time. This contradictory result might be due to the long-ranged interaction of the model. Indeed, it has been known that the onset temperature of the IS for a fully-connected spin-glass model for *finite size* is much higher than the mean-field value and convergence to the mean-field limit is extremely slow [122]. We speculate that this trend should be understood to be stabilization of the saddle points in the landscape. In general, we can assume that the saddle points are unstable at  $\varphi_{\text{eq}} < \varphi_d^{(\text{theory})}$  region. However, for the *finite-size* fully-connected model, the number of degrees of freedom is lacking for constructing modes escaping from the saddle points [122]. Then, the saddle points are stabilized at relatively lower  $\varphi_{\text{eq}}$  than  $\varphi_d^{(\text{theory})}$ .

### 4.3.2 Geometrical and vibrational properties

Here, we show geometrical and vibrational properties of the denser jammed packings generated by the above.

As we have discussed in Sec. 1.4, the averaged contact number  $Z_J$  at  $\varphi_J$  is closely related to the stability of the system, and it plays a central role in characterizing the jamming configurations [101]. When a system is isostatic, the condition  $Z_J = 2d$  holds, which means that the system is in a marginal stable state. In practice, two particles  $i$  and  $j$  are considered to be in contact if  $r_{ij} \leq (1+a)\sigma_{ij}$ , where  $a = 10^{-8}$  in this thesis.  $Z_J$  is given by  $Z_J = N_c/(N - N_r)$ , where  $N_r$  is the number of the rattler particles,  $N_c$  is the number of contact pairs among  $(N - N_r)$  particles which make a contact network. We define the rattler particle as the particle whose contact number is smaller than  $d + 1$ .

We show the scatter plot of  $Z_J$  vs.  $\varphi_J$  in Figs. 4.4(a) and (b) for various initial volume fractions  $\varphi_{\text{eq}}$ . Even though  $\varphi_J$  exists over the continuous range of the volume fraction,  $Z_J$  remains always close to 6 in 3D and 4 in 2D. We also examine the probability distribution function of the contact number *per particle* in Figs. 4.4(c) and (d). We find that the shape of distribution functions barely change even at

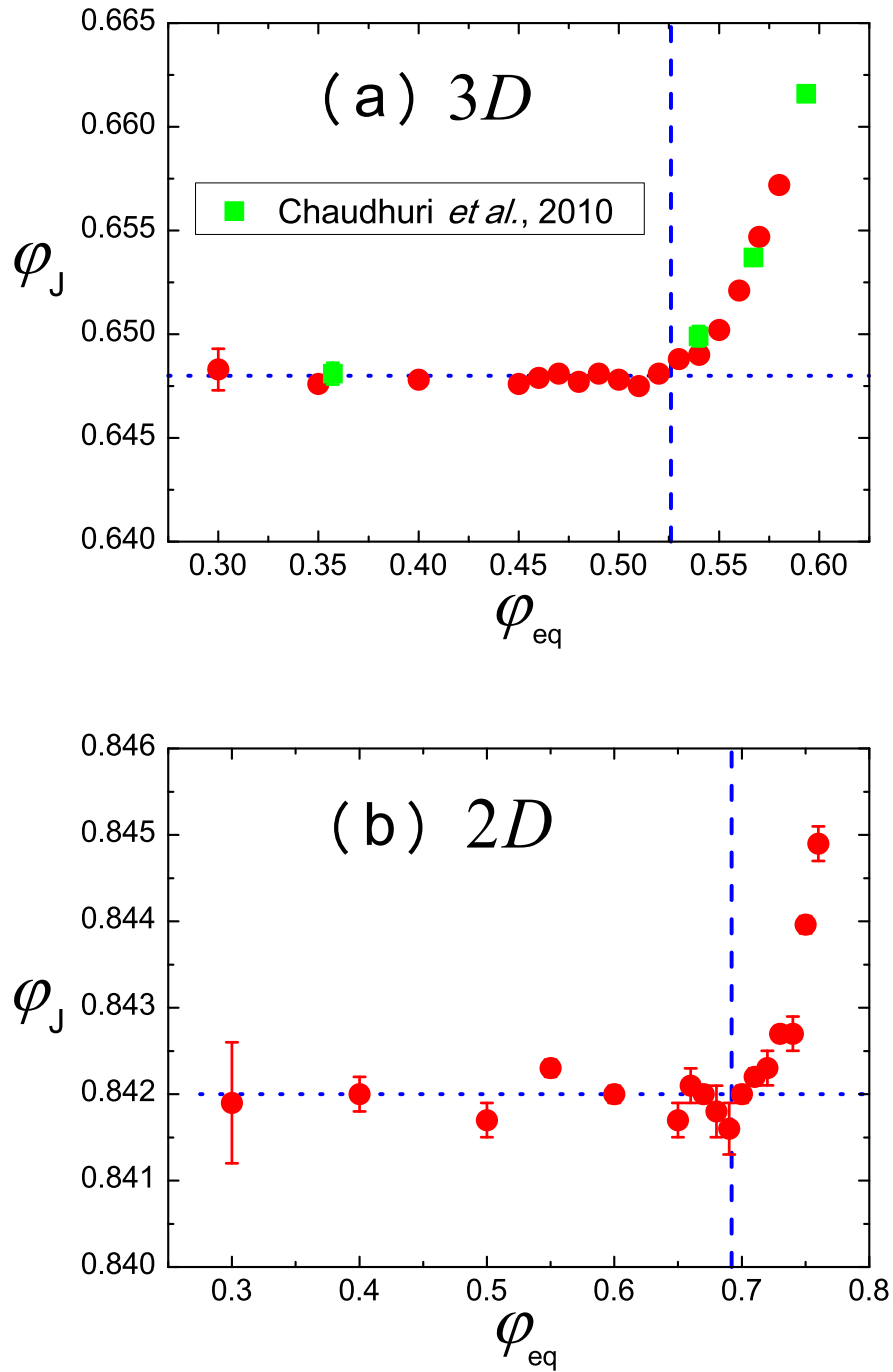


Figure 4.2: (a), (b)  $\varphi_J$  as a function of  $\varphi_{eq}$  for the binary mixture with  $R = 1.4$  in 3 (a) and 2 (b) dimensions. Each  $\varphi_J$  is obtained by the finite size scaling with fixing  $\nu$  at the lowest  $\varphi_{eq}$ . The square points in (a) are  $\varphi_J$  reported by Chaudhuri *et al.* [26]. The horizontal dotted lines are  $\varphi_J$  reported by O'Hern *et al.* [100]. The vertical dashed lines are the positions of  $\varphi_d^{(theory)}$ .

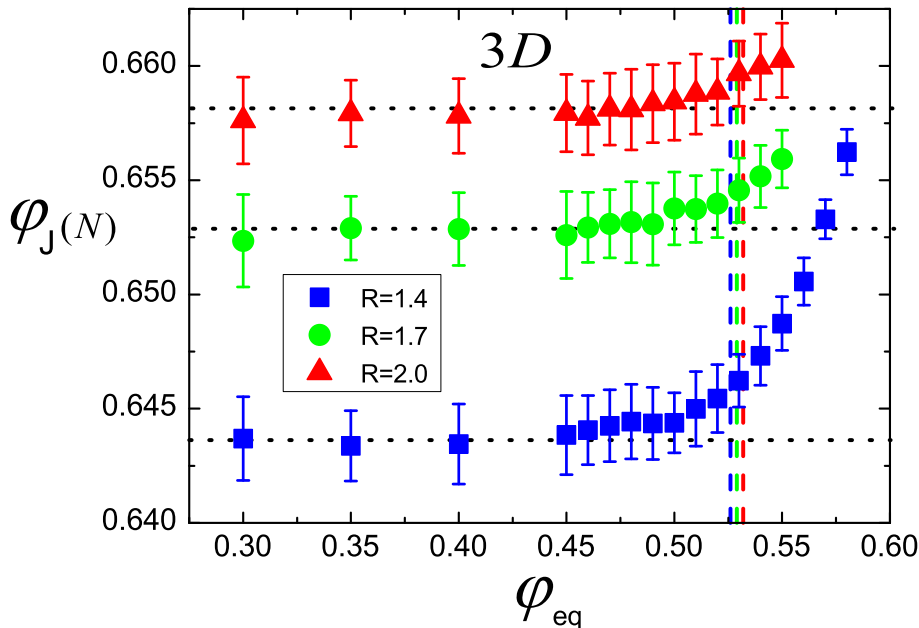


Figure 4.3:  $\varphi_J$  as a function of  $\varphi_{\text{eq}}$  and  $R$  for  $N = 1024$  in 3D. The horizontal dotted lines are guides to the eye. The vertical dashed lines are the positions of  $\varphi_d^{(\text{theory})}$ .  $\varphi_d^{(\text{theory})} = 0.526, 0.529$ , and  $0.532$  for  $R = 1.4, 1.7$ , and  $2.0$ , respectively.

the denser jammed packings in both 3D and 2D. If partial crystallization occurs in the denser jammed packings, we expect to observe some peaks at  $Z \sim 12$  (the face centered cubic) in 3D and  $Z \sim 6$  (the hexagonal packing) in 2D. However, such peaks are not observed. From these facts, we conclude that the denser jammed packings generated by our protocol remain the isostatic at least within our numerical precision. This is consistent with recent numerical works [26,107]. Note that the question of whether a jammed packing is truly isostatic in a finite system size under periodic boundary conditions is quite subtle because, the isostatic condition is only true in the large  $N$  limit [123]. Testing the isostaticity of the continuous range of  $\varphi_J$  in the large  $N$  limit and the binary case in high resolution is left for the future works [124].

It has been reported from numerical studies that in the binary mixture for  $R = 1.4$  [23], nearly 5% of the particles are the rattlers which do not participate in the contact network. One might conceive that as  $\varphi_J$  increases, the fraction of the rattlers decreases to reduce vacant spaces. In Figs. 4.5(a) and (b), we show the rattler fraction as a function of  $\varphi_{\text{eq}}$ . We confirm that the rattler fractions at  $\varphi_{\text{eq}} < \varphi_d^{(\text{theory})}$  are nearly 5% in both dimensions. This is consistent with previous study [23]. However, the rattler fractions *increases* at  $\varphi_{\text{eq}} > \varphi_d^{(\text{theory})}$ . To clarify this counter intuitive feature of the denser jammed packings, we analyze the rattlers for large and small particles separately in Figs. 4.5(c) and (d). Interestingly, the small particles constitute substantial portion of the rattler fraction for the entire system in both dimensions. Besides, the increase of the rattler fraction is mainly caused by the small particles especially in 3D. This trend might be the nature of the binary mixture system. To investigate this, we present the rattler fraction of the large and small particles as a function of  $R$  at  $\varphi_{\text{eq}} = 0.3$  in Fig. 4.6(a). In the monodisperse case ( $R = 1.0$ ), the rattler fraction is 2% as reported by previous studies [23,103,123]. When  $R > 1.0$ , the rattler fraction of the small particle rapidly increases, whereas that of the large particles decreases moderately and almost vanishes at  $R = 2.0$ .

To examine structure of  $R > 1.0$  closely, we compute the compositional order parameters which characterize how the large and small particles are mixed or demixed [107]. In other words, this quantifies how much the two species are phase separated. A quantity,  $f_{LL}$ , is the fraction of contacts

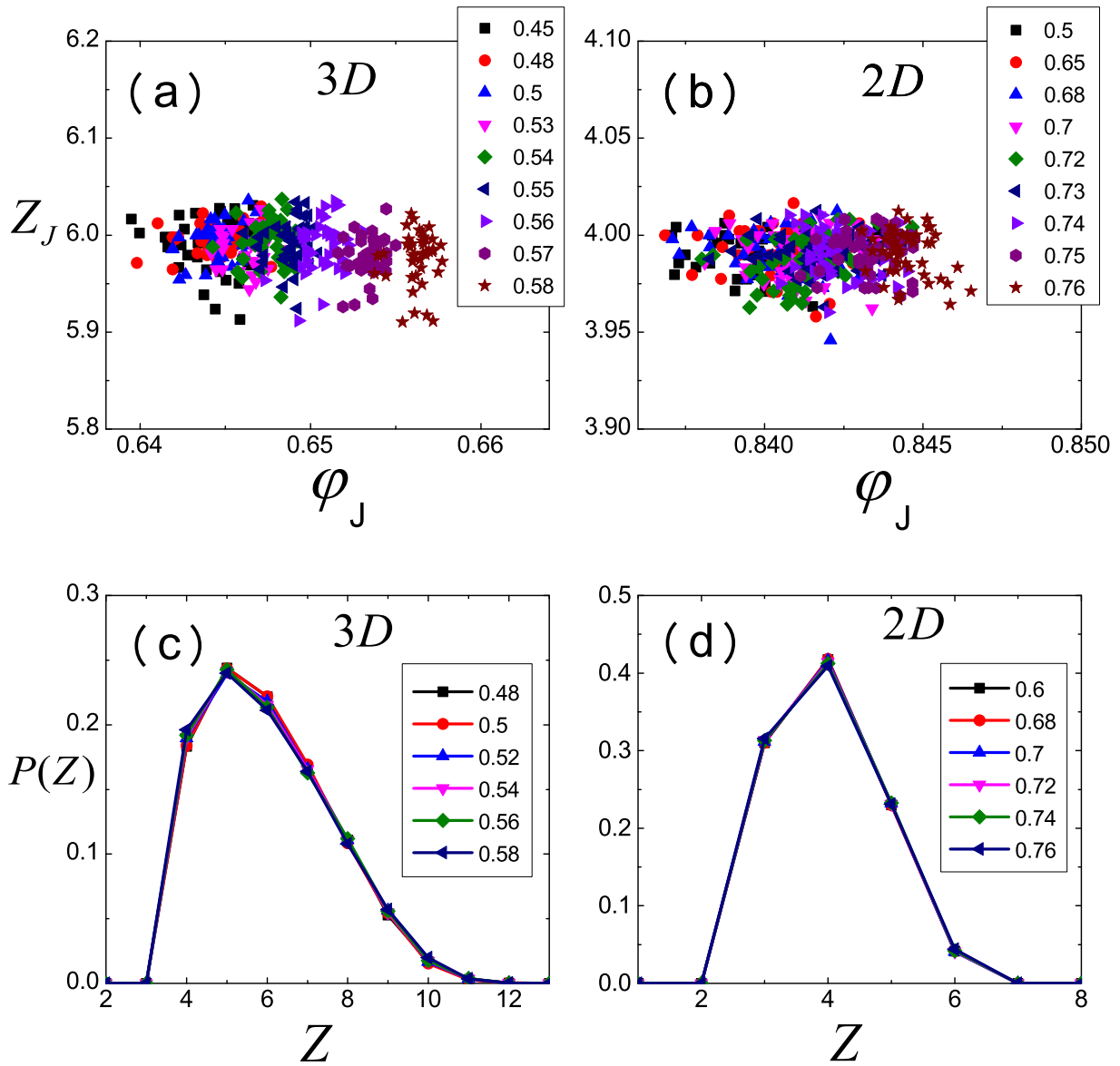


Figure 4.4: (a), (b) The scatter plot of the averaged contact number  $Z_J$  vs.  $\varphi_J$  for a configuration in 3D (a) and 2D (b). The different shapes of the points correspond to different initial volume fraction  $\varphi_{eq}$ . (c), (d) The probability distribution functions of the contact number for a particle in 3D (c) and 2D (d).

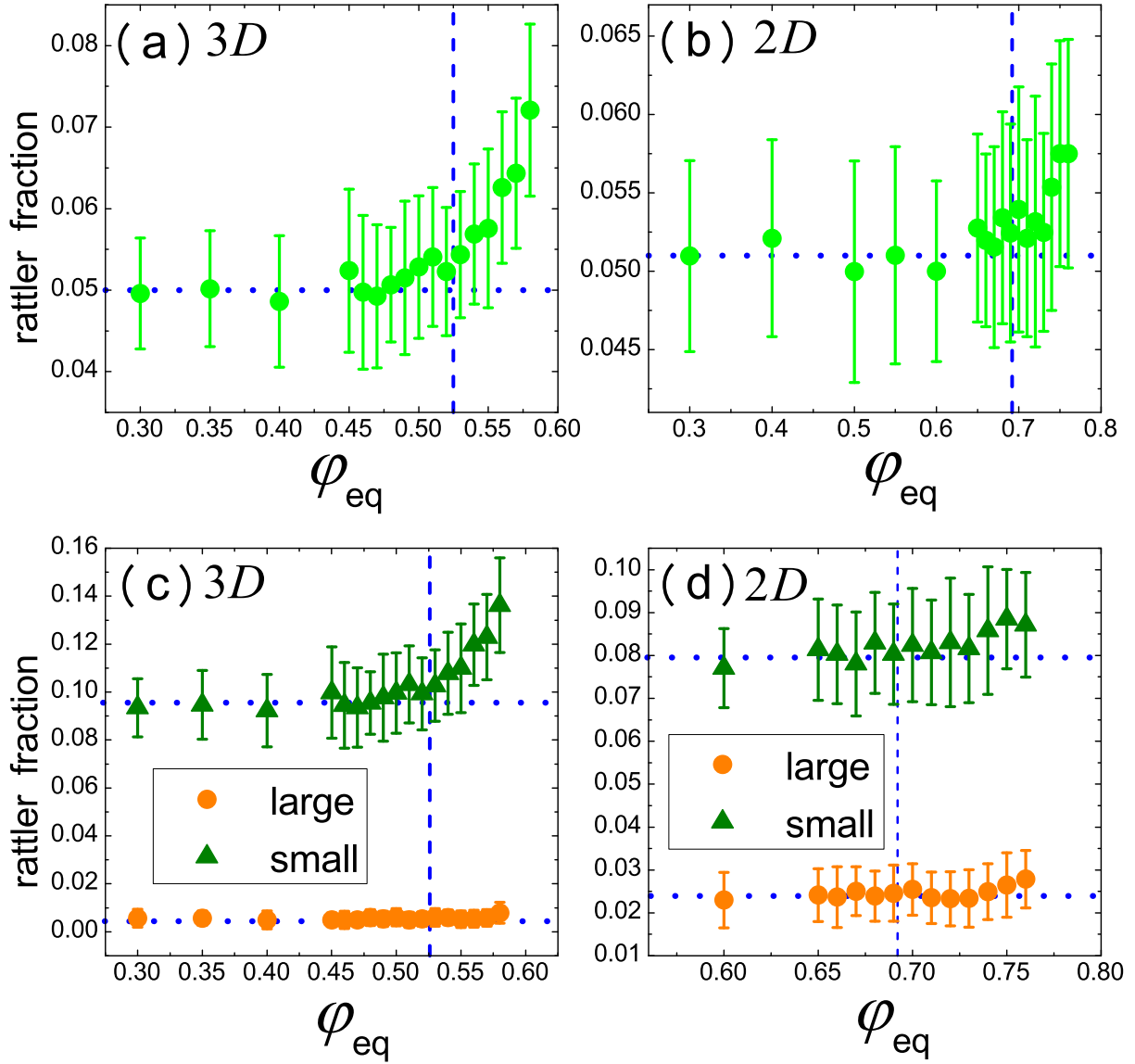


Figure 4.5: (a), (b) The rattler fraction as a function of  $\varphi_{\text{eq}}$  in 3D (a) and 2D (b). (c), (d) The rattler fraction of the large and small particles as a function of  $\varphi_{\text{eq}}$  in 3D (c) and 2D (d). The horizontal dotted lines are guides to the eye. The vertical broken lines are the positions of  $\varphi_d^{(\text{theory})}$ .

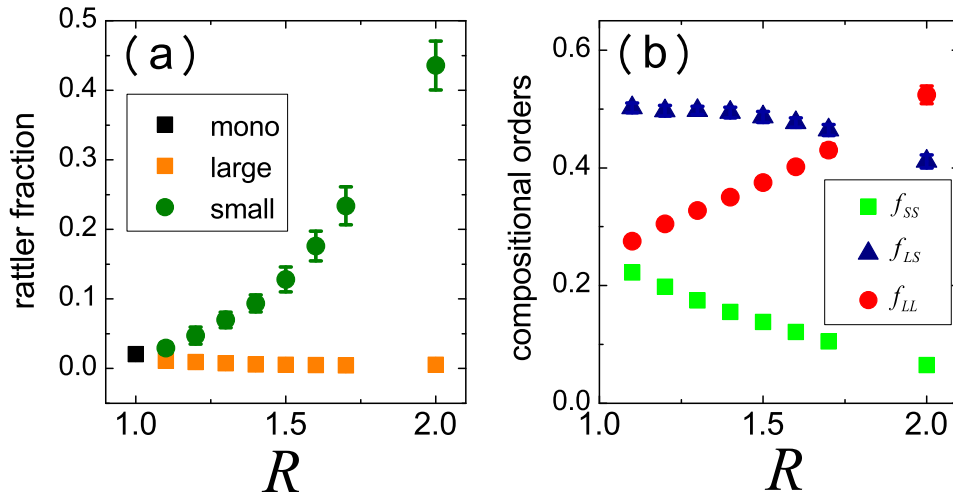


Figure 4.6: (a) The rattler fraction of the large and small particles as a function of  $R$  for  $\varphi_{\text{eq}} = 0.3$  in 3D. (b) The compositional order parameters as a function of  $R$  for  $\varphi_{\text{eq}} = 0.3$  in 3D.

of large-large particles divided by the number of the entire contacts.  $f_{LS}$  and  $f_{SS}$  are also defined in the same ways. Note that  $f_{LL} + f_{LS} + f_{SS} = 1$  always holds by definition. If the system is completely phase separated,  $f_{LS} = 0$  and  $f_{LL} + f_{SS} = 1$  hold. On the other hand, for randomly mixed configuration, one expects that  $f_{LS} = 0.5$  and  $f_{LL} + f_{SS} = 0.5$ .

We plot  $f_{LL}$ ,  $f_{LS}$ , and  $f_{SS}$  as a function of  $R$  in Fig. 4.6(b). We observe that whereas  $f_{LS}$  decreases gradually from 0.5 and  $f_{LL}$  increases with increasing  $R$ ,  $f_{SS}$  decreases. This observation suggests that the small particles tend to be surrounded by void formed by the large particles. We can speculate that these small particles become the rattlers and contribute to the increase of the rattler fraction. This speculation will be confirmed further by the analysis of the voronoi tessellation later.

It is known that  $\varphi_J$  is a critical point whose isostatic condition causes anomalous properties around the point. Here we examine a scaling property of  $Z$  and an anomalous vibrational property [23, 125, 126]. To observe the critical properties around  $\varphi_J$ , we slightly compress the system  $\varphi > \varphi_J$  by switching the hard sphere potential to the harmonic sphere one given by Eq. (4.2.2). It has been widely reported that the averaged contact number  $Z$  grows with the square root of the excess volume fraction,  $(Z - Z_J) \sim \sqrt{\varphi - \varphi_J}$ , where  $Z_J = 2d$ , when jammed configurations are compressed further [23, 101, 127]. Note that this relation is independent from spatial dimension, interaction potential between particles, and polydispersity [23]. In Figs. 4.7(a) and 4.7(b), we show the excess averaged contact number  $Z - Z_J$  as a function of  $\varphi - \varphi_J$  for various initial condition  $\varphi_{\text{eq}}$ . In both dimensions, all data points including the denser jammed packings collapse onto the straight lines with slope 0.5. Thus, we find that the denser jammed packings generated by our protocol also maintain the scaling relation of  $Z$ .

One of the striking differences between the amorphous jammed packings and the crystal packings is the excess of the low frequency normal modes [23, 125, 126]. It is well known that the density of normal mode frequencies  $D(\omega)$  of crystal structures show the Debye behavior,  $D(\omega) \sim \omega^{d-1}$  ( $\omega \rightarrow 0$ ). On the other hand,  $D(\omega)$  of the jammed packings near  $\varphi_J$  exhibits a plateau regime at low frequencies, which is called the boson peak. This feature signals excitations of low frequency modes compared to the Debye behavior and is believed to be related to unusual properties of amorphous solids such as energy transport [15]. In order to compute  $D(\omega)$  [128], we diagonalize the Hessian matrix of the potential energy. Then, we obtain  $d(N - N_r)$  eigenvalues  $e_i$  and their associated eigenvectors. Since the periodic boundary conditions are used in our systems,  $d$  eigenvalues are zero due to the translational invariance. The normal mode frequency  $\omega_i$  is given by  $\omega_i = \sqrt{e_i/N}$ . Finally,  $D(\omega)$  is obtained by  $D(\omega) = (N(\omega + \delta\omega) - N(\omega))/\delta\omega$ , where  $N(\omega)$  is the number of modes with frequencies less than or equal to  $\omega$ . In Figs. 4.7(c) and (d), we present  $D(\omega)$  of the compressed jammed packings

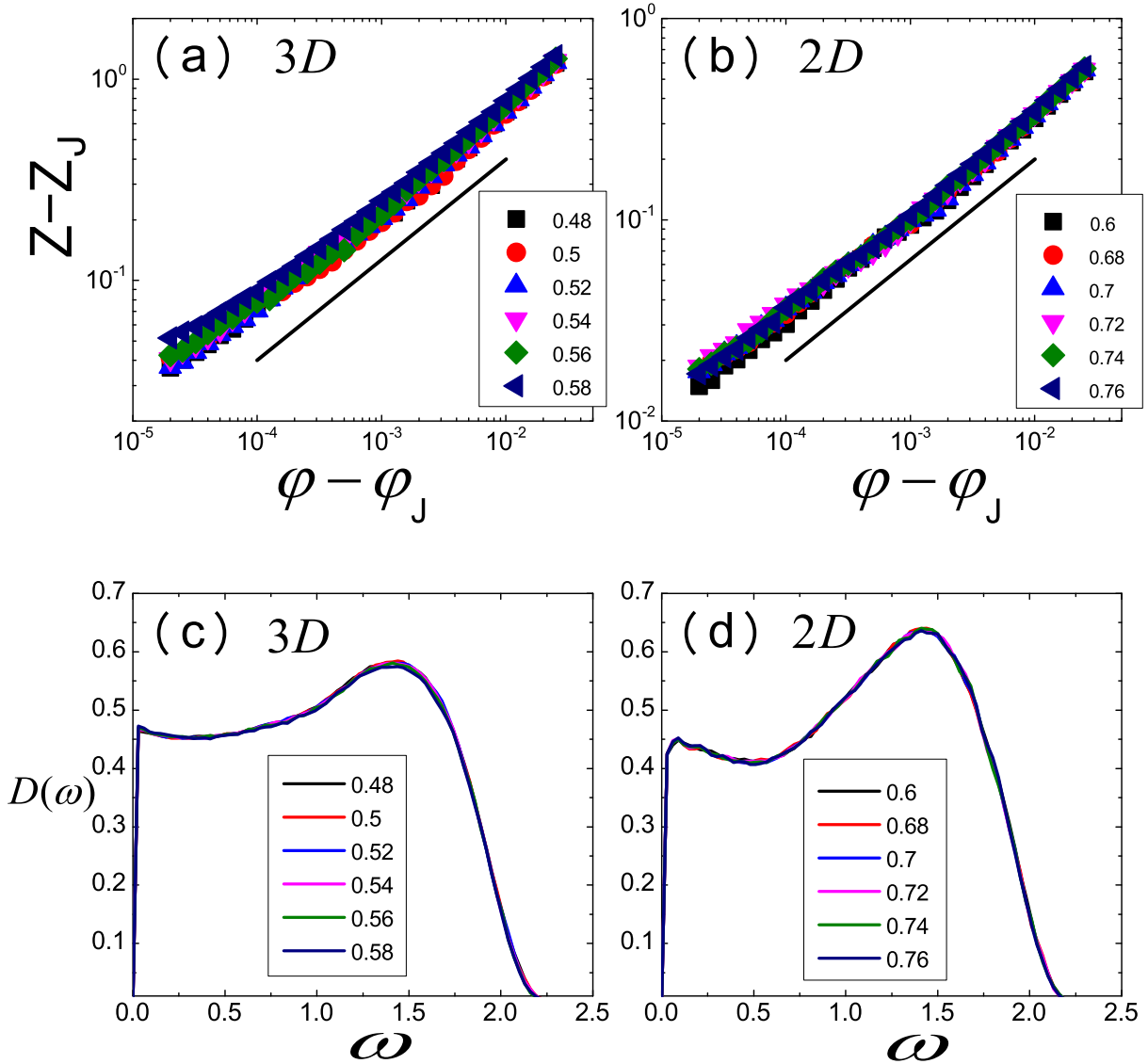


Figure 4.7: (a), (b) Excess of the averaged contact number  $Z - Z_J$  as a function of distance from the jamming transition point,  $(\varphi - \varphi_J)$ , in 3D (a) and 2D (b). The different shapes of the points correspond to different initial volume fractions  $\varphi_{eq}$ . The straight lines have slope 0.5. (c), (d) The density of normal mode frequencies  $D(\omega)$  in 3D (c) and 2D (d).  $D(\omega)$  is computed at  $(\varphi - \varphi_J) = 10^{-4}$  in both dimensions. The different colors of the lines correspond to different initial volume fractions  $\varphi_{eq}$ .

for various initial conditions  $\varphi_{\text{eq}}$ . The distance to jamming transition point is  $(\varphi - \varphi_J) = 10^{-4}$  in both dimensions. We find that the excess low frequency modes are observed in all data including denser jammed packings and the shape of  $D(\omega)$  remain unchanged. As a results, we confirm that the denser jammed packings generated by our protocol maintain usual scaling of the averaged contact number and the excess of the anomalous low frequency normal modes in the density of states.

### 4.3.3 Local structure of denser jammed packings

We have shown that  $\varphi_J$  depends on initial equilibrium volume fraction  $\varphi_{\text{eq}}$  of parent fluids, and the jamming transition points  $\varphi_J$  generated from  $\varphi_{\text{eq}} > \varphi_d^{(\text{theory})}$  are denser than conventional values [23, 100]. Naively thinking, the density of a spherical particulate system increases by introducing partial crystalline orders. In addition, one can speculate that the partial crystalline orders are accompanied by increasing of the number of pair contacts and violation of the isostatic condition. However, it have been confirmed that our denser jammed packings also maintain usual isostaticity within our numerical precision. Therefore, a following question naturally arises. How do particles construct denser configurations without partial crystallizations? To answer this question, we analyze local structure of the jammed packings and investigate mechanism of the denser amorphous configurations. In this subsection, we introduce a local jamming density by using the Voronoi tessellation and show its properties. In the following, we focus on 3D system.

To analyze the increase of the jamming transition point at a local level, we apply the Voronoi tessellation to the jammed packings and decompose the volume of the system as

$$V = \sum_{i=1}^N v_i^{(\text{voro})}, \quad (4.3.1)$$

where  $V$  is the volume of the entire system and  $v_i^{(\text{voro})}$  is the voronoi volume of  $i$ -th particle. We use a software library to carry out efficient 3D computation of the Voronoi tessellation [129]. We introduce a local jamming density  $\varphi_{J,i}^{(\text{local})}$  defined by

$$\varphi_{J,i}^{(\text{local})} = \frac{v_i^{(\text{sphere})}}{v_i^{(\text{voro})}}, \quad (4.3.2)$$

where,  $v_i^{(\text{sphere})}$  is the volume of  $i$ -th particle,  $v_i^{(\text{sphere})} = \pi\sigma_i^3/6$ .  $\sigma_i$  is the diameter of the  $i$ -th particle. First, we discuss relation between this new quantity,  $\varphi_{J,i}^{(\text{local})}$ , and  $\varphi_J$ .

For the monodisperse case ( $R=1.0$ ), the average of  $\varphi_{J,i}^{(\text{local})}$  over all particles is defined by

$$\langle \varphi_J^{(\text{local})} \rangle = \frac{1}{N} \sum_{i=1}^N \varphi_{J,i}^{(\text{local})} = \frac{1}{N} \sum_{i=1}^N \frac{v_i^{(\text{sphere})}}{v_i^{(\text{voro})}} = \frac{v_0^{(\text{sphere})}}{N} \sum_{i=1}^N \frac{1}{v_i^{(\text{voro})}}, \quad (4.3.3)$$

where,  $v_0^{(\text{sphere})} = v_1^{(\text{sphere})} = v_2^{(\text{sphere})} = \dots = v_N^{(\text{sphere})}$ . In general,  $\langle \varphi_J^{(\text{local})} \rangle$  and  $\varphi_J$  are not same. They satisfy the relationship between the harmonic average and the arithmetic average,  $\langle \varphi_J^{(\text{local})} \rangle \geq \varphi_J$ . Because,  $\varphi_J$  is decomposed by

$$\varphi_J = \frac{\sum_{i=1}^N v_i^{(\text{sphere})}}{\sum_{i=1}^N v_i^{(\text{voro})}} = \frac{N v_0^{(\text{sphere})}}{\sum_{i=1}^N v_i^{(\text{voro})}}. \quad (4.3.4)$$

From Eq. (4.3.3) and (4.3.4), one can easily prove  $\langle \varphi_J^{(\text{local})} \rangle \geq \varphi_J$ . Actually, we obtain  $\langle \varphi_J^{(\text{local})} \rangle = 0.637$  and  $\varphi_J = 0.635$  for  $N = 1024$  with  $R = 1.0$  (see Fig. 4.10 (a)). Note that the equality is attained if and only if  $v_1^{(\text{voro})} = v_2^{(\text{voro})} = \dots = v_N^{(\text{voro})}$ .

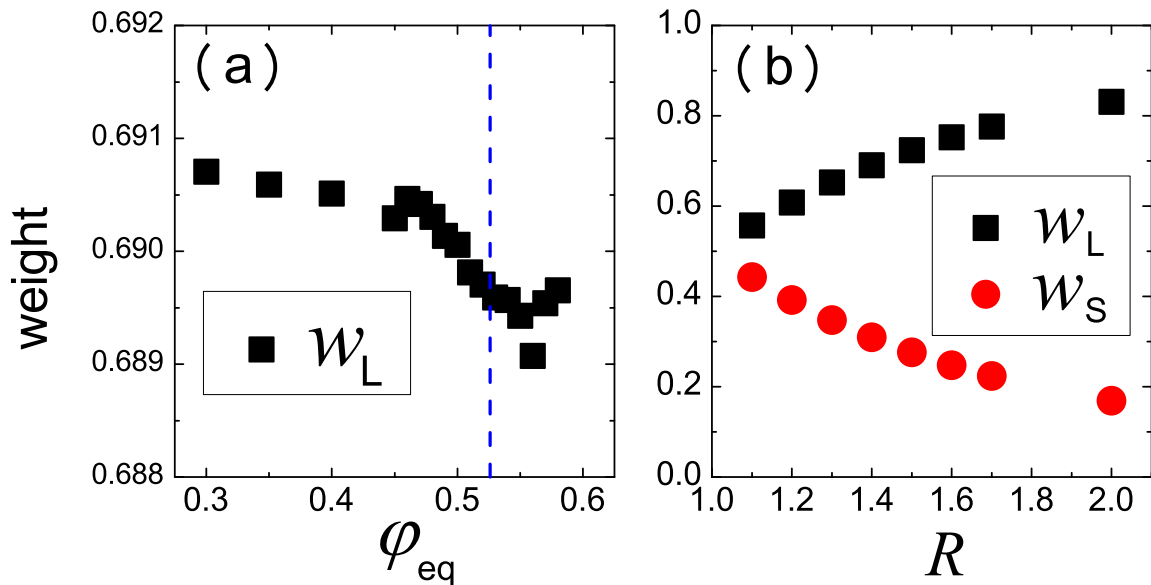


Figure 4.8: (a)  $w_L$  as a function of  $\varphi_{\text{eq}}$  with  $R = 1.4$ . Since  $w_L + w_S = 1$  holds, we only plot  $w_L$ . (b)  $w_L$  and  $w_S$  as a function of  $R$  for  $\varphi_{\text{eq}} = 0.3$ .

When  $R > 1.0$ , or the system is the binary mixture, a caution must be taken, because contribution of the large and small species to the volume fraction of the entire system are different. Thus, we must introduce the weights of voronoi volume of the large and small species as

$$\langle \varphi_J^{(\text{local})} \rangle = w_L \langle \varphi_J^{(\text{local})} \rangle_L + w_S \langle \varphi_J^{(\text{local})} \rangle_S, \quad (4.3.5)$$

where  $w_L = V_L/V$  and  $w_S = V_S/V$  are the fractions of the volume of the large and small species respectively.  $V_L$  and  $V_S$  are obtained by  $V_L = \sum_{i \in L} v_i^{(\text{voro})}$  and  $V_S = \sum_{i \in S} v_i^{(\text{voro})}$ , respectively.  $V = V_L + V_S$  always holds by definition.  $\langle \varphi_J^{(\text{local})} \rangle_L$  and  $\langle \varphi_J^{(\text{local})} \rangle_S$  are the average of the large and small particles, respectively. Fig. 4.8 show that the  $\varphi_{\text{eq}}$  and  $R$  dependence of  $w_L$  and  $w_S$ . We notice that  $w_L = w_S = 0.5$  (for  $R = 1.0$ ) split into  $w_L > w_S$  when  $R$  increases in Fig. 4.8(b). This indicates that the large particles dominate in contribution to the volume fraction of the entire system in highly asymmetric binary mixture. We also find that  $w_L$  hardly changes ( $w_L \simeq 0.69$ ) when  $\varphi_{\text{eq}}$  increases in Fig. 4.8(a).

In Figs. 4.9 and 4.10, the averages of  $\varphi_{J,i}^{(\text{local})}$  for the total, large, and small particles as a function of  $\varphi_{\text{eq}}$  and  $R$  [130] are shown. We confirm that the averages of newly introduced quantity,  $\varphi_{J,i}^{(\text{local})}$  trace the functional form of  $\varphi_J(N)$  as shown in Figs. 4.9 (a) and 4.10 (a). The probability distribution functions of  $\varphi_{J,i}^{(\text{local})}$  are shown in Figs. 4.9(d) and 4.10(d). We find that these probability distribution functions are bell-shaped. Figs. 4.10(b) and (c) show that whereas the local jamming density of the large particles increases with increasing  $R$ , that of the small particles decreases. This feature also indicates that the small particles tend to be surrounded by voids formed by the large particles in highly asymmetric binary mixtures.

These results shown in Figs. 4.9 and 4.10 justify the prescription of Eq. (4.3.5) and allow us to discuss the increase of the density of the jammed packings in terms of  $\varphi_{J,i}^{(\text{local})}$ . Hereafter, we investigate the mechanism of the denser jammed packings by using  $\varphi_{J,i}^{(\text{local})}$ . Especially, we examine correlation between  $\varphi_{J,i}^{(\text{local})}$  and some geometrical features such as the bond-orientational order and the locally preferred structures.

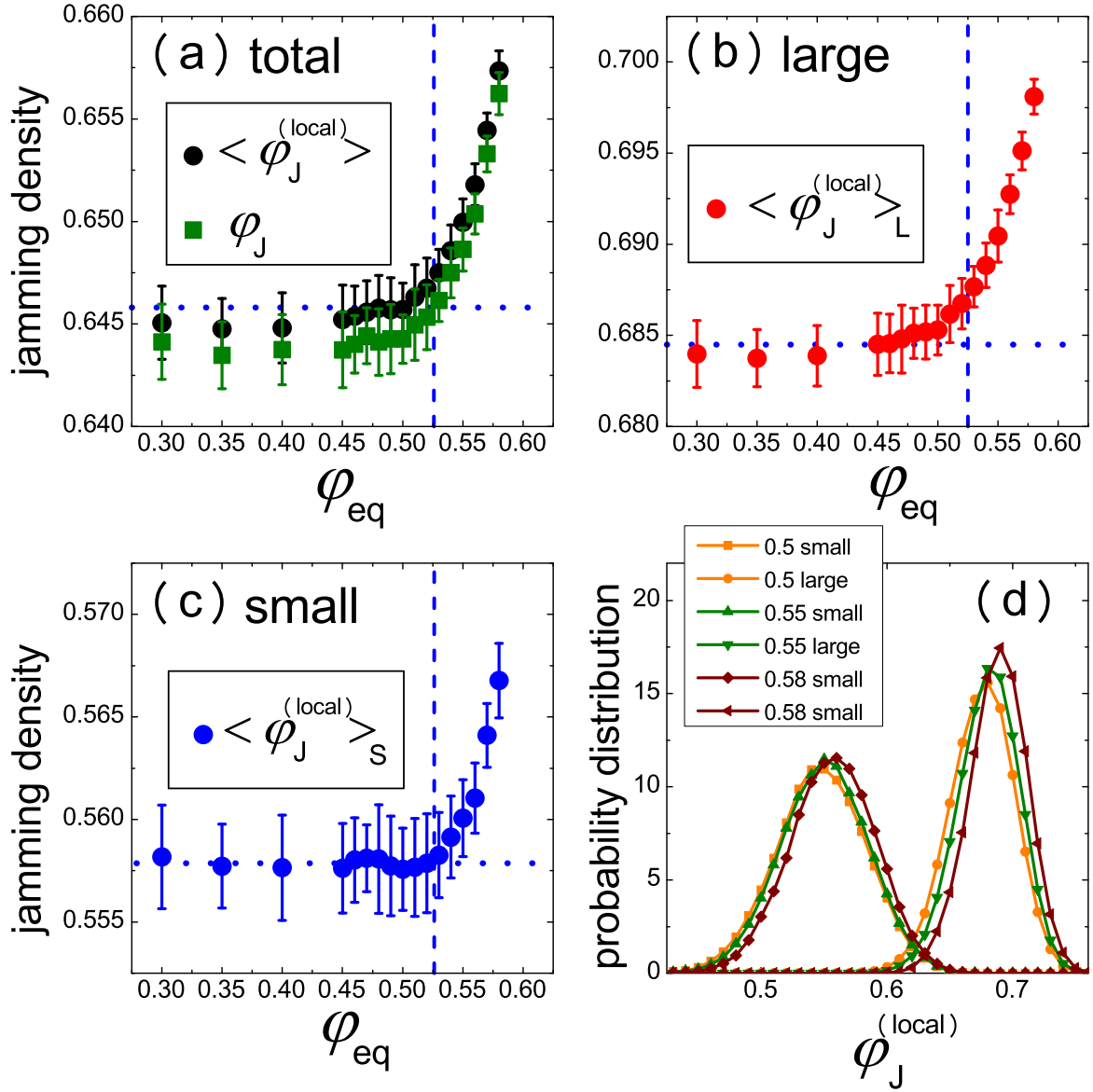


Figure 4.9: (a) - (c) The average of  $\varphi_{J,i}^{(local)}$  over total (a), large (b), and small (c) particles with  $R = 1.4$  as a function of  $\varphi_{eq}$ .  $\varphi_J(N)$  for  $N = 1024$  is also plotted in (a). The vertical dashed lines are the positions of  $\varphi_d^{(theory)}$ . The horizontal dotted lines are guides to the eye. (d) The probability distribution function of  $\varphi_{J,i}^{(local)}$  for the large (right peak) and small (left peak) particles with  $R = 1.4$ .

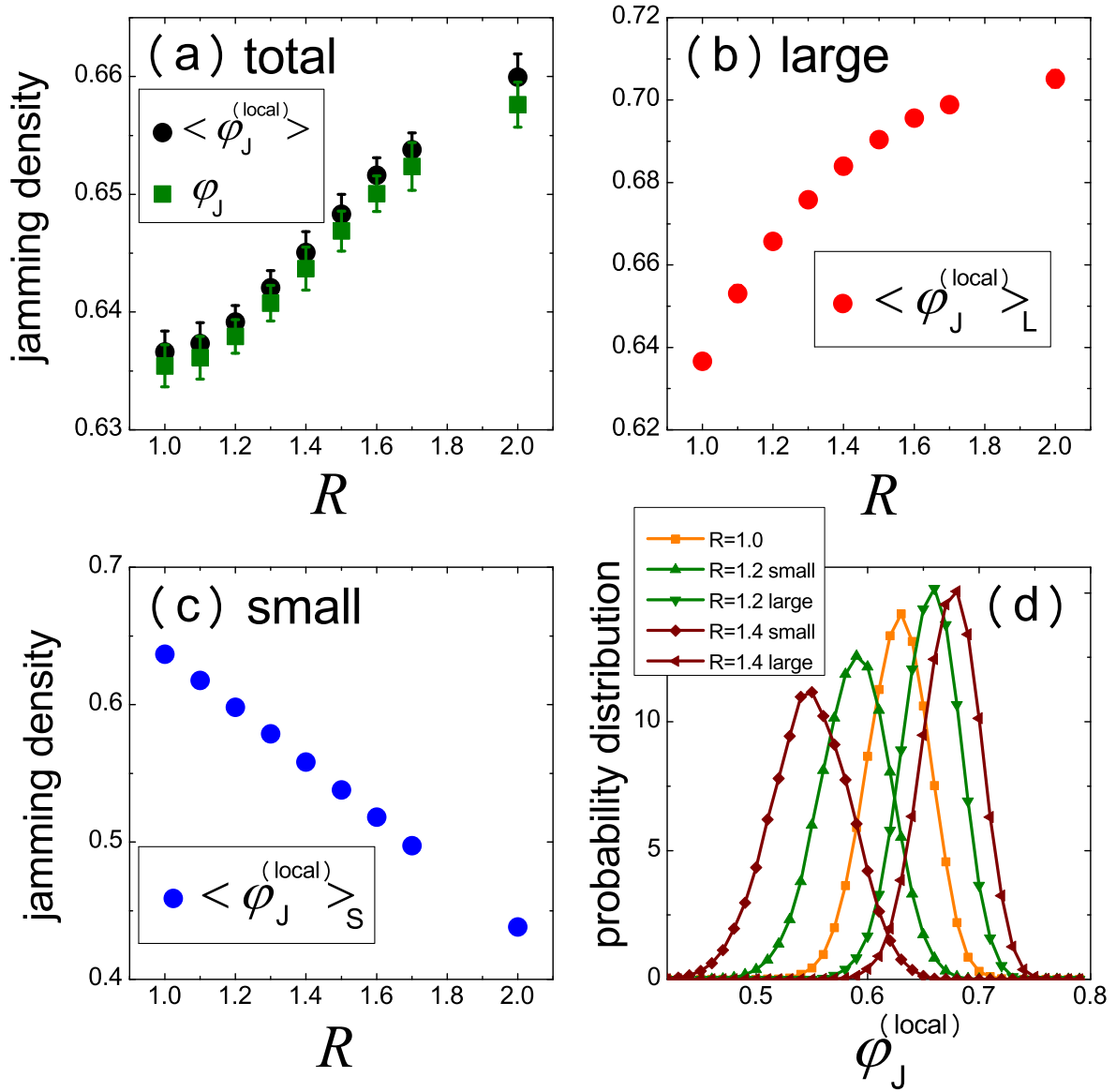


Figure 4.10: (a) - (c) The average of  $\phi_{J,i}^{(local)}$  over total (a), large (b), and small (c) particles at  $\varphi_{eq} = 0.3$  as a function of  $R$ .  $\phi_J(N)$  for  $N = 1024$  is also plotted in (a). (d) The probability distribution function of  $\phi_{J,i}^{(local)}$  at  $\varphi_{eq} = 0.3$ . The single peak at  $R = 1.0$  splits into the right (the large particles) and the left (the small particles) peaks for  $R > 1.0$ .

#### 4.3.4 Bond orientational order

In general, the density of crystalline configurations is higher than that of amorphous configurations in 2D and 3D. Therefore, one might speculate that local crystalline configurations are found at the denser jammed packings. To examine the correlation between the increase of  $\varphi_J$  and the growth of the crystalline order in the jammed packings, we employ the bond-orientational order (BOO) parameter [131, 132] which quantify the degree of crystallinity of the system. We compute the BOO parameter for the  $i$ -th particle given by

$$Q_{6,i} = \left( \frac{4\pi}{13} \sum_{m=-6}^6 \left| \frac{1}{n_b^i} \sum_{j=1}^{n_b^i} Y_{l=6,m}(\mathbf{r}_{ij}) \right| \right)^{1/2}, \quad (4.3.6)$$

where  $n_b^i$  is the number of the nearest neighbors of the  $i$ -th particle, and  $Y_{l,m}(\mathbf{r}_{ij})$  is the spherical harmonics of the degree  $l$  and the order  $m$ . We set  $l = 6$  since this choice is known for the best number to characterize the close packed structure in 3D (face-centered cubic) [131]. In this thesis, we define the nearest neighbors based on the Voronoi tessellation. We present the averaged  $Q_{6,i}$  as a function of  $\varphi_{\text{eq}}$  for the total, large, and small particles in Fig. 4.11(a), (b), and (c), respectively. At low  $\varphi_{\text{eq}}$ ,  $Q_{6,i}$ 's are almost constant but abruptly start increasing at high  $\varphi_{\text{eq}}$ , and the onset volume fractions are found to be close to  $\varphi_d^{(\text{theory})}$ .

Since the averaged  $Q_{6,i}$ 's behave in much the same way as  $\langle \varphi_J^{(\text{local})} \rangle$  in Fig. 4.9(a), (b), and (c), one may conclude that the increment of the local BOO directly relates to the denser jamming transition points. However, it has been reported that the BOO parameter is not always applicable to characterize the crystalline order in amorphous configurations when the system is the binary mixture [133]. Therefore, to examine availability of the BOO parameter for the binary case ( $R > 1.0$ ), we plot  $Q_{6,i}$  vs.  $\varphi_J^{(\text{local})}$  correlation maps for several  $R$ 's in Fig. 4.12. At the same time, we calculate the Pearson's correlation coefficients in Fig. 4.13. We find that the correlation between  $Q_{6,i}$  and  $\varphi_J^{(\text{local})}$  is the highest at  $R = 1.0$  (monodisperse case), but the correlation rapidly decreases with increasing  $R$  and, eventually, becomes almost zero at  $R = 2.0$  for both large and small particles. For  $R = 1.4$  where we intensively use in this study, the correlation coefficients are relatively low values, 0.26 and 0.20 for the large and small particles, respectively. Interestingly, these correlation coefficients decrease further at high  $\varphi_{\text{eq}}$  region in Fig. 4.13 (a). This trend is opposite to the increase of the jamming transition points in Fig. 4.2 (a) and Fig. 4.9. Therefore, we conclude that, although the BOO parameter can capture the abrupt change of the configurations at  $\varphi_d^{(\text{theory})}$ , it is not proper quantity to argue the increase of the jamming density for the binary hard sphere systems such as  $R = 1.4$  case, and alternative ways of characterizing the variation of the density of the jammed packings are required.

#### 4.3.5 Hidden onset of growth of locally preferred structures

Here we employ the locally preferred structure (LPS) approach using statistics of the Voronoi polyhedra [37, 134] to investigate the relationship between the denser jamming transition points and their local structures. In this approach, the structure of a particle is characterized by the Voronoi polyhedra with a given signature  $(n_3, n_4, n_5, \dots)$ , where  $n_k$  is the number of faces of the polyhedron with a given number  $k$  of the vertices, and the fraction of the Voronoi polyhedra is monitored. In this thesis, we define the LPS by the top six most frequent Voronoi polyhedra of the hard sphere, whereas Coslovich [134] defines it as the most frequent Voronoi polyhedron of the Lennard-Jones (LJ) and its variant around only the small particles.

The top six most frequent signatures of the Voronoi polyhedra around the large and small particles from the equilibrium configurations (EQ) and the jamming configurations (IS) for  $R = 1.4$  are reported in Table 4.1 and 4.2, respectively. Similar to the the LJ mixtures and its variant, the fractions of the Voronoi polyhedra for the small particles are larger than that of the large particles. In both Table 4.1 and 4.2, one observes that members of the top six most frequent Voronoi polyhedra, or LPSs, of the

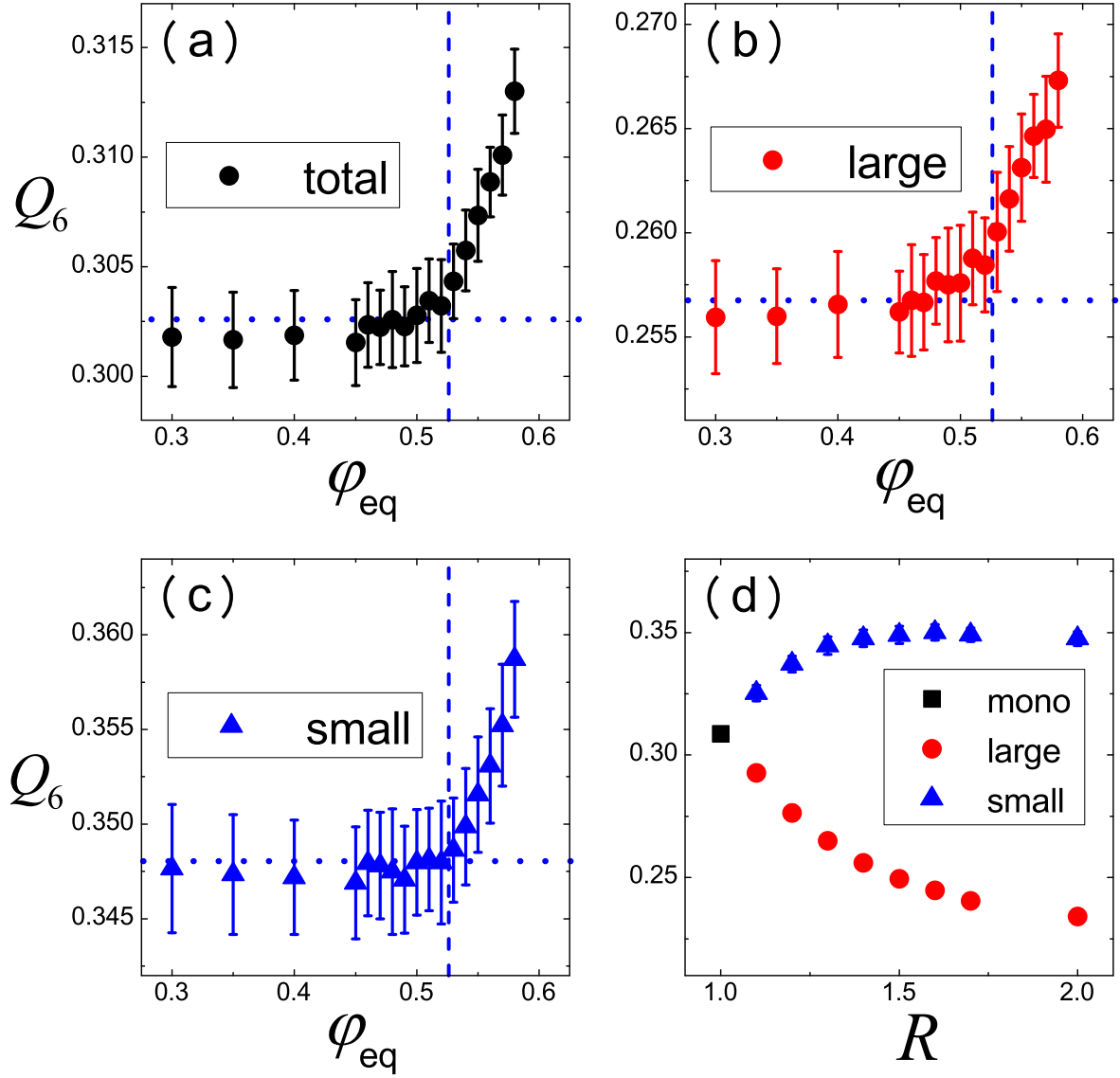


Figure 4.11: (a) - (c) The averaged  $Q_{6,i}$  for total (a), large (b), and small (c) particles with  $R = 1.4$  as a function of  $\varphi_{\text{eq}}$ . The vertical dashed lines are the positions of  $\varphi_d^{(\text{theory})}$ . The horizontal dotted lines are guides to the eye. (d) The averaged  $Q_{6,i}$  for total, large, and small particles at  $\varphi_{\text{eq}} = 0.30$  as a function of  $R$ .

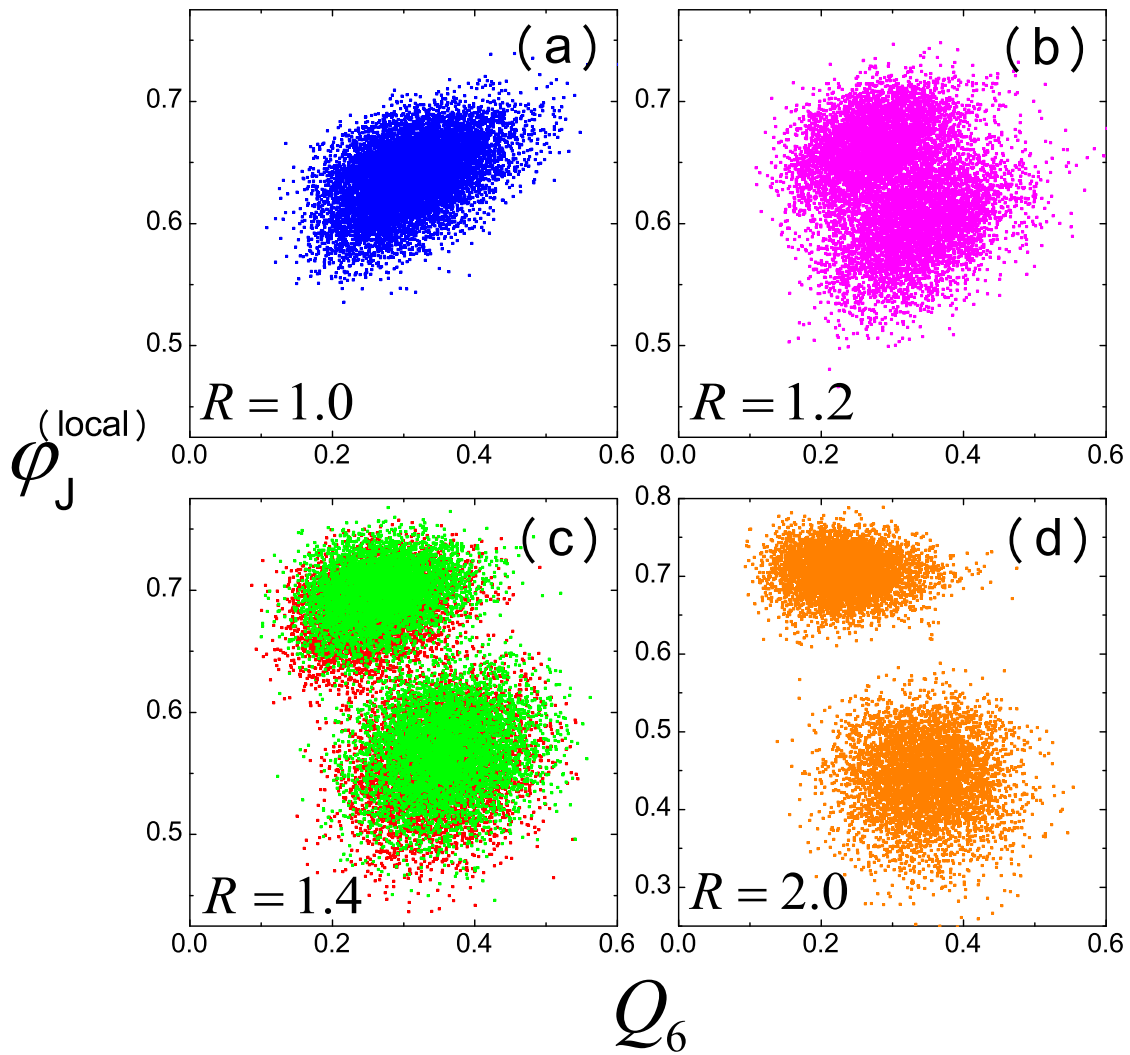


Figure 4.12: (a) - (d) The correlation between  $Q_{6,i}$  and  $\varphi_J^{(\text{local})}$  for  $R = 1.0$  (a),  $R = 1.2$  (b),  $R = 1.4$  (c), and  $R = 2.0$  (d). In (a), (b), and (d),  $\varphi_{\text{eq}} = 0.30$  is used. In (c), two different initial conditions,  $\varphi_{\text{eq}} = 0.50$  (red points) and  $\varphi_{\text{eq}} = 0.58$  (green points), are shown.

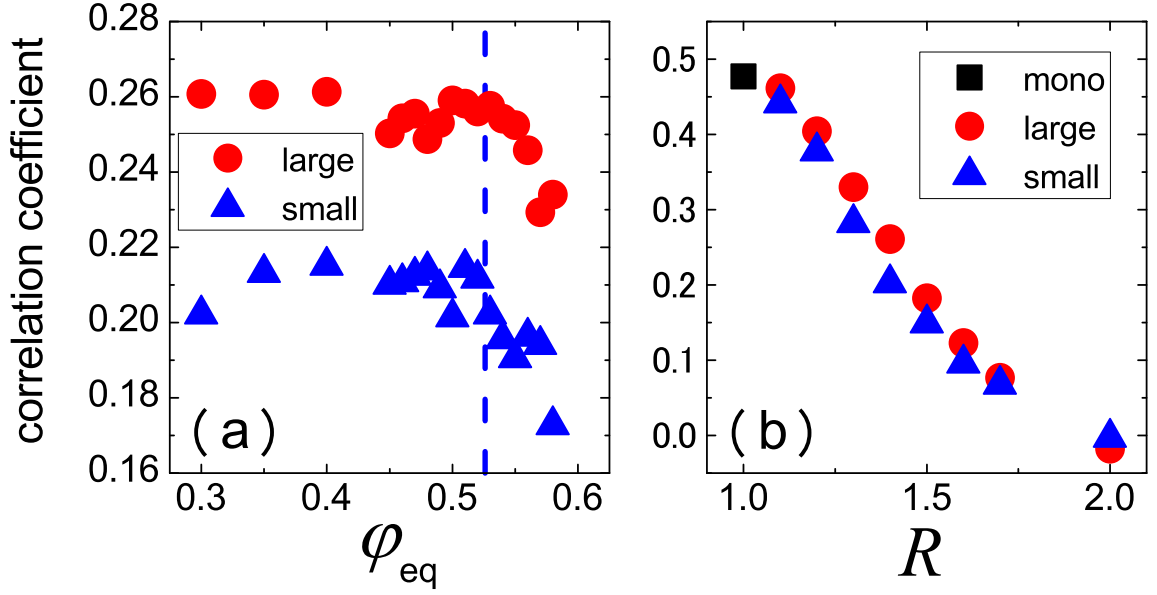


Figure 4.13: (a) The correlation coefficients of the large and small particles as a function of  $\varphi_{eq}$  with  $R = 1.4$  (b) The correlation coefficients of the large and small particles as a function of  $R$  at  $\varphi_{eq} = 0.3$

Table 4.1: The top six most frequent signatures of the Voronoi polyhedra around large particles from the equilibrium configurations (EQ) and the jammed packings (IS).

	$\varphi_{eq}=0.45$		$\varphi_{eq}=0.50$		$\varphi_{eq}=0.55$		$\varphi_{eq}=0.58$	
	signature	%	signature	%	signature	%	signature	%
EQ	(1,3,5,5)	1.3	(0,2,8,5)	2.2	(0,2,8,5)	3.9	(0,2,8,5)	5.4
	(0,3,6,6)	1.3	(0,3,6,6)	2.0	(0,2,8,6)	3.5	(0,2,8,6)	5.2
	(0,3,7,4)	1.2	(0,2,8,4)	1.8	(0,3,6,6)	3.0	(0,1,10,4)	4.3
	(0,2,8,4)	1.2	(0,3,7,5)	1.7	(0,1,10,4)	2.8	(0,1,10,5)	3.9
	(0,3,7,5)	1.2	(0,2,8,6)	1.6	(0,2,8,4)	2.5	(0,3,6,6)	3.4
	(0,2,8,5)	1.1	(1,3,5,5)	1.5	(0,1,10,5)	2.3	(0,2,8,4)	3.0
IS	(0,2,8,5)	2.7	(0,2,8,5)	3.0	(0,2,8,5)	3.8	(0,2,8,6)	4.9
	(0,2,8,6)	2.5	(0,2,8,6)	2.8	(0,2,8,6)	3.4	(0,2,8,5)	4.9
	(0,3,6,6)	2.2	(0,3,6,6)	2.5	(0,3,6,6)	2.8	(0,1,10,4)	3.6
	(0,3,7,5)	2.1	(0,3,7,5)	1.9	(0,1,10,4)	2.8	(0,1,10,5)	3.3
	(0,3,6,7)	1.8	(0,1,10,4)	1.8	(0,1,10,5)	2.3	(0,3,6,6)	3.2
	(0,2,8,4)	1.8	(0,2,8,4)	1.8	(0,2,8,4)	2.2	(0,3,6,7)	3.1

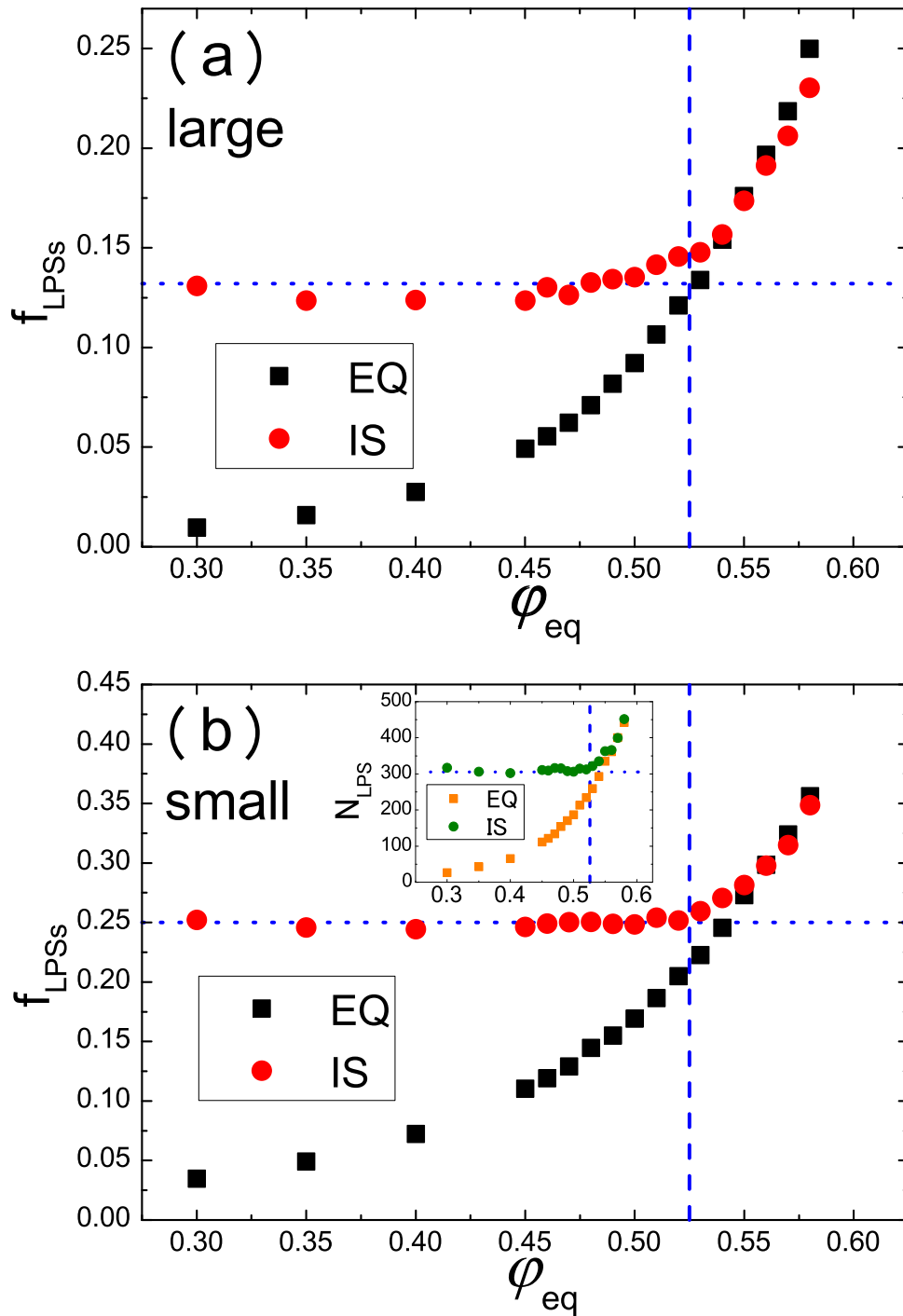


Figure 4.14: (a), (b)  $f_{LPSs}$  as a function of  $\varphi_{eq}$  for large (a) and small (b) particles. The inset in (b) shows  $\varphi_{eq}$  dependence of  $N_{LPS}$ . The vertical broken lines are the positions of  $\varphi_d^{(theory)}$ . The horizontal dotted lines are guides to the eye.

Table 4.2: The top six most frequent signatures of the Voronoi polyhedra around small particles from the equilibrium configurations (EQ) and the jammed packings (IS).

	$\varphi_{\text{eq}}=0.45$		$\varphi_{\text{eq}}=0.50$		$\varphi_{\text{eq}}=0.55$		$\varphi_{\text{eq}}=0.58$	
	signature	%	signature	%	signature	%	signature	%
EQ	(0,3,6,3)	2.8	(0,3,6,3)	3.8	(0,2,8,1)	6.6	(0,2,8,1)	9.4
	(0,3,6,4)	2.3	(0,2,8,1)	3.4	(0,2,8,2)	5.9	(0,2,8,2)	8.2
	(1,3,4,3)	2.0	(0,2,8,2)	3.3	(0,3,6,3)	5.2	(0,3,6,3)	6.1
	(0,4,4,3)	2.0	(0,3,6,4)	3.2	(0,3,6,4)	4.3	(0,3,6,4)	4.9
	(0,2,8,2)	2.0	(0,4,4,4)	2.5	(0,4,4,4)	2.9	(0,2,8,0)	3.9
	(0,2,8,1)	1.9	(0,4,4,3)	2.4	(1,2,5,4)	2.9	(1,2,5,3)	3.2
IS	(0,2,8,1)	6.1	(0,2,8,1)	6.1	(0,2,8,1)	7.5	(0,2,8,1)	9.7
	(0,3,6,3)	4.9	(0,3,6,3)	5.2	(0,2,8,2)	5.5	(0,2,8,2)	7.3
	(0,2,8,2)	4.4	(0,2,8,2)	4.4	(0,3,6,3)	5.3	(0,3,6,3)	6.1
	(0,3,6,4)	3.4	(0,3,6,4)	3.3	(0,3,6,4)	3.7	(0,2,8,0)	4.5
	(0,4,4,3)	3.3	(0,4,4,4)	3.1	(0,4,4,4)	3.2	(0,3,6,4)	3.8
	(0,4,4,4)	3.0	(0,4,4,3)	3.1	(0,2,8,0)	3.1	(1,2,5,3)	3.4

EQ and IS are different at low  $\varphi_{\text{eq}}$ . However, these members become similar between the EQ and IS at high  $\varphi_{\text{eq}}$ . This fact suggests that the IS strongly affects the configurations of the EQ at high  $\varphi_{\text{eq}}$ .

To examine this observation closely, we calculate the  $\varphi_{\text{eq}}$ -dependence of the fraction of the LPSs. We define  $f_{\text{LPSs}}$  as the sum of the fractions of the top six Voronoi polyhedra of the IS at  $\varphi_{\text{eq}} = 0.58$  at which the highest equilibrium volume fraction for this study. We present the growth of  $f_{\text{LPSs}}$  for the EQ and IS as a function of  $\varphi_{\text{eq}}$  for the large and small particles in Fig. 4.14(a) and (b), respectively. We find that  $f_{\text{LPSs}}$  of the EQ monotonically increases with  $\varphi_{\text{eq}}$ , whereas  $f_{\text{LPSs}}$  of the IS remains constant at  $\varphi_{\text{eq}} < \varphi_d^{(\text{theory})}$  but abruptly increases at  $\varphi_d^{(\text{theory})}$  in both the large and small particles. Besides,  $f_{\text{LPSs}}$  of the EQ and IS are almost match quantitatively at  $\varphi_{\text{eq}} > \varphi_d^{(\text{theory})}$ . This fact suggests that configurations of the EQ, or parent fluids, are strongly influenced by their IS at  $\varphi_{\text{eq}} > \varphi_d^{(\text{theory})}$ . The sudden increase of  $f_{\text{LPSs}}$  for the IS, which is not observed for the EQ, suggests that the onset of the growth of the LPSs is hidden in the IS.

We also examine the LPS domain  $N_{\text{LPS}}$  which has been introduced by Coslovich *et al.* [37, 134].  $N_{\text{LPS}}$  is defined by the number of particles sitting either at the center or on the vertices of face-sharing polyhedra with the most frequent Voronoi polyhedron around the small particles. In the inset of Fig. 4.14 (b), we show  $N_{\text{LPS}}$  as a function of  $\varphi_{\text{eq}}$ . We find that  $N_{\text{LPS}}$  increases in a similar fashion of  $f_{\text{LPSs}}$  as  $\varphi_{\text{eq}}$  increases.

The synchronized change of  $\varphi_J$  in Fig. 4.2 and  $f_{\text{LPSs}}$  or  $N_{\text{LPS}}$  for the IS in Fig. 4.14 suggests that the growth of the fraction of the LPSs may be a main contribution to the denser jamming transition points. To clarify this speculation, we decompose  $\langle \varphi_J^{(\text{local})} \rangle_L$  and  $\langle \varphi_J^{(\text{local})} \rangle_S$  in Eq. (4.3.5) into the contribution of the three frequent signatures of the Voronoi polyhedra which show markedly growth in Table 4.1 and 4.2 and the others as

$$\langle \varphi_J^{(\text{local})} \rangle_\alpha = \sum_l S_{\alpha,l} + S_{\alpha,\text{others}}, \quad (4.3.7)$$

where  $\alpha = L, S$ , and  $l = 1, 2, 3$  specifies the three most frequent signatures of the Voronoi polyhedra: (0, 2, 8, 6), (0, 2, 8, 5), and (0, 1, 10, 4) for the large particles, and (0, 2, 8, 1), (0, 2, 8, 2), and (0, 3, 6, 3) for the small particles, respectively.  $S_{\alpha,l}$  is the contribution from the  $l$ -th LPS,

$$S_{\alpha,l} = \frac{1}{N_\alpha} \sum_{i_i=1}^{N_{\alpha,l}} \varphi_{J,i_i}^{(\text{local})}. \quad (4.3.8)$$

where  $N_{\alpha,l}$  is the number of particles belonging to the  $l$ -th LPS with species  $\alpha$ , and  $S_{\alpha,\text{others}}$  is the contribution from the others.

In Fig. 4.15, we show Eq. (4.3.7) as stacked bars for the large (a) and small (b) particles at  $\varphi_{\text{eq}} = 0.50, 0.55, \text{ and } 0.58$ . The heights of the stacked bars correspond to the data in Figs. 4.9 (b) and (c). This representation enables us to see the increase of the jamming density in terms of the growth of the LPSs. Fig. 4.15 directly shows that the denser jamming transition points generated from  $\varphi_{\text{eq}} > \varphi_d^{(\text{theory})}$  are achieved by the growth of the LPSs.

Here we mention a recent study related to the LPS approach. Interestingly, our conclusion is similar to the feature of a recent simulation study of the ultrastable glasses [135]. Singh *et al.* have found that a couple of the Voronoi polyhedra in the ultrastable glasses are more abundant than that of ordinary glasses. These Voronoi polyhedra found in the ultrastable glasses may be energetically favored structures, whereas the LPS in the jamming configurations are entropically favored structures.

## 4.4 Conclusion

In this Chapter, we have presented numerical evidence that the protocol dependence of  $\varphi_J$  is a natural consequence of the RFOT scenario. By employing the packing algorithm developed in the soft particle systems for the hard sphere potential systems, we have numerically investigated the dependence of  $\varphi_J$  on the initial configurations of the parent fluids equilibrated at  $\varphi_{\text{eq}}$ . We have found that  $\varphi_J$  remains constant when  $\varphi_{\text{eq}} < \varphi_d^{(\text{theory})}$  but sharply increases when  $\varphi_{\text{eq}}$  exceeds  $\varphi_d^{(\text{theory})}$  in both three and two dimensions. It has been emphasized that the onset of the increase of  $\varphi_J$  is obviously much lower than  $\varphi_d^{(\text{fit})}$  obtained from the fitting of the structural relaxation data. We have confirmed that the denser  $\varphi_J$ 's generated by our protocol also maintain the isostaticity, the scaling of the averaged contact numbers, and the excess of the low frequency normal modes within our numerical precision. In addition, the growth of the fraction of the rattlers has been shown and explained as a particular effect of the binary system.

In order to clarify the nature of the denser jammed packings, or the mechanism of the efficient amorphous packings, we have introduced the local jamming density,  $\varphi_{J,i}^{(\text{local})}$ , and analyzed its correlation with the BOO parameter. We have found that the tiny growth of the BOO parameter is not directly related to the increase of  $\varphi_J$  at least the binary sphere system with the size ratio  $R = 1.4$ . To describe the denser jammed packings, we have measured the LPS as the frequent signatures of the Voronoi polyhedra. We have found that the denser jammed packings generated from  $\varphi_{\text{eq}} > \varphi_d^{(\text{theory})}$  are consist of the several LPSs.

The results of this Chapter indicates that the LPS approach is useful to characterize the jammed packings and can be a proper order metric for the amorphous systems. It has been recognized that common order metrics such as the BOO parameters and the translation order parameters are related to the use of a particular reference configuration in their design [103]. For example, the BOO parameters are designed to detect the sign of the crystalline order in a packing, but they are insensitive to emergence of other types of order. Thus, the BOO parameters fail to characterize the order inside random configurations. However, the LPS approach utilizes the fraction of the frequent Voronoi polyhedra and does not depend on any kind of reference systems. The application of the LPS approach to design of the order metric of the amorphous system can be a promising future problem.

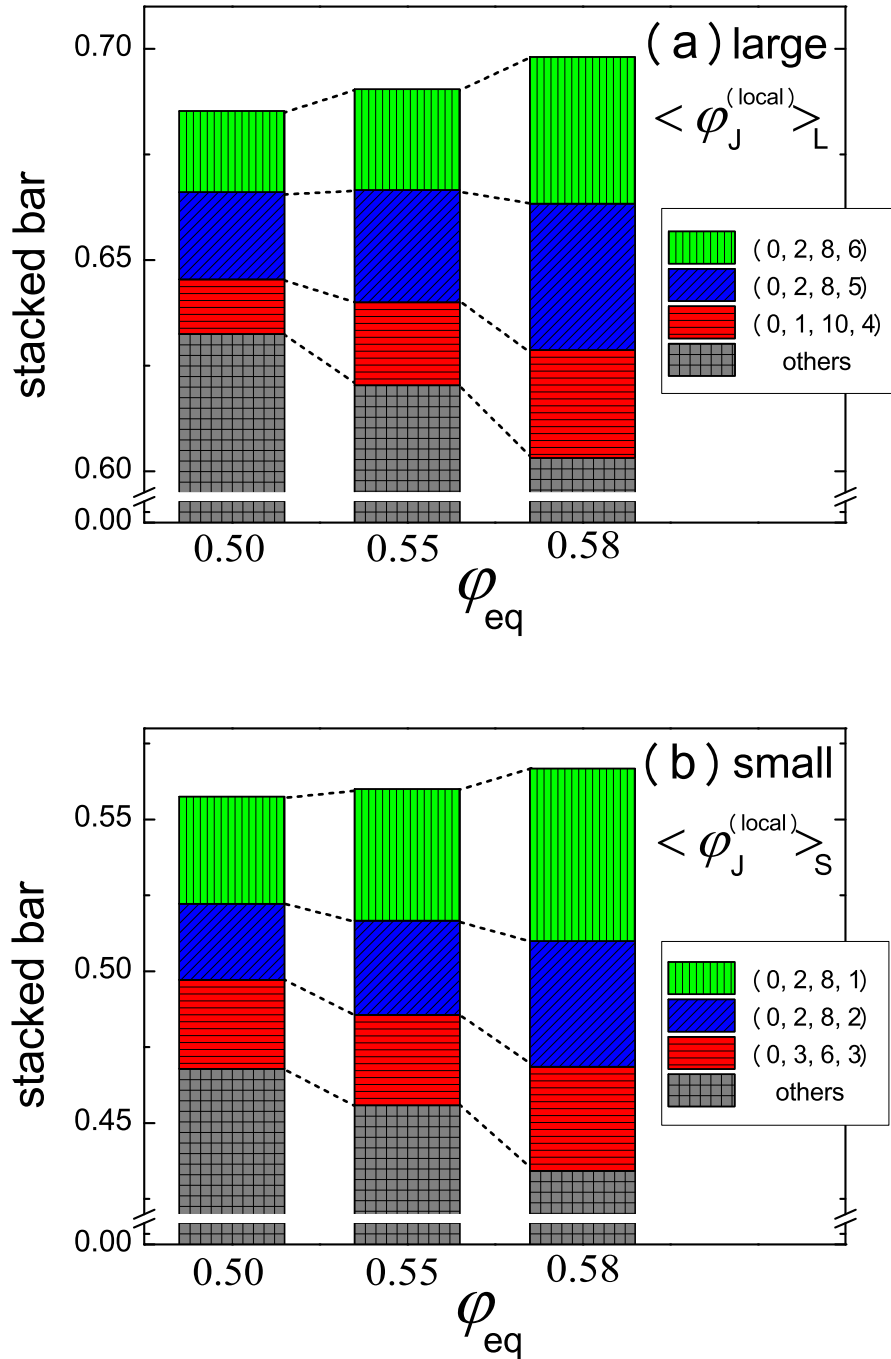


Figure 4.15: (a), (b) The stacked bars of  $\langle \varphi_J^{(local)} \rangle_L$  (a) and  $\langle \varphi_J^{(local)} \rangle_S$  (b). The heights of the stacked bars correspond to  $\langle \varphi_J^{(local)} \rangle_\alpha$  ( $\alpha = L, S$ ). The portions of the stacked bar are  $S_{\alpha,l}$  ( $l = 1, 2, 3$ ) and  $S_{\alpha,others}$ . The signatures of the top three Voronoi polyhedra are colored.



## Chapter 5

# Summary and Future Works

In this Chapter, we summarize our results and discuss perspectives for future works.

The study of the glass transition has more than a half-century of history. Despite of intensive studies up to now, the nature of the glass transition is still uncovered. Due to the recent development of the electronic technology and computer, the computer simulation has become a standard tool and infused us with a lot of insights about the glass transition. It enable us to access to the microscopic information which has never been possible by the experiments.

One of the characteristic properties of the glassy systems is the slowing down of the dynamics with decreasing the temperature or increasing the pressure. The relaxation time and the viscosity grow dramatically within narrow temperature or pressure windows. Interestingly, whereas the dynamic properties change qualitatively, the static properties hardly change. The dramatic slowing down of the dynamics without resorting any apparent changes of the static properties is a conundrum and an essential difference from the critical slowing down at the second order phase transition point. Besides, the temperature dependence of the relaxation time and the viscosity is also unusual. The dynamics of some glass formers show the apparent deviation from the simple Arrhenius law, and they are called the fragile glass formers. The glass formers whose dynamics show the Arrhenius law are classified as the strong glass formers. Although the deviation from the Arrhenius law, or the super-Arrhenius behavior, for the fragile glass formers is a distinct property of the glassy systems, microscopic understanding of this behavior is still lacking. The classification of the strong and fragile glass formers is a very basic concept and we always see this topics in the first pages of virtually all books and review papers of the glass transition. Designing a computer simulation model whose fragility can be tuned systematically is the first step to tackle this fundamental issue. We have constructed such a model showing a variety of the fragility. To be specific, we systematically tune the attractive potential energy between different species of the binary system to change the local structure of the system from the tetrahedral network to the isotropic structures. We found that the fragility of the system varies from the value of a typical strong glass former model to the one of a fragile binary soft-sphere potential model. An advantage of our model compared with previous models is its simplicity. Previous models adopted relatively complicated way to control the fragility, for example, introducing an internal degree of freedom such as the spin in a particle or tuning the three body interaction potentials. Contrarily, our new model use only simple two body interaction potential. It would help us to understand essence of the fragility and compare the simulation results with theoretical predictions. Our model shows the correlation between the microscopic configurations of the particles and the fragility of the system. We found that when the system is tuned to have the network structure, it have small fragility, and when the system is tuned to have more isotropic and compact structure, the fragility becomes larger. Moreover, we confirmed that more fragile system shows more pronounced dynamical heterogeneity through the decoupling between the self diffusion and the relaxation time, and the dynamics becomes more non-Gaussian. In future, we shall inspect the model further to investigate the super-Arrhenius behavior. It is empirically known that there are correlations between the fragility of the system and other properties such as mechanical constants, vibrational properties [64], and the exponent of the stretched exponential relaxation [13]. We are planning to verify these experimental facts by using our model and understand microscopic

origin of the relations in the future.

More fundamental argument in the study of the glass transition is whether a thermodynamic singular point, the ideal glass transition point, at which dynamics truly freezes exists or not. The excess entropy, or the configurational entropy, measured by the experiments implies that there exists such a point at which the configurational entropy vanishes at very low temperatures where usual experiments and simulations are inaccessible. Besides, fitting of the relaxation time and viscosity by the VFT equation suggests a singular point at the same temperature. Thus, both the thermodynamic and dynamic data support the existence of the ideal glass transition. The RFOT, a promising candidate for the ultimate theory of the glass transition, has been established based on the above facts that the ideal glass transition exists and the singularity causes the slow dynamics of the system. However, identifying the ideal glass transition is a hard problem because it needs an astronomical time scale to approach the point by experiments and simulations. So far, all studies related to the ideal glass transition resort on unreliable extrapolations and fittings. Therefore, the existence of the ideal glass transition was still unclear. Recently, a novel idea to bypass this difficulty has been proposed [69]. By randomly pinning a fraction of the particles, it has been predicted the ideal glass transition temperature rises to a point at which experiments and simulations in an equilibrium state are accessible. We used this method for a three dimensional simulation system and computed the zero configurational entropy states and thus identified the ideal glass transition points for the first time. We drew the equilibrium phase diagram of the fluids and the ideal glass states in the parameter space of two parameters, the temperature and the fraction of the pinned particles. In addition, we determined the spinodal line by analyzing the potential energy landscape. We found that the spinodal line and the fluid-glass line cross at a finite temperature and a fraction of the pinned particles, which implies that there exists a certain critical point similar to the critical point of the gas-liquid phase diagram. Careful studies are needed to identify the precise location and the nature, or universality class, of the critical point in future works. Our results presented in this thesis qualitatively agrees with the theoretical prediction of the RFOT. The next natural step is to detect the static length scale predicted by the RFOT which governs the slow dynamics. Recently, an idea to probe such a static length from the mechanical response has been proposed [97,98]. We are planning to apply this method for the randomly pinned configurations to detect the static length down to the ideal glass transition point.

The relation between the glass and jamming transitions is another fundamental issue in the field. It had been known that the hard-sphere particles like pinballs solidify with random configurations at the volume fraction  $\varphi_J \simeq 0.64$ .  $\varphi_J$  is called the jamming transition point and had been thought that it is uniquely determined like the critical point of the usual phase transitions. Therefore, some insist that the jamming transition is merely the zero temperature glass transition. Recent numerical simulation results show that the jamming transition point systematically varies depending on the generating protocols such as the compression rate. If we compress the spheres slowly, or equilibrate the system at high density,  $\varphi_J$  increases above 0.64. The RFOT predicts  $\varphi_J$  is the inherent structures (local minima of the landscape) of the hard-spheres systems and accounts for the protocol dependence of  $\varphi_J$ . In this thesis, we verified the prediction of the RFOT via the simulation of the jamming transition and with the numerical analysis of the MCT. The results were consistent with the prediction of the theory. However, another question is raised. How does the jammed system denser than 0.64 look like? Intuitively, the increasing of the density means the growth of the crystalline structures. But, we could not find out a sign of the emergence of any crystalline orders. Here, we consider mechanism of these high density jammed states via the configurational entropy. As our study of the random pinning has shown, the configurational entropy can decrease and become zero even with random configurations. The decreasing of the configurational entropy means the decrease of the number of available states. When the configurational entropy is zero, the corresponding state is almost uniquely determined despite of the random configuration. This implies that there exists seemingly random, but highly optimized configuration. In the RFOT, this configuration is called the amorphous order. Does the amorphous order grow in our highly packed jammed states? And is it possible to detect such order from the random configurations? These questions should be answered in future works.

# Appendix A

## The Adam Gibbs Theory

In this appendix, we summarize the Adam Gibbs theory (AGT) [2, 58]. The AGT explains the slow dynamics of the supercooled liquids from the thermodynamic point of view. The theory assumes that the ideal glass transition point  $T_K$  exists and its singularity causes the slowing down of the dynamics. A thermodynamic function, called the configurational entropy  $S_c$  plays a central role in the AGT. The theory connects  $S_c$  and the dynamical observables such as the relaxation time  $\tau_\alpha$  and the viscosity  $\eta$  in the supercooled state. The random first order transition theory (RFOT) have been developed based on the AGT [17, 66]. Thus, basic concepts of the AGT are inherited to the RFOT.

### A.1 Dynamics and configurational entropy

First, we consider an activation process of the glass formers. The temperature dependence of  $\tau_\alpha$  and  $\eta$  can be represented by

$$\tau_\alpha(T), \eta(T) \propto \exp\left[\frac{E(T)}{k_B T}\right], \quad (\text{A.1.1})$$

where  $E(T)$  is the temperature dependent activation energy. When the temperature is lowered,  $E(T)$  increases due to the increase of the number of particles participating the elementally relaxation process. To be specific, at low temperatures, the particles affect each other so tightly that they can not relax independently. Therefore, they relax by forming a cluster. This collectively moving cluster is called the cooperative rearrange region (CRR). We denote the number of particles composing a single CRR as  $n(T)$ .  $n(T)$  increases with decreasing  $T$  later. We consider the number of available states inside a CRR,  $\Omega$ . The AGT assumes that  $\Omega$  is insensitive to the temperature, *i.e.*,  $\Omega$  is constant. Next, we consider the number of states for the entire system  $\mathcal{N}(T)$ .  $\mathcal{N}(T)$  can be expressed approximately by  $n(T)$  and the number of particles in the system  $N$ . The number of CRRs is given by  $N/n(T)$ . If these CRRs move independently,  $\mathcal{N}(T)$  is approximately written as

$$\mathcal{N}(T) \simeq \Omega^{N/n(T)}. \quad (\text{A.1.2})$$

The definition of  $S_c$  is the logarithmic function of the number of available states,  $S_c(T) = \log \mathcal{N}(T)$ . Hereafter, we use the intensive value  $s_c = S_c/N$  instead of the extensive one. Therefore,  $s_c$  is expressed by

$$s_c(T) \simeq \frac{\log \Omega}{n(T)}. \quad (\text{A.1.3})$$

Eq. (A.1.3) is crucial since it connects the growth of the CRR with the decreasing of the configurational entropy.  $n(T)$  diverges when  $s_c(T)$  becomes zero, which means that at  $T_K$ , the entire system is consist of a single CRR. Finally, we connect temperature dependence of  $\tau_\alpha$  or  $\eta$  and  $s_c$ . As we discussed before, the increase of  $E(T)$  can be regard as the growth of the CRR. Here we postulate that  $E(T)$  is proportional to  $n(T)$ . Actually, this relation is confirmed by an experiment recently [16]. Then  $\tau_\alpha$  or  $\eta$  can be expressed as

$$\tau_\alpha(T), \eta(T) \propto \exp\left[\frac{An(T)}{k_B T}\right] \simeq \exp\left[\frac{B}{T s_c(T)}\right], \quad (\text{A.1.4})$$

where  $A$  and  $B$  are constants. Eq. (A.1.4) explicitly connects the dynamical observables ( $\tau_\alpha$  and  $\eta$ ) with the thermodynamic quantity,  $s_c$ . If  $s_c$  decreases and eventually vanishes at  $T_K$ ,  $\tau_\alpha$  and  $\eta$  diverge.

## A.2 Relation with the VFT equation

A fitting function, the Vogel-Fulcher-Tamman (VFT) equation,  $\tau_\alpha(T), \eta(T) \propto \exp[1/K(T/T_0 - 1)]$  can be derived from the AGT. Here we explain the derivation of the VFT equation.  $s_c$  is expanded near (putative)  $T_K$  as

$$\begin{aligned} s_c(T) &\simeq s_c(T_K) + \frac{\partial s_c(T_K)}{\partial T}(T - T_K) \\ &= \Delta c_p(T_K) \left( \frac{T - T_K}{T_K} \right), \end{aligned} \tag{A.2.1}$$

where  $\Delta c_p(T)$  is the jump of the (isobaric) specific heat between the supercooled and the crystal states. We use  $s_c(T_K) = 0$  at the second equality in Eq. (A.2.1). If we substitute Eq. (A.2.1) to Eq. (A.1.4), we arrive at

$$\begin{aligned} \tau_\alpha(T), \eta(T) &\propto \exp \left[ \frac{BT_K}{T\Delta c_p(T - T_K)} \right] \\ &\simeq \exp \left[ \frac{B}{\Delta c_p(T - T_K)} \right]. \end{aligned} \tag{A.2.2}$$

Therefore, the VFT equation is derived, and this shows  $T_0$  is found to be identical to  $T_K$ ,  $T_K = T_0$ . Besides, the fragility parameter  $K$  is related to  $\Delta c_p$  as  $K \propto \Delta c_p(T_K)$ . This result is consistent with the experimental fact that the fragile glass formers tend to have large jump of the specific heat at the empirical glass transition temperature  $T_g$ .

# Appendix B

## The Mode-Coupling Theory

In this appendix, we briefly explain the mode-coupling theory (MCT) and describe numerical methods to obtain the MCT transition point for the hard sphere systems discussed in Chap. 4.

### B.1 The MCT equation

In the history of the glass transition research, quite a few theories have been proposed. Among them, the MCT is the first principle theory which partially but successfully explain dynamical behaviors of the glass formers from a purely microscopic point of view [74]. The MCT is a kind of approximate theory of generalized Langevin equation for the density correlation function  $F(k, t)$ . For simplicity, we consider the monodisperse system first, then we discuss the binary system in the next section. The generalized Langevin equation is given by

$$\dot{F}(k, t) + \frac{D_0 k^2}{S(k)} \left\{ F(k, t) + \int_0^t dt' m(k, t-t') \dot{F}(k, t') \right\} = 0, \quad (\text{B.1.1})$$

where  $D_0$  is the diffusion constant at high temperature or low density,  $S(k)$  is the static structure factor  $S(k) = F(k, t=0)$ .  $m(k, t)$  is referred to as the memory kernel and information of glassy dynamics are contained in this kernel function. According to the MCT,  $m(k, t)$  is given by

$$m(k, t) = \frac{S(k)}{2\rho k^2} \int \frac{d\mathbf{q}}{(2\pi^3)} \nu_k^2(\mathbf{q}, \mathbf{k}-\mathbf{q}) F(|\mathbf{k}-\mathbf{q}|, t) F(\mathbf{q}, t), \quad (\text{B.1.2})$$

where  $\nu_k(\mathbf{p}, \mathbf{q})$  is the vertex function expressed as

$$\nu_k(\mathbf{p}, \mathbf{q}) = \rho \left[ c(p) \hat{\mathbf{k}} \cdot \mathbf{p} + c(q) \hat{\mathbf{k}} \cdot \mathbf{q} \right], \quad (\text{B.1.3})$$

where  $c(k)$  is the direct correlation function which is related by  $S(k)$  through the Ornstein-Zernike relation [4] defined by

$$c(k) = \frac{1 - 1/S(k)}{\rho}. \quad (\text{B.1.4})$$

The MCT enables one to calculate  $F(k, t)$  using the number density  $\rho$  and  $S(k)$  as inputs and reproduces the experimental and simulational results quantitatively. Remarkably, the MCT describes the two-step relaxation of  $F(k, t)$  which is a finger print of the glassy dynamics as mentioned in Chap. 1.

However, the MCT has an obvious drawback at low temperature or high density regions. The MCT predicts a certain threshold point  $T_d$  or  $\varphi_d$  beyond which  $F(k, t)$  never reaches zero value. Therefore, one may think that the MCT correctly captures the glass transition and  $T_d$  is identical to  $T_K$ . Unfortunately,  $T_d$  ( $\varphi_d$ ) is much higher (lower) than experimentally observed glass transition point  $T_g$  ( $\varphi_g$ ) and  $T_K$  ( $\varphi_K$ ). It is established now that  $T_d$  and  $\varphi_d$  are spurious transition points. Instead, they are crossover points at which dynamics qualitatively change. In the RFOT picture,  $T_d$  and  $\varphi_d$  are interpreted as the points at which exponentially large number of metastable states appear in the free energy landscape. One of the main goal of Chap. 4 is to verify a consequence of this prediction by using the computer simulation and the numerical analysis of the MCT equation.

## B.2 The MCT transition points for the binary hard-sphere systems

We numerically analyze the MCT for binary hard spheres (3D) and disks (2D) to determine the MCT transition point  $\varphi_d^{(\text{theory})}$ . The MCT for the binary mixture is obtained as a straightforward extension from that of the monodisperse system given by Eq. (B.1.1) - (B.1.4) [74]. The MCT provides the time evolution of the density correlation between each species.

$$F_{\alpha\beta}(\mathbf{k}, t) = \langle \delta\rho_\alpha(\mathbf{k}, t) \delta\rho_\beta^*(\mathbf{k}, 0) \rangle, \quad (\text{B.2.1})$$

where the Greek indices  $\alpha, \beta \in \{L, S\}$  stand for species of particle,  $\delta\rho_\alpha(\mathbf{k}, t)$  is the density fluctuation of species  $\alpha$  with wavevector  $\mathbf{k}$  and time  $t$ .  $\langle \dots \rangle$  is the ensemble average. In the time domain, dynamic equation of the MCT for the overdamped colloidal system reads, by adopting dyadic abbreviation, as

$$\tau_k \dot{\mathbf{F}}(k, t) + \mathbf{S}^{-1}(k) \mathbf{F}(k, t) + \int_0^t dt' \mathbf{M}(k, t-t') \dot{\mathbf{F}}(k, t') = 0, \quad (\text{B.2.2})$$

where  $\tau_k$  and  $\mathbf{S}(k) = \mathbf{F}(k, 0)$  represent the short time relaxation time matrix and the static structure factor matrix. These quantities are used as inputs to the MCT.  $\mathbf{M}(k, t)$  is the memory function represents nonlinear feedback of the density fluctuation in dense liquids and given by

$$M_{\alpha\beta}(k, t) = \frac{1}{2x_\alpha x_\beta \rho k^2} \sum_{\alpha'\alpha''\beta'\beta''} \int \frac{d^d \mathbf{q}}{(2\pi)^d} V_{\alpha\alpha'\alpha''}^{\mathbf{k};\mathbf{q}\mathbf{p}} F_{\alpha'\beta'}(q, t) F_{\alpha''\beta''}(p, t) V_{\beta'\beta''}^{\mathbf{k};\mathbf{q}\mathbf{p}}, \quad (\text{B.2.3})$$

where  $x_\alpha$  is the mole fraction of species  $\alpha$  and  $\mathbf{p} = \mathbf{k} - \mathbf{q}$ . We introduced the vertex function  $V_{\alpha\alpha'\alpha''}^{\mathbf{k};\mathbf{q}\mathbf{p}}$  as

$$V_{\alpha\alpha'\alpha''}^{\mathbf{k};\mathbf{q}\mathbf{p}} = \frac{1}{k} \mathbf{k} \cdot \mathbf{q} \rho c_{\alpha\alpha'}(q) \delta_{\alpha\alpha''} + \frac{1}{k} \mathbf{k} \cdot \mathbf{p} \rho c_{\alpha\alpha''}(p) \delta_{\alpha\alpha'}, \quad (\text{B.2.4})$$

where  $\mathbf{c}(k)$  is the direct correlation function matrix and related to the static structure factor matrix with Ornstein-Zernicke equation [4],

$$\rho c_{\alpha\beta}(k) = \frac{\delta_{\alpha\beta}}{x_\alpha} - [\mathbf{S}^{-1}]_{\alpha\beta}(k). \quad (\text{B.2.5})$$

The dynamic transition point  $\varphi_d^{(\text{theory})}$  is defined as a threshold volume fraction at which  $\mathbf{F}(k, t)$  becomes no longer ergodic.

In order to evaluate  $\varphi_d^{(\text{theory})}$ , we solve Eq. (B.2.2) at long time limit  $t \rightarrow \infty$ .  $\varphi_d^{(\text{theory})}$  can be identified as the point at which the long time limit of  $\mathbf{F}(k, t)$ , so-called the Debye-Waller (DW) factor  $\mathbf{D}(k) = \lim_{t \rightarrow \infty} \mathbf{F}(k, t)$  becomes nonzero.  $\mathbf{D}(k)$  can be evaluated from the long time limit of Eq. (B.2.2);

$$\mathbf{D}(k) = [\mathbf{S}^{-1}(k) + \mathbf{M}(k)]^{-1} \mathbf{M}(k) \mathbf{S}^{-1}(k), \quad (\text{B.2.6})$$

where  $\mathbf{M}(k)$  is long time limit of memory function matrix  $\mathbf{M}(k, t)$ . Eq. (B.2.6) is a self-consistent equation for the DW factor which can be solved numerically. Note that  $\tau_k$  is absent in Eq. (B.2.6) since first term in left hand side of Eq. (B.2.2) vanishes in long time limit. Thus input to the MCT to obtain  $\varphi_d^{(\text{theory})}$  is the static structure factor matrix only.

We evaluate the static structure factor matrix  $\mathbf{S}(k)$  by using the coordinate data generated by the MC simulation. We choose the number of particles in the simulation up to  $N = 2048$  in 2D and  $N = 8192$  in 3D. We have checked that the finite size effects on the value of the MCT transition point is negligible in these system sizes. Since the size of the system is finite we can not obtain meaningful value of the static structure factors in  $k < k_{\text{IR}}$ , where  $k_{\text{IR}}$  is infrared cutoff wavenumber given by  $k_{\text{IR}} = 4\pi/L$ , where  $L$  is the linear length of the simulation box. Thus we employ the static structure factors evaluated by the Percus-Yevik (PY) approximation [4] for  $k < k_{\text{IR}}$ . As shown in Fig. B.1, the PY approximation is sufficiently accurate in long wavelength and in the volume fractions we are interested in, while it slightly overestimates the height of the first peak of the static structure factors.

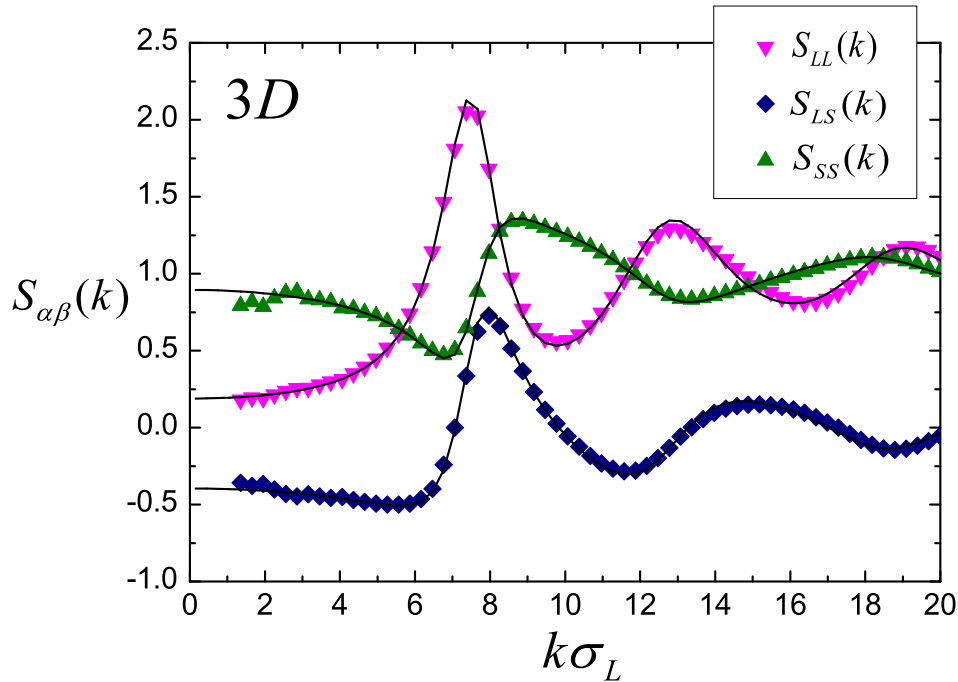


Figure B.1: The static structure factors  $S_{\alpha\beta}(k)$  for  $\varphi = 0.526$ ,  $R = 1.4$ ,  $x_S = 0.5$ ,  $N = 2048$  in 3D. The filled points are the data from the MC simulation and the solid lines are the Percus-Yevick approximation solutions.

In order to solve the self-consistent equation, Eq. (B.2.6), we discretized Eq. (B.2.6) on 250 grid points between  $k \in [0.15, 75.0]$  in 3D and  $k \in [0.10, 75.0]$  in 2D.

These values of discretization parameters are chosen to be identical to those used in previous studies on the binary MCT [136, 137]. The value of the MCT transition points  $\varphi_d^{(\text{theory})}$  for  $R = 1.4$ ,  $x_S = 0.5$  are obtained as  $\varphi_d^{(\text{theory})} = 0.6925 \pm 0.0005$  in 2D and  $\varphi_d^{(\text{theory})} = 0.5255 \pm 0.0005$  in 3D. We confirm that these values do not depend on computation methods of  $S_{\alpha\beta}(k)$ , *i.e.*, the Fourier transform of the radial distribution functions and a direct calculation in the wave vector space. Note that the value of the MCT transition point in 2D is consistent with that obtained in Ref. [136] but slightly smaller than the value obtained in Ref. [137] for 3D,  $\varphi_d^{(\text{theory})} \cong 0.55$ .



## Appendix C

# Configurational entropy of the pinned systems

In this Appendix, we describe the method how to compute the configurational entropy of the pinned systems by the numerical simulations. Basically, we follow the inherent structure (IS) formalism, but this has been established mainly for bulk systems [21, 83, 84]. Therefore, we develop the IS formalism for the pinned systems.

### C.1 Statistical mechanics of the pinned systems

First, we consider the bulk (unpinned) case to introduce the notation. We use a binary Lennard-Jones mixture as a model. The number of particles is  $N = N_A + N_B$ , where  $N_A$  and  $N_B$  are the number of particles for species A and B respectively. For simplicity, we consider same mass for A and B particles ( $m = m_A = m_B$ ). The positions of  $N$  particles are expressed by  $\{\mathbf{x}\} = (\mathbf{x}_1, \mathbf{x}_2, \dots, \mathbf{x}_N)$ . The Hamiltonian of the system is

$$H = \sum_i^N \frac{\mathbf{p}_i^2}{2m} + U(\{\mathbf{x}\}), \quad (\text{C.1.1})$$

where  $\mathbf{p}_i$  is the momentum of  $i$ -th particle and  $U$  is the potential energy of the system. The partition function of the system for the canonical ensemble is given by

$$Z(T) = \frac{1}{\Lambda^{3N} N_A! N_B!} \int d\{\mathbf{x}\} \exp[-\beta U(\{\mathbf{x}\})], \quad (\text{C.1.2})$$

where  $\Lambda = \sqrt{2\pi\beta\hbar^2/m}$  is the de Broglie thermal wavelength and  $\beta$  is the inverse temperature. The Helmholtz free energy of the system is  $F(T) = -T \log Z(T)$  and the probability distribution function of the particles is

$$P(\{\mathbf{x}\} : T) = \frac{1}{Z(T) \Lambda^{3N} N_A! N_B!} \exp[-\beta U(\{\mathbf{x}\})]. \quad (\text{C.1.3})$$

Next, we consider the pinning case. We pick up  $cN$  particles from an equilibrium configuration via the procedure which we discussed in Sec. 3.2. The number of mobile (unpinned) particles is  $M = (1 - c)N = M_A + M_B$ , where  $M_A$  and  $M_B$  are the number of mobile particles for A and B. We denote the positions of mobile and pinned particles are  $\{\mathbf{r}\}$  and  $\{\mathbf{s}\}$ , respectively. Then, we can decompose  $U(\{\mathbf{x}\})$  as  $U(\{\mathbf{x}\}) = U(\{\mathbf{s}\}, \{\mathbf{r}\}) = U_{\text{pin}}(\{\mathbf{s}\}) + U_{\text{move}}(\{\mathbf{r}\}) + U_{\text{int}}(\{\mathbf{s}\}, \{\mathbf{r}\})$ , where  $U_{\text{pin}}(\{\mathbf{s}\})$ ,  $U_{\text{move}}(\{\mathbf{r}\})$ , and  $U_{\text{int}}(\{\mathbf{s}\}, \{\mathbf{r}\})$  are the sum of the interaction potentials between pinned particle - pinned particle, mobile particle - mobile particle, and mobile particle - pinned particle, respectively. The probability distribution of the pinned particles is expressed by tracing out  $\{\mathbf{r}\}$  from Eq. (C.1.3).

$$P_{\text{pin}}(\{\mathbf{s}\} : T) = \frac{1}{Z(T) \Lambda^{3N} N_A! N_B!} \int d\{\mathbf{r}\} \exp[-\beta U(\{\mathbf{s}\}, \{\mathbf{r}\})]. \quad (\text{C.1.4})$$

Then, we consider the thermodynamics of the mobile particles under a particular realization  $\{\mathbf{s}\}$ . The Hamiltonian of the mobile particles in this situation is

$$\tilde{H} = \sum_i^M \frac{\mathbf{p}_i^2}{2m} + U(\{\mathbf{s}\}, \{\mathbf{r}\}). \quad (\text{C.1.5})$$

The partition function of the system is given by

$$\tilde{Z}(\{\mathbf{s}\} : T) = \frac{1}{\Lambda^{3M} M_A! M_B!} \int d\{\mathbf{r}\} \exp[-\beta U(\{\mathbf{s}\}, \{\mathbf{r}\})] \quad (\text{C.1.6})$$

and the Helmholtz free energy of the system is  $\tilde{F}(\{\mathbf{s}\} : T) = -T \log \tilde{Z}(\{\mathbf{s}\} : T)$ . We can obtain the following relation between  $P_{\text{pin}}(\{\mathbf{s}\} : T)$  and  $\tilde{Z}(\{\mathbf{s}\} : T)$  immediately.

$$P_{\text{pin}}(\{\mathbf{s}\} : T) = \frac{\tilde{Z}(\{\mathbf{s}\} : T) \Lambda^{3M} M_A! M_B!}{Z(T) \Lambda^{3N} N_A! N_B!}. \quad (\text{C.1.7})$$

The probability distribution function of  $\{\mathbf{r}\}$  under a realization  $\{\mathbf{s}\}$  is expressed by the conditional probability distribution,

$$\tilde{P}(\{\mathbf{r}\} | \{\mathbf{s}\} : T) = \frac{1}{\tilde{Z}(\{\mathbf{s}\} : T) \Lambda^{3M} M_A! M_B!} \exp[-\beta U(\{\mathbf{s}\}, \{\mathbf{r}\})]. \quad (\text{C.1.8})$$

In these settings, one can calculate any static observables  $A(\{\mathbf{s}\}, \{\mathbf{r}\})$ . To this end, we define two different types of average. One is the thermal average,  $\langle \dots \rangle_{\{\mathbf{s}\}}$ , for the mobile particles under a realization  $\{\mathbf{s}\}$ ,

$$\langle \dots \rangle_{\{\mathbf{s}\}} = \int d\{\mathbf{r}\} \tilde{P}(\{\mathbf{r}\} | \{\mathbf{s}\} : T) (\dots). \quad (\text{C.1.9})$$

The other is quenched average,  $\overline{\dots}$ , for the pinned particles,

$$\overline{\dots} = \int d\{\mathbf{s}\} P_{\text{pin}}(\{\mathbf{s}\} : T) (\dots). \quad (\text{C.1.10})$$

If we take both averages at the same time, we get simple expression,

$$\begin{aligned} \overline{\langle A \rangle_{\{\mathbf{s}\}}} &= \int d\{\mathbf{s}\} P_{\text{pin}}(\{\mathbf{s}\} : T) \int d\{\mathbf{r}\} \tilde{P}(\{\mathbf{r}\} | \{\mathbf{s}\} : T) A(\{\mathbf{s}\}, \{\mathbf{r}\}) \\ &= \int d\{\mathbf{x}\} P(\{\mathbf{x}\} : T) A(\{\mathbf{x}\}) = \langle A \rangle_{\text{bulk}}. \end{aligned} \quad (\text{C.1.11})$$

We used Eq. (C.1.7) for the last equality. This means that double average of any static quantities is equal to the bulk one. Note that this is a special property of the pinning procedure which we consider now, *i.e.*, pinned particles are selected randomly from a equilibrium configuration.

Finally, the Helmholtz free energy of the pinned system is given by

$$F(c, T) = \int d\{\mathbf{s}\} P_{\text{pin}}(\{\mathbf{s}\} : T) \tilde{F}(\{\mathbf{s}\} : T). \quad (\text{C.1.12})$$

In general, the free energy of the pinned system is different from the bulk free energy since the quenched average is performed after taking the logarithm.

## C.2 Total entropy of the pinned systems

In this thesis, we calculate the total entropy  $S$  of the pinned systems by using the thermodynamic integration (TI) method from high temperature limit  $\beta = 0$  to the target temperature  $\beta = \beta^*$ . First,

we consider thermodynamics under a particular realization  $\{\mathbf{s}\}$ . The total entropy of a realization  $\{\mathbf{s}\}$  is expressed as

$$\tilde{S}(\{\mathbf{s}\} : \beta^*) = \tilde{S}(\{\mathbf{s}\} : \beta = 0) + \int_0^{\beta^*} d\beta \frac{\partial \tilde{S}}{\partial \beta}, \quad (\text{C.2.1})$$

The first term of the RHS of Eq. (C.2.1) is written by

$$\tilde{S}(\{\mathbf{s}\} : \beta = 0) = (\beta \langle \tilde{H} \rangle_{\{\mathbf{s}\}})_{\beta=0} - (\beta \tilde{F})_{\beta=0}. \quad (\text{C.2.2})$$

We do not calculate  $(\beta \langle \tilde{H} \rangle_{\{\mathbf{s}\}})_{\beta=0}$  further since it cancels out with another term later. The second term,  $(\beta \tilde{F})_{\beta=0}$ , is calculated straightforwardly,

$$\begin{aligned} (\beta \tilde{F})_{\beta=0} &= -\log \frac{1}{\Lambda^{3M} M_A! M_B!} \int d\{\mathbf{r}\} e^0 = -\log \frac{V^M}{\Lambda^{3M} M_A! M_B!} \\ &= M \left\{ \log \left( \frac{M}{V} \right) - 1 \right\} + M_A \log \left( \frac{M_A}{M} \right) + M_B \log \left( \frac{M_B}{M} \right) + 3M (\log \Lambda)_{\beta=0}, \end{aligned} \quad (\text{C.2.3})$$

where  $V = \int d\mathbf{r}$ . We carefully treat the last term of Eq. (C.2.3) later, since  $(\log \Lambda)_{\beta=0}$  diverges when  $\beta \rightarrow 0$ .

Next, we calculate the second term of the RHS of Eq. (C.2.1),

$$\begin{aligned} \int_0^{\beta^*} d\beta \frac{\partial \tilde{S}}{\partial \beta} &= \int_0^{\beta^*} d\beta \beta \frac{\partial \langle \tilde{H} \rangle_{\{\mathbf{s}\}}}{\partial \beta} \\ &= (\beta \langle \tilde{H} \rangle_{\{\mathbf{s}\}})_{\beta=\beta^*} - (\beta \langle \tilde{H} \rangle_{\{\mathbf{s}\}})_{\beta=0} - \int_0^{\beta^*} d\beta \langle \tilde{H} \rangle_{\{\mathbf{s}\}}. \end{aligned} \quad (\text{C.2.4})$$

We use a thermodynamic relation for the first equality. Then, we put Eq. (C.2.2), (C.2.3), and (C.2.4) into Eq. (C.2.1).

$$\begin{aligned} \tilde{S}(\{\mathbf{s}\} : \beta^*) &= M \left\{ 1 - \log \left( \frac{M}{V} \right) \right\} - M_A \log \left( \frac{M_A}{M} \right) - M_B \log \left( \frac{M_B}{M} \right) - 3M (\log \Lambda)_{\beta=0} \\ &\quad + (\beta \langle \tilde{H} \rangle_{\{\mathbf{s}\}})_{\beta=\beta^*} - \int_0^{\beta^*} d\beta \langle \tilde{H} \rangle_{\{\mathbf{s}\}}. \end{aligned} \quad (\text{C.2.5})$$

The thermal average of the Hamiltonian under a realization  $\{\mathbf{s}\}$  is

$$\langle \tilde{H} \rangle_{\{\mathbf{s}\}} = \frac{3M}{2\beta} + U_{\text{pin}} + \langle U_{\text{move}} \rangle_{\{\mathbf{s}\}} + \langle U_{\text{int}} \rangle_{\{\mathbf{s}\}}. \quad (\text{C.2.6})$$

Then, we substitute this into the last two Hamiltonian terms of Eq. (C.2.5). Then,  $\tilde{S}(\{\mathbf{s}\} : \beta^*)$  is expressed by

$$\begin{aligned} \tilde{S}(\{\mathbf{s}\} : \beta^*) &= M \left\{ 1 - \log \left( \frac{M}{V} \right) \right\} - M_A \log \left( \frac{M_A}{M} \right) - M_B \log \left( \frac{M_B}{M} \right) - 3M (\log \Lambda)_{\beta=\beta^*} + \frac{3M}{2} \\ &\quad + (\beta \langle U_{\text{move}} \rangle_{\{\mathbf{s}\}} + \beta \langle U_{\text{int}} \rangle_{\{\mathbf{s}\}})_{\beta=\beta^*} - \int_0^{\beta^*} d\beta (\langle U_{\text{move}} \rangle_{\{\mathbf{s}\}} + \langle U_{\text{int}} \rangle_{\{\mathbf{s}\}}). \end{aligned} \quad (\text{C.2.7})$$

This expression is suitable for the numerical simulation since we only need a temperature dependence of  $\langle U_{\text{move}} \rangle_{\{\mathbf{s}\}} + \langle U_{\text{int}} \rangle_{\{\mathbf{s}\}}$ . Practically, we calculate  $\langle U_{\text{move}} \rangle_{\{\mathbf{s}\}}$  and  $\langle U_{\text{int}} \rangle_{\{\mathbf{s}\}}$  at many temperatures along  $\beta = 0$  ( $T = \infty$ ) and  $\beta^*$  ( $T^*$ ). But we should be careful about the following. The pinning realizations  $\{\mathbf{s}\}$  is made from an equilibrium bulk configuration at  $\beta = \beta^*$ . While decreasing  $\beta$  (increasing  $T$ ),  $\{\mathbf{s}\}$  does not change and have to be fixed permanently from the outset.

Next let us consider how to deal with the integration in Eq. (C.2.7). We have to care about the integration part because the high temperature limit ( $\beta \rightarrow 0$ ) might cause divergence. Here we limit

ourselves to the case of the Lennard-Jones pair interaction potential,  $v(r) = \epsilon/4\{(\sigma/r)^{12} - (\sigma/r)^6\}$ . In this case, the average of the potential energy at high temperature is expanded in terms of  $\beta$  as

$$\langle U_{\text{move}} \rangle_{\{\mathbf{s}\}} + \langle U_{\text{int}} \rangle_{\{\mathbf{s}\}} = A\beta^{-3/4} + B\beta^{-1/2} + C\beta^{-1/4} + \mathcal{O}(1). \quad (\text{C.2.8})$$

where  $A$ ,  $B$ , and  $C$  are constants [84]. Fortunately, Eq. (C.2.8) tells us that the integration in Eq. (C.2.7) does not diverge due to  $\beta^{-3/4}$  dependence, and thus Eq. (C.2.8) can be useful function to extrapolate very high temperature region of  $\langle U_{\text{move}} \rangle_{\{\mathbf{s}\}} + \langle U_{\text{int}} \rangle_{\{\mathbf{s}\}}$ . We show  $\beta^{3/4}(\langle U_{\text{move}} \rangle_{\{\mathbf{s}\}} + \langle U_{\text{int}} \rangle_{\{\mathbf{s}\}})/M$  as a function of  $\beta^{1/4}$  in Fig C.1. The red fitting curves obtained by  $\beta^{3/4}(\langle U_{\text{move}} \rangle_{\{\mathbf{s}\}} + \langle U_{\text{int}} \rangle_{\{\mathbf{s}\}}) = A + B(\beta^{1/4}) + C(\beta^{1/4})^2 + \mathcal{O}((\beta^{1/4})^3)$  are also plotted in the figure to demonstrate the validity of Eq. (C.2.8). It is clear that Eq. (C.2.8) holds very well even in the presence of the pinned particles.

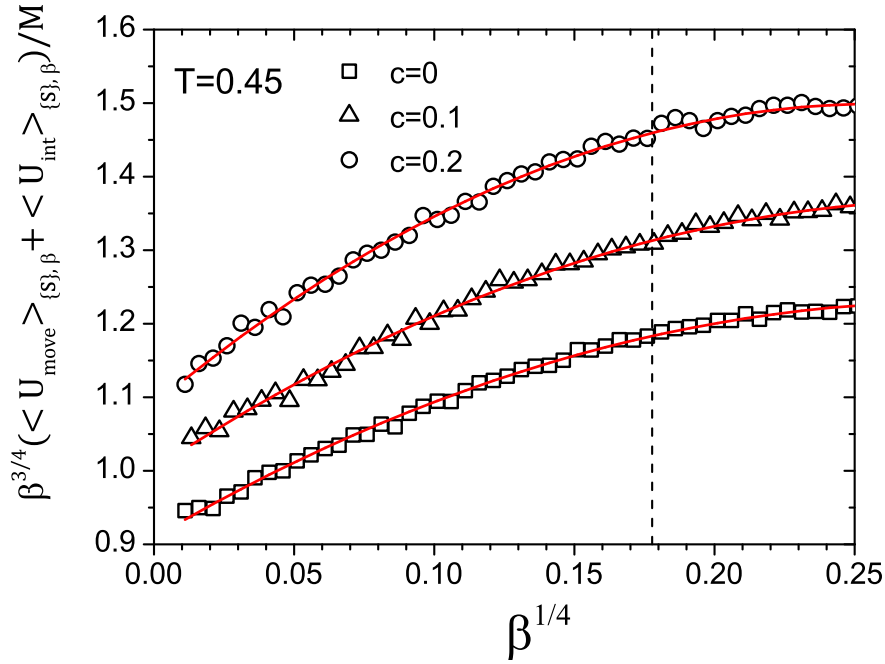


Figure C.1:  $\beta^{3/4}(\langle U_{\text{move}} \rangle_{\{\mathbf{s}\}} + \langle U_{\text{int}} \rangle_{\{\mathbf{s}\}})/M$  as a function of  $\beta^{1/4}$  at very high  $T$  ( $> 250$ ). The red fitting curves are obtained by  $\beta^{3/4}(\langle U_{\text{move}} \rangle_{\{\mathbf{s}\}} + \langle U_{\text{int}} \rangle_{\{\mathbf{s}\}}) = A + B(\beta^{1/4}) + C(\beta^{1/4})^2 + \mathcal{O}((\beta^{1/4})^3)$ , *i.e.*, a quadratic function of  $\beta^{1/4}$ . The vertical dashed line is the position of  $\beta_0$  at which the analytical integration starts.

Next step is to introduce  $\beta_0$  where the extrapolation starts from, and the integration is decomposed into an analytical and a numerical integration parts,

$$\int_0^{\beta^*} d\beta (\langle U_{\text{move}} \rangle_{\{\mathbf{s}\}} + \langle U_{\text{int}} \rangle_{\{\mathbf{s}\}}) = \int_0^{\beta_0} d\beta (A\beta^{-3/4} + B\beta^{-1/2} + C\beta^{-1/4} + \mathcal{O}(1)) + \int_{\beta_0}^{\beta^*} d\beta (\langle U_{\text{move}} \rangle_{\{\mathbf{s}\}} + \langle U_{\text{int}} \rangle_{\{\mathbf{s}\}}). \quad (\text{C.2.9})$$

Finally, we obtain the expression of  $\tilde{S}(\{\mathbf{s}\} : \beta^*)$ ,

$$\begin{aligned} \tilde{S}(\{\mathbf{s}\} : \beta^*) &= M \left\{ 1 - \log \left( \frac{M}{V} \right) \right\} - M_A \log \left( \frac{M_A}{M} \right) - M_B \log \left( \frac{M_B}{M} \right) - 3M(\log \Lambda)_{\beta=\beta^*} + \frac{3M}{2} \\ &\quad + (\beta \langle U_{\text{move}} \rangle_{\{\mathbf{s}\}} + \beta \langle U_{\text{int}} \rangle_{\{\mathbf{s}\}})_{\beta=\beta^*} - 4A\beta_0^{1/4} - 2B\beta_0^{1/2} - (4C/3)\beta_0^{3/4} + \mathcal{O}(\beta_0) \\ &\quad - \int_{\beta_0}^{\beta^*} d\beta (\langle U_{\text{move}} \rangle_{\{\mathbf{s}\}} + \langle U_{\text{int}} \rangle_{\{\mathbf{s}\}}). \end{aligned} \quad (\text{C.2.10})$$

The parameters,  $A$ ,  $B$ , and  $C$ , are obtained by fitting Eq. (C.2.8) with the simulation data and the last integration is evaluated using the Simpson's rule. In this study, we set  $\beta_0 = 0.001$ .

The total entropy of the pinned system is obtained by taking the quenched average for  $\tilde{S}(\{\mathbf{s}\} : T)$ ,

$$S(c, T) = \int d\{\mathbf{s}\} P_{\text{pin}}(\{\mathbf{s}\} : T) \tilde{S}(\{\mathbf{s}\} : T). \quad (\text{C.2.11})$$

### C.3 Vibrational entropy of the pinned systems

In this section, we derive the vibrational entropy using the harmonic approximation for the pinned systems. First, we explain the method to map the equilibrium configuration of  $M$  mobile particles  $\{\mathbf{r}\}$  to that of the inherent structure (IS)  $\{\mathbf{r}_{\text{IS}}\}$  by a potential energy minimization. The ISs are the local minima of the potential energy. The potential energy,  $U(\{\mathbf{s}\}, \{\mathbf{r}\})$  is minimized by the conjugate-gradient method. Note that only the degree of freedoms of the mobile particles  $\{\mathbf{r}\}$  are optimized and those of the pinned particles  $\{\mathbf{s}\}$  are fixed during the optimization process. Once the minimization of the potential energy are completed and the IS coordinates are evaluated, we expand  $U$  around  $\{\mathbf{r}_{\text{IS}}\}$ .

$$U_{\text{vib}}(\{\mathbf{s}\}, \{\mathbf{r}\}) = U(\{\mathbf{s}\}, \{\mathbf{r}_{\text{IS}}\}) + \frac{1}{2} \sum_{i,j} \frac{\partial^2 U(\{\mathbf{s}\}, \{\mathbf{r}_{\text{IS}}\})}{\partial \mathbf{r}_i \partial \mathbf{r}_j} \delta \mathbf{r}_i \delta \mathbf{r}_j. \quad (\text{C.3.1})$$

The first derivative is zero since the IS is the minimum of the potential energy. Then, the vibrational free energy is evaluated as

$$\begin{aligned} \tilde{F}_{\text{vib}}(\{\mathbf{s}\} : T) &= -T \log \frac{1}{\Lambda^{3M} M_A! M_B!} \int d\{\mathbf{r}\} \exp[-\beta U_{\text{vib}}(\{\mathbf{s}\}, \{\mathbf{r}\})] \\ &= -T \log \frac{\exp[-\beta U(\{\mathbf{s}\}, \{\mathbf{r}_{\text{IS}}\})]}{\Lambda^{3M}} \int d\{q\} \exp[-\frac{\beta}{2} \sum_{a=1}^{3M} \lambda_a q_a^2] \\ &= U(\{\mathbf{s}\}, \{\mathbf{r}_{\text{IS}}\}) + 3MT \log \Lambda - \frac{T}{2} \sum_{a=1}^{3M} \log \frac{2\pi}{\beta \lambda_a}. \end{aligned} \quad (\text{C.3.2})$$

In the second equality, we diagonalize  $(3M \times 3M)$  Hessian matrix  $\partial^2 U / \partial \mathbf{r}_i \partial \mathbf{r}_j$  and change the variables from  $\{\mathbf{r}\}$  to the normal coordinate  $\{q\} = (q_1, q_2, \dots, q_{3M})$  of the Hessian matrix.  $\lambda_a$  are the eigenvalues of the Hessian.

The energy of the system is  $\langle \tilde{H} \rangle_{\text{vib}\{\mathbf{s}\}} = \partial(\beta \tilde{F}_{\text{vib}}) / \partial \beta$ . Therefore, the vibrational entropy  $\tilde{S}_{\text{vib}}(\{\mathbf{s}\} : T)$  under a fixed realization  $\{\mathbf{s}\}$  is given by,

$$\begin{aligned} \tilde{S}_{\text{vib}}(\{\mathbf{s}\} : T) &= \beta (\langle \tilde{H} \rangle_{\text{vib}\{\mathbf{s}\}} - \tilde{F}_{\text{vib}}(\{\mathbf{s}\} : T)) \\ &= 3M(1 - \log \Lambda) + \frac{1}{2} \sum_{a=1}^{3M} \log \frac{2\pi}{\beta \lambda_a} \\ &= \sum_{a=1}^{3M} \{1 - \log(\beta \hbar \omega_a)\}, \end{aligned} \quad (\text{C.3.3})$$

where  $\omega_a = \sqrt{\lambda_a/m}$ . Numerically, we diagonalize the Hessian matrix and get the eigenvalues  $\omega_a$ . The three lowest modes are left out from the summation in Eq. (C.3.3) since they are modes of the translational invariance.

Finally, we get the vibrational entropy of the pinned system,

$$S_{\text{vib}}(c, T) = \int d\{\mathbf{s}\} P_{\text{pin}}(\{\mathbf{s}\} : T) \tilde{S}_{\text{vib}}(\{\mathbf{s}\} : T). \quad (\text{C.3.4})$$

## C.4 Anharmonic contribution for the vibrational entropy

In this section, we evaluate the anharmonic contribution for  $S_{\text{vib}}$ . Details of this method is described in Ref. [73] for the bulk system. Extension of the method to the pinned system is straightforward.

The anharmonic contribution of the potential energy  $\tilde{U}_{\text{anh}}(\{\mathbf{s}\} : T)$  for a pinning realization is given by

$$\tilde{U}_{\text{anh}}(\{\mathbf{s}\} : T) = \tilde{U}(\{\mathbf{s}\} : T) - \tilde{U}_{\text{IS}}(\{\mathbf{s}\} : T) - \frac{3}{2}Mk_B T, \quad (\text{C.4.1})$$

where  $\tilde{U}(\{\mathbf{s}\} : T) = \langle U(\{\mathbf{s}\}, \{\mathbf{r}\}) \rangle$  and  $M = N(1 - c)$ . The last term is the energy of the harmonic vibration of  $M$  mobile particles. The anharmonic contribution for the vibrational entropy for a realization  $\tilde{S}_{\text{anh}}(\{\mathbf{s}\} : T)$  is given by

$$\tilde{S}_{\text{anh}}(\{\mathbf{s}\} : T) = \int_0^T dT' \frac{1}{T'} \frac{\partial \tilde{U}_{\text{anh}}(\{\mathbf{s}\} : T')}{\partial T'}. \quad (\text{C.4.2})$$

We assumed that  $\tilde{S}_{\text{anh}}(\{\mathbf{s}\} : T = 0) = 0$  to derive the above equation, *i.e.*, there is no anharmonic contribution at  $T = 0$ .  $\tilde{U}_{\text{anh}}(\{\mathbf{s}\} : T)$  can be expanded by  $T$  around zero temperature.

$$\tilde{U}_{\text{anh}}(\{\mathbf{s}\} : T) = \sum_{k=2} \tilde{C}_k(\{\mathbf{s}\}) T^k, \quad (\text{C.4.3})$$

where  $\tilde{C}_k(\{\mathbf{s}\})$  is a  $T$  independent coefficient. We also assume the linear term in Eq. (C.4.3) is zero,  $\tilde{C}_1(\{\mathbf{s}\}) = 0$ , which means the anharmonic contribution for the specific heat vanishes at  $T = 0$ . Substituting Eq. (C.4.3) to Eq. (C.4.2), we obtain

$$\tilde{S}_{\text{anh}}(\{\mathbf{s}\} : T) = \sum_{k=2} \frac{k}{k-1} \tilde{C}_k(\{\mathbf{s}\}) T^{k-1}. \quad (\text{C.4.4})$$

Taking the quenched average for Eq. (C.4.1), Eq. (C.4.3), and Eq. (C.4.4), we arrive at

$$U_{\text{anh}}(c, T) = U(T) - U_{\text{IS}}(c, T) - \frac{3}{2}Mk_B T, \quad (\text{C.4.5})$$

$$U_{\text{anh}}(c, T) = \sum_{k=2} C_k(c) T^k, \quad (\text{C.4.6})$$

$$S_{\text{anh}}(c, T) = \sum_{k=2} \frac{k}{k-1} C_k(c) T^{k-1}, \quad (\text{C.4.7})$$

where  $C_k(c) = \overline{\tilde{C}_k(\{\mathbf{s}\})}$ . The procedure for evaluating  $S_{\text{anh}}$  is as follows [73]. First, we compute  $U_{\text{anh}}(c, T)$  by the simulation. Then, the coefficients  $C_k(c)$ 's are obtained by fitting  $U_{\text{anh}}(c, T)$  as a function of  $T$ . In this thesis, we use the first two terms,  $C_2(c)$  and  $C_3(c)$ , for the fitting [138]. Finally,  $S_{\text{anh}}(c, T)$  is evaluated by Eq. (C.4.7). This means the signs of  $C_k(c)$ 's determine the sign of  $S_{\text{anh}}$ . In Fig. C.2(a), the simulation data of  $U_{\text{anh}}(c, T)$  are plotted for several  $c$ 's. The dashed curve is an extrapolated curve down to  $T = 0$ .  $S_{\text{anh}}$  is shown in Fig. C.2(b). We find that  $S_{\text{anh}}$  is small and negative [73, 138] for all  $c$ 's and  $T$ 's, and the order is comparable to the negative values found in Fig. 3.2(b). Evaluation of the exact values of this corrections is difficult since we rely on extrapolation down to  $T = 0$ . More direct method such as the Frenkel-Ladd method [139] is required for this end.

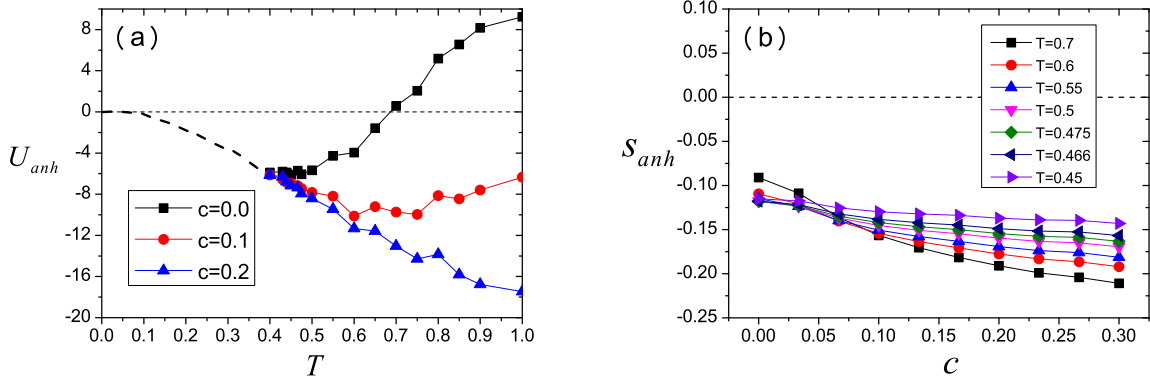


Figure C.2: (a) The anharmonic potential energy  $U_{anh}(c, T)$  for several  $c$ 's. The dashed curve is an extrapolation down to  $T = 0$ . The curve is drawn by hand. (b) The anharmonic contribution of the vibrational entropy  $s_{anh}(c, T) = S_{anh}(c, T)/N(1 - c)$  per a particle as a function of  $c$  for several  $T$ 's. The system size is  $N = 300$ .

## C.5 Finite size effect

In Fig. C.3, we show the  $S_c$  for  $N = 150$  and  $300$  for several state points. We find that finite size effects are small at least for these two system sizes.

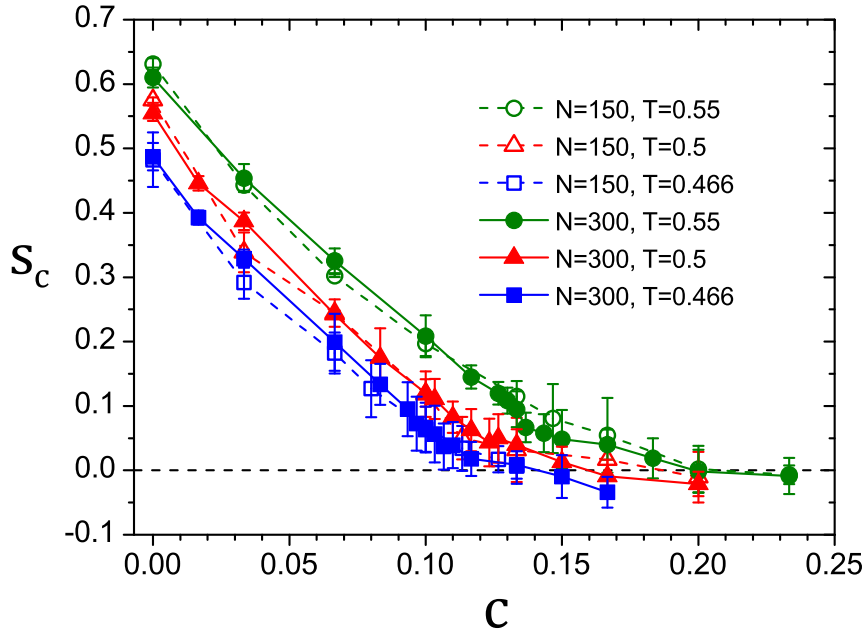


Figure C.3: Finite size effect of the configurational entropy for  $N = 150$  and  $N = 300$ .



# Appendix D

## Effects of pinning on glass states

### D.1 Effects of pinning on the vibrational entropy of the glass states

In this appendix, we discuss effects of the pinning on the vibrational properties of the glass states. The goal of this appendix is to understand the linear  $c$  dependence of  $S_{\text{vib}}$  found in Fig. 3.2(a). Intuitively, the pinning is expected to kill the excitation at long wave lengths and low frequency vibrational modes, thus  $S_{\text{vib}}$  is suppressed by the pinning. We discuss this argument more quantitatively by using the density of states.

We consider the bulk ( $c = 0$ ) case to introduce the notation. The harmonic vibrational entropy of the solid is

$$\begin{aligned}
 S_{\text{vib}}(T) &= \sum_{a=1}^{3N} \{1 - \log(\beta \hbar \omega_a(T))\} \\
 &= \sum_{a=1}^{3N} \left( \int_0^\infty d\omega \delta(\omega - \omega_a(T)) \right) \{1 - \log(\beta \hbar \omega_a(T))\} \\
 &= \int_0^\infty d\omega D(T, \omega) \{1 - \log(\beta \hbar \omega)\},
 \end{aligned} \tag{D.1.1}$$

where  $D(T, \omega) = \sum_{a=1}^{3N} \delta(\omega - \omega_a(T))$  is the density of states (DOS). In the second equality, we inserted the identity  $1 = \int_0^\infty d\omega \delta(\omega - \omega_a(T))$ .

Next we consider the pinning ( $c > 0$ ) case. We discuss the harmonic vibrational entropy  $\tilde{S}_{\text{vib}}(\{\mathbf{s}\} : T)$  under a fixed realization  $\{\mathbf{s}\}$ . As we have discussed in Appendix C,  $\tilde{S}_{\text{vib}}(\{\mathbf{s}\} : T)$  is written as

$$\begin{aligned}
 \tilde{S}_{\text{vib}}(\{\mathbf{s}\} : T) &= \sum_{a=1}^{3N(1-c)} \{1 - \log(\beta \hbar \omega_a(\{\mathbf{s}\} : T))\} \\
 &= \sum_{a=1}^{3N(1-c)} \left( \int_0^\infty d\omega \delta(\omega - \omega_a(\{\mathbf{s}\} : T)) \right) \{1 - \log(\beta \hbar \omega_a(\{\mathbf{s}\} : T))\} \\
 &= \int_0^\infty d\omega \tilde{D}(\{\mathbf{s}\} : T, \omega) \{1 - \log(\beta \hbar \omega)\},
 \end{aligned} \tag{D.1.2}$$

where  $\tilde{D}(\{\mathbf{s}\} : T, \omega) = \sum_{a=1}^{3N(1-c)} \delta(\omega - \omega_a(\{\mathbf{s}\} : T))$  is the DOS of the pinned system. We take quenched average,  $\overline{\cdot}$ , for  $\tilde{S}_{\text{vib}}(\{\mathbf{s}\} : T)$ , then we get  $S_{\text{vib}}$  as functions of  $c$  and  $T$ ,

$$S_{\text{vib}}(c, T) = \overline{\tilde{S}_{\text{vib}}(\{\mathbf{s}\} : T)} = \int_0^\infty d\omega D(c, T, \omega) \{1 - \log(\beta \hbar \omega)\}, \tag{D.1.3}$$

where,  $D(c, T, \omega) = \overline{\tilde{D}(\{\mathbf{s}\} : T, \omega)}$ . This expression tells us that  $D(c, T, \omega)$  contains all information about the pinning. Thus, we can understand the  $c$  dependence of  $S_{\text{vib}}$  via  $D(c, T, \omega)$ .

### Pinning kills low frequency modes

In the presence of the pinned particles, there is a characteristic length  $\xi_{\text{pin}} \sim c^{-1/d}$  in arbitrary dimension  $d$ . It is expected that the vibrational modes with the length larger than  $\xi_{\text{pin}}$  are suppressed in the presence of the pinning. Therefore, a certain cutoff wave number,  $k_c \sim 1/\xi_{\text{pin}}$ , should be present. If we assume the dispersion relation is linear at low  $\omega$ , the cutoff frequency  $\omega_c$  is given by

$$\omega_c \sim k_c \sim c^{1/d}. \quad (\text{D.1.4})$$

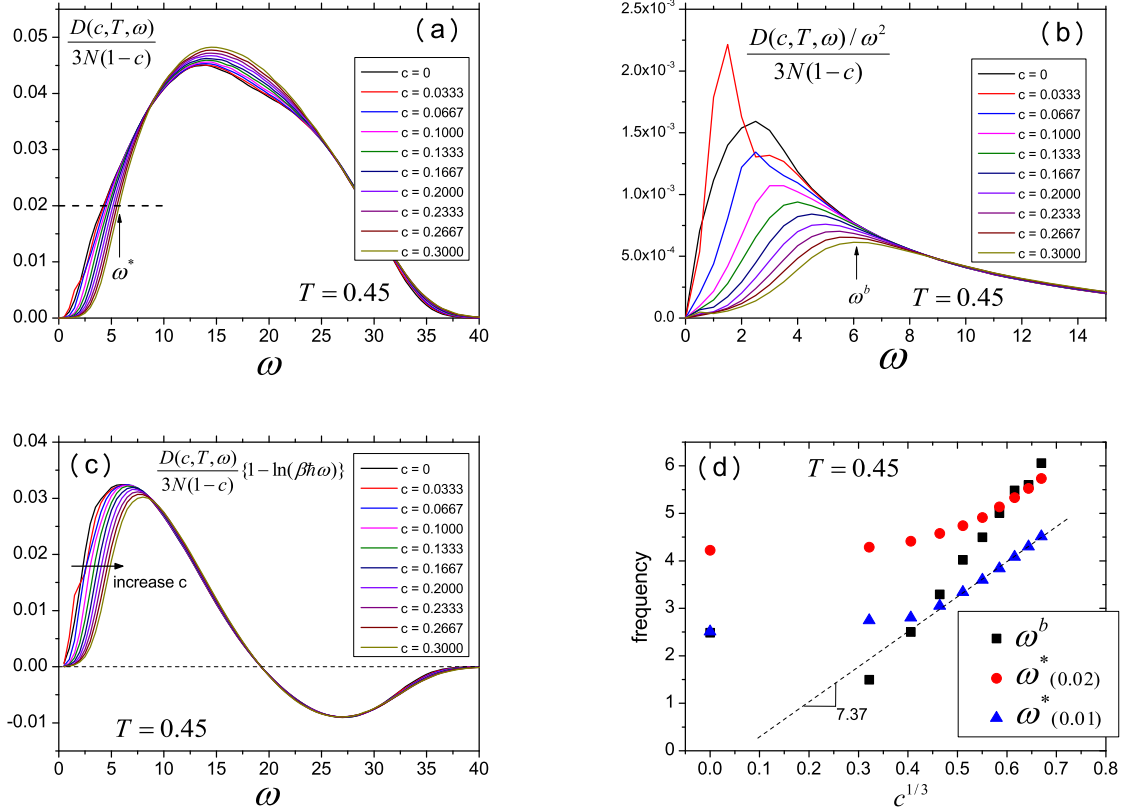


Figure D.1: (a) The DOS,  $D(c, T, \omega)$ , normalized by  $N(1 - c)$ . We define a characteristic frequency  $\omega^*$  by  $D(c, T, \omega^*) = 0.02$ . (b)  $D(c, T, \omega)$  normalized by  $\omega^2$ . We define another characteristic frequency  $\omega^b$  as the position of the peak. (c)  $\frac{D(c, T, \omega)}{3N(1-c)} \{1 - \log(\beta \hbar \omega)\}$ . This is the integrand of  $S_{\text{vib}}(c, T)/3$ . (d)  $\omega^*$  and  $\omega^b$  as a function of  $c^{1/3}$ .

Here we discuss this argument through the numerical observations in Fig. D.1. We show the DOS normalized by the number of the modes,  $3N(1 - c)$ , for several  $c$ 's in Fig. D.1(a). We find that whereas the shape of the DOS hardly changes at higher frequencies ( $\omega \gtrsim 25$ ) as increasing  $c$ , the low frequency modes ( $\omega \lesssim 8$ ) are significantly suppressed by the pinning. We can highlight this suppression of the low frequency modes by normalizing the DOS by  $\omega^2$  as shown in Fig. D.1(b). Note that a shape peak observed in  $c = 0.0333$  is thought to be modified modes of the translational invariance [140]. To evaluate the contribution of the suppression of the low frequency modes to the decrease of  $S_{\text{vib}}(c, T)$ , we compute the integrand of the RHS of Eq. (D.1.3) as shown in Fig. D.1(c). The figure clearly shows that the main contribution of the decreasing of  $S_{\text{vib}}(c, T)$  is the suppression of the low frequency modes ( $\omega \lesssim 8$ ). Next, we discuss validity of Eq. (D.1.4). It is difficult to measure  $\omega_c$  directly in the numerical simulation. Instead, we define two characteristic frequencies,  $\omega^*$  and  $\omega^b$  and examine their  $c$  dependences.  $\omega^*$  is defined as  $D(c, T, \omega^*) = 0.01$  or  $0.02$  and  $\omega^b$  is the position of the peak in Fig. D.1(b). We plot  $\omega^*(0.01)$ ,  $\omega^*(0.02)$ , and  $\omega^b$  as a function of  $c^{1/3}$  in Fig. D.1(d). We find that

these frequencies increase with increasing  $c$  and show straight lines except low  $c$  regions, which means these characteristic frequencies are proportional to  $c^{1/3}$  at least high  $c$  regions.

From these numerical observations, the suppression of the low frequency modes in  $D(c, T, \omega)$  is indeed the main contribution of decreasing of  $S_{\text{vib}}(c, T)$ . Here we try to model  $D(c, T, \omega)$  to calculate the  $c$  dependence of  $S_{\text{vib}}(c, T)$  explicitly. A simple approximation is adding the cutoff via the Heaviside's step function  $\theta(x)$ .

$$\frac{D(c, T, \omega)}{3N(1-c)} \simeq \frac{D(T, \omega)}{3N} \theta(\omega - \omega_c). \quad (\text{D.1.5})$$

Under this assumption, we can write down a relation between  $S_{\text{vib}}(c, T)$  and  $S_{\text{vib}}(T)$ ,

$$\begin{aligned} S_{\text{vib}}(c, T) &= \int_0^\infty d\omega (1-c) D(T, \omega) \theta(\omega - \omega_c) \{1 - \log(\beta \hbar \omega)\} \\ &= (1-c) \int_{\omega_c}^\infty d\omega D(T, \omega) \{1 - \log(\beta \hbar \omega)\} \\ &= (1-c) \int_0^\infty d\omega D(T, \omega) \{1 - \log(\beta \hbar \omega)\} - (1-c) \int_0^{\omega_c} d\omega D(T, \omega) \{1 - \log(\beta \hbar \omega)\} \\ &= (1-c) S_{\text{vib}}(T) - (1-c) \int_0^{\omega_c} d\omega D(T, \omega) \{1 - \log(\beta \hbar \omega)\}. \end{aligned} \quad (\text{D.1.6})$$

Then, the above equation can be rewritten by using intensive value.

$$\frac{S_{\text{vib}}(c, T)}{N(1-c)} = \frac{S_{\text{vib}}(T)}{N} + (\text{c dependent term}). \quad (\text{D.1.7})$$

The explicit expression of the last term of the RHS is

$$(\text{c dependent term}) = -\frac{1}{N} \int_0^{\omega_c} d\omega D(T, \omega) \{1 - \log(\beta \hbar \omega)\}. \quad (\text{D.1.8})$$

In order to investigate further, we have to evaluate  $D(T, \omega)$  in the second term somehow. Here we assume the Debye's model,

$$D(T, \omega) \simeq A\omega^2, \quad (\text{D.1.9})$$

where  $A$  is a constant. Using the Debye's model is a crude approximation but it is widely believed that the vibrational entropy of the glass states and the entropy of the crystal are close.

$$\begin{aligned} (\text{c dependent term}) &= -\frac{A}{N} \int_0^{\omega_c} d\omega \omega^2 \{1 - \log(\beta \hbar \omega)\} \\ &= \frac{A\omega_c^3}{3N} \left( \frac{4}{3} - \log(\beta \hbar \omega_c) \right). \end{aligned} \quad (\text{D.1.10})$$

Finally, using  $\omega_c = Bc^{1/3}$ , we arrive at

$$(\text{c dependent term}) = \frac{AB^3}{3N} c \left( \frac{4}{3} - \frac{1}{3} \log c - \log(\beta \hbar B) \right). \quad (\text{D.1.11})$$

If we neglect the  $\log(\beta \hbar B)$  term, we reproduce the  $c$ -dependence. We show such function in Fig. D.2(a).

## Discussions

We have derived the  $c$  dependence of  $S_{\text{vib}}$  in Eq. (D.1.11). In the derivation, we have used several approximations and assumptions. We discuss these approximations and assumptions in the following.

(1) Eq. (D.1.4): In this assumption, the definition of  $\omega_c$  is somewhat ambiguous. Thus, we have not extracted  $\omega_c$  from the simulation data directly. Instead, we have evaluated two characteristic frequencies,  $\omega^*$  and  $\omega^b$ . These frequencies show linear dependences of  $c^{1/3}$ . Thus, we can speculate

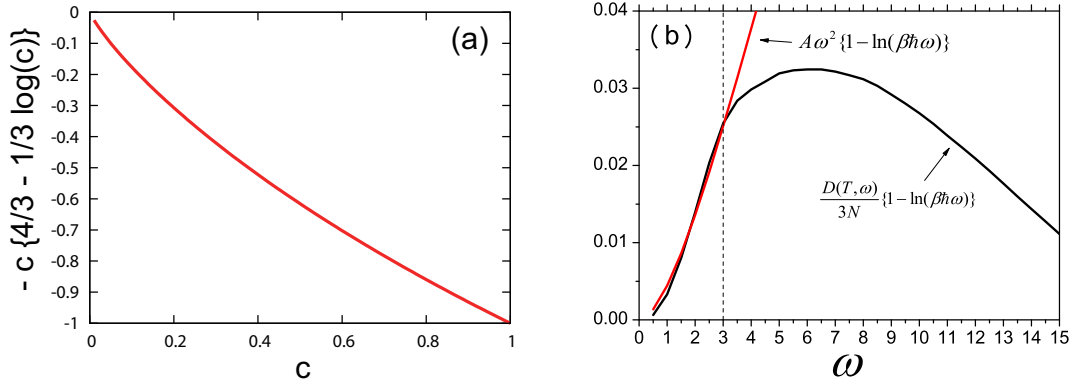


Figure D.2: (a)  $-c\{4/3 - 1/3 \log(c)\}$ . (b)  $D(T, \omega)/3N\{1 - \log(\beta\hbar\omega)\}$  of the simulation data (black line) and the Debye's model (red line).

that these frequencies capture the physical trend of  $\omega_c$ . However, the relationship among  $\omega^*$ ,  $\omega^b$ , and  $\omega_c$  is left for the future works.

(2) Eq. (D.1.5): In this approximation, the normalization of  $D(c, T, \omega)$  does not hold since modes at  $\omega < \omega_c$  are just killed. This means that one assume that high  $\omega$  modes do not contribute to  $S_{\text{vib}}$  so much. The integrand of  $S_{\text{vib}}(c, T)$  in Fig. D.1(c) justifies this assumption since only  $\omega \lesssim 8$  modes contribute to the integration.

(3) Eq. (D.1.9): To examine validity of this approximation, we compare the Debye's model ( $\omega^2$ ) and  $D(T, \omega)$  obtained by the simulation in Fig. D.2(b). This figure shows that at  $\omega < 3$  the Debye's model reproduces real  $D(T, \omega)$ . In other words, the Debye's model is valid only  $\omega < 3$ . Therefore, this approximation can not cover  $3 < \omega \lesssim 8$ , where the suppression of the low frequency modes are observed.

## Appendix E

# Saddle points and dynamic transition point

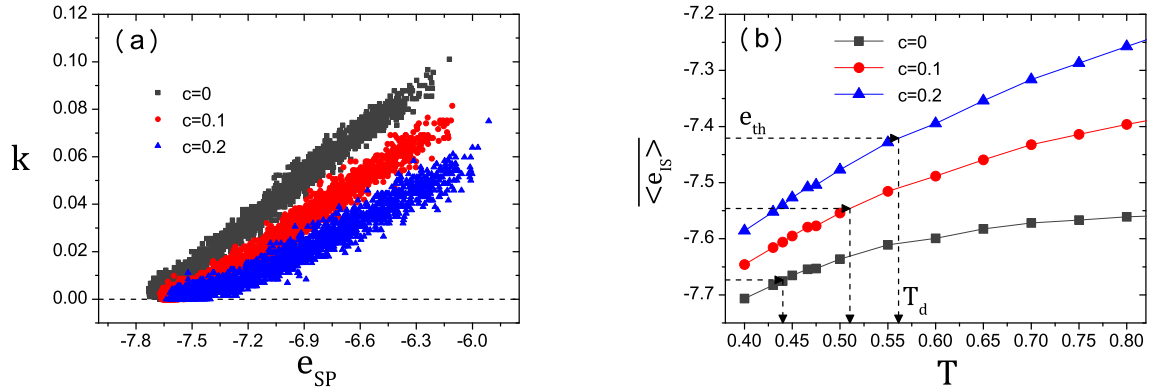


Figure E.1: (a) The scatter plot of  $k$  vs.  $e_{SP}$ . (b) The  $\overline{\langle e_{IS} \rangle}$  as a function of  $T$ . The horizontal and vertical arrows indicate the location of  $e_{th}(c)$  and  $T_d(c)$ , respectively. This plot is used to map  $e_{th}(c)$  to  $T_d(c)$ .

In Fig. E.1(a), we show the original data of Fig. 3.5(b) in Chap. 3. This scatter plot shows the normalized saddle index  $k$  as a function of the energy at the saddle,  $e_{SP}$ , obtained from the minimization of the square gradient potential  $W = \frac{1}{2}|\nabla U|^2$  [75, 76]. Fig. 3.5(b) has been obtained by averaging over this scatter data for a given  $e_{SP}$ . The threshold energy  $e_{th}$  is extracted from Fig. 3.5(b) as a point at which the averaged  $k$  vanishes. Mapping of  $e_{th}(c)$  to the dynamic transition temperature  $T_d(c)$  can be done by plotting the temperature dependence of the inherent structures  $\overline{\langle e_{IS} \rangle}$ . The reason why we use the inherent structures  $\overline{\langle e_{IS} \rangle}$  instead of  $\langle e_{SP} \rangle$  is that in practice one can evaluate the  $T$  dependence of  $\overline{\langle e_{IS} \rangle}$  with higher precision than that of  $\langle e_{SP} \rangle$ . Note that using  $\langle e_{SP} \rangle$  would in fact give the same result since it is expected to be very close to  $\overline{\langle e_{IS} \rangle}$  in the low temperature regime. In Fig. E.1(b) we show the  $T$ -dependence of  $\overline{\langle e_{IS} \rangle}$  for several  $c$ 's. The inherent structures are found to be a monotonic function of  $T$  for all  $c$ 's and therefore  $e_{th}$  can be uniquely mapped to  $T_d$ .



# Acknowledgment

The author thanks to all those who have supported me during my PhD course.

I would express my appreciation to the PhD adviser Prof. Kunimasa Miyazaki for guiding me to a splendid research field. Besides my adviser, I would like to thank the dissertation committee: Prof. Yasuhiro Hatsugai, Prof. Yasuhiro Tokura, and Prof. Susumu Okada for insightful discussions and comments. Particularly I am deeply grateful to Prof. Yasuhiro Hatsugai for administrative supports during the PhD course.

I would also like to thank collaborators, Prof. Kang Kim (Chapter 2), Prof. Walter Kob (Chapter 3), Prof. Atsushi Ikeda (Chapter 3 and 4) and Dr. Takeshi Kuroiwa (Chapter 4). Without their guidance and persistent help this thesis would not have been possible.

Special thanks to Prof. Kang Kim and Dr. Ryoji Miyazaki for careful reading the thesis and for giving valuable comments and discussions.

I am grateful to the members of soft matter theory group in University of Tsukuba and non-linear physics group in Nagoya University, Prof. Tetsuro Konishi, Prof. Atsushi Ikeda, Dr. Takeshi Kuroiwa, Dr. Ryoji Miyazaki, Shota Okazaki, Hiroya Fukuda, Hironori J. Matsuyama, Shoko Sugae, Harukuni Ikeda, Hideki Fujii, Hironobu Iga, Mitsuhiro Tanabe, and Yoshiaki Eguchi.

I want to thank many friends in the University of Tsukuba. I could spend an exciting time with these crazy guys.

Finally, I appreciate my family for everyday encouragement.



# Bibliography

- [1] Pablo G Debenedetti and Frank H Stillinger. Supercooled liquids and the glass transition. *Nature*, 410(6825):259–267, 2001.
- [2] Andrea Cavagna. Supercooled liquids for pedestrians. *Physics Reports*, 476(4):51–124, 2009.
- [3] Ronald G Larson. *The Structure and Rheology of Complex Fluids*, volume 4. Oxford University Press New York, 1999.
- [4] Jean-Pierre Hansen and IR McDonald. *Theory of Simple Liquids*. Academic Press, 2006.
- [5] C Austen Angell. Formation of glasses from liquids and biopolymers. *Science*, 267(5206):1924–1935, 1995.
- [6] Walter Kob and Hans C Andersen. Testing mode-coupling theory for a supercooled binary lennard-jones mixture. ii. intermediate scattering function and dynamic susceptibility. *Physical Review E*, 52(4):4134, 1995.
- [7] Walter Kob and Hans C Andersen. Testing mode-coupling theory for a supercooled binary lennard-jones mixture i: The van hove correlation function. *Physical Review E*, 51(5):4626, 1995.
- [8] Paul M Chaikin and Tom C Lubensky. *Principles of Condensed Matter Physics*, volume 1. Cambridge University Press, 2000.
- [9] Merdith G Evans and Michael Polanyi. Some applications of the transition state method to the calculation of reaction velocities, especially in solution. *Trans. Faraday Soc.*, 31:875–894, 1935.
- [10] Greer A. Lindsay, F. Kelton Kenneth, and Sastry Srikanth. *Fragility of Glass-Forming Liquids*. Hindustan Book Agency, 2014.
- [11] JA Bucaro and HD Dardy. High-temperature strain relaxation in silica by optical correlation spectroscopy. *Journal of Non-Crystalline Solids*, 24(1):121–129, 1977.
- [12] Paul K Dixon and Sidney R Nagel. Frequency-dependent specific heat and thermal conductivity at the glass transition in o-terphenyl mixtures. *Physical Review Letters*, 61(3):341, 1988.
- [13] Roland Böhmer, KL Ngai, CA Angell, and DJ Plazek. Nonexponential relaxations in strong and fragile glass formers. *The Journal of Chemical Physics*, 99(5):4201–4209, 1993.
- [14] CA Angell. Structural instability and relaxation in liquid and glassy phases near the fragile liquid limit. *Journal of Non-Crystalline Solids*, 102(1):205–221, 1988.
- [15] Ludovic Berthier, Giulio Biroli, Jean-Philippe Bouchaud, Luca Cipelletti, and Wim van Saarloos. *Dynamical Heterogeneities in Glasses, Colloids, and Granular Media*. Oxford University Press, 2011.
- [16] Th Bauer, P Lunkenheimer, and A Loidl. Cooperativity and the freezing of molecular motion at the glass transition. *Physical Review Letters*, 111(22):225702, 2013.

- [17] T. R. Kirkpatrick, D. Thirumalai, and P. G. Wolynes. Scaling concepts for the dynamics of viscous liquids near an ideal glassy state. *Physical Review A*, 40:1045–1054, Jul 1989.
- [18] Walter Kauzmann. The nature of the glassy state and the behavior of liquids at low temperatures. *Chemical Reviews*, 43(2):219–256, 1948.
- [19] Julian H Gibbs and Edmund A DiMarzio. Nature of the glass transition and the glassy state. *The Journal of Chemical Physics*, 28(3):373–383, 1958.
- [20] V Lubchenko and PG Wolynes. Theory of structural glasses and supercooled liquids. *Annual Review of Physical Chemistry*, 58:235–266, 2006.
- [21] Francesco Sciortino, W Kob, and Piero Tartaglia. Inherent structure entropy of supercooled liquids. *Physical Review Letters*, 83(16):3214, 1999.
- [22] Salvatore Torquato and Frank H Stillinger. Jammed hard-particle packings: From kepler to bernal and beyond. *Reviews of Modern Physics*, 82(3):2633, 2010.
- [23] Corey S O’Hern, Leonardo E Silbert, Andrea J Liu, and Sidney R Nagel. Jamming at zero temperature and zero applied stress: The epitome of disorder. *Physical Review E*, 68(1):011306, 2003.
- [24] J Clerk Maxwell. L. on the calculation of the equilibrium and stiffness of frames. *The London, Edinburgh, and Dublin Philosophical Magazine and Journal of Science*, 27(182):294–299, 1864.
- [25] Andrea J Liu and Sidney R Nagel. Nonlinear dynamics: Jamming is not just cool any more. *Nature*, 396(6706):21–22, 1998.
- [26] Pinaki Chaudhuri, Ludovic Berthier, and Srikanth Sastry. Jamming transitions in amorphous packings of frictionless spheres occur over a continuous range of volume fractions. *Physical Review Letters*, 104:165701, Apr 2010.
- [27] MP Allen and DJ Tildesley. Computer simulation of liquids, 1987. *New York: Oxford*, 385, 1989.
- [28] Ludovic Berthier and Walter Kob. The monte carlo dynamics of a binary lennard-jones glass-forming mixture. *Journal of Physics: Condensed Matter*, 19(20):205130, 2007.
- [29] Kurt Binder and Walter Kob. *Glassy Materials and Disordered Solids: An Introduction to their Statistical Mechanics*. World Scientific, 2011.
- [30] B Bernu, JP Hansen, Y Hiwatari, and G Pastore. Soft-sphere model for the glass transition in binary alloys: Pair structure and self-diffusion. *Physical Review A*, 36(10):4891, 1987.
- [31] BWH Van Beest, Gert Jan Kramer, and RA Van Santen. Force fields for silicas and aluminophosphates based on ab initio calculations. *Physical Review Letters*, 64(16):1955, 1990.
- [32] Daniele Coslovich and Giorgio Pastore. Dynamics and energy landscape in a tetrahedral network glass-former: direct comparison with models of fragile liquids. *Journal of Physics: Condensed Matter*, 21(28):285107, 2009.
- [33] Srikanth Sastry. The relationship between fragility, configurational entropy and the potential energy landscape of glass-forming liquids. *Nature*, 409(6817):164–167, 2001.
- [34] Ludovic Berthier and Thomas A Witten. Compressing nearly hard sphere fluids increases glass fragility. *Europhysics Letters*, 86(1):10001, 2009.
- [35] Shiladitya Sengupta, Thomas B Schröder, and Srikanth Sastry. Density-temperature scaling of the fragility in a model glass-former. *The European Physical Journal. E*, 36(12), 2013.

- [36] Takeshi Kawasaki and Hajime Tanaka. Structural origin of dynamic heterogeneity in three-dimensional colloidal glass formers and its link to crystal nucleation. *Journal of Physics: Condensed Matter*, 22(23):232102, 2010.
- [37] D Coslovich and G Pastore. Understanding fragility in supercooled lennard-jones mixtures. 1. locally preferred structures. *The Journal of Chemical Physics*, 127(12):124504, 2007.
- [38] Sneha Elizabeth Abraham, Sarika Maitra Bhattacharaya, and Biman Bagchi. Energy landscape, antiplasticization, and polydispersity induced crossover of heterogeneity in supercooled polydisperse liquids. *Physical Review Letters*, 100(16):167801\_1–167801\_4, 2008.
- [39] Cristiano De Michele, Francesco Sciortino, and Antonio Coniglio. Scaling in soft spheres: fragility invariance on the repulsive potential softness. *Journal of Physics: Condensed Matter*, 16(45):L489, 2004.
- [40] Patrice Bordat, Frédéric Affouard, Marc Descamps, and KL Ngai. Does the interaction potential determine both the fragility of a liquid and the vibrational properties of its glassy state? *Physical Review Letters*, 93(10):105502, 2004.
- [41] Shiladitya Sengupta, Filipe Vasconcelos, Frédéric Affouard, and Srikanth Sastry. Dependence of the fragility of a glass former on the softness of interparticle interactions. *The Journal of Chemical Physics*, 135(19):194503, 2011.
- [42] Ludovic Berthier and Gilles Tarjus. Nonperturbative effect of attractive forces in viscous liquids. *Physical Review Letters*, 103(17):170601, 2009.
- [43] Hiroshi Shintani and Hajime Tanaka. Frustration on the way to crystallization in glass. *Nature Physics*, 2(3):200–206, 2006.
- [44] Valeria Molinero, Srikanth Sastry, and C Austen Angell. Tuning of tetrahedrality in a silicon potential yields a series of monatomic (metal-like) glass formers of very high fragility. *Physical Review Letters*, 97(7):075701, 2006.
- [45] Emanuela Zaccarelli, Francesco Sciortino, and Piero Tartaglia. A spherical model with directional interactions. 1. static properties. *The Journal of Chemical Physics*, 127(17):174501, 2007.
- [46] Christian Mayer, Francesco Sciortino, Piero Tartaglia, and Emanuela Zaccarelli. A spherical model with directional interactions: 2. dynamics and landscape properties. *Journal of Physics: Condensed Matter*, 22(10):104110, 2010.
- [47] Ludovic Berthier, Giulio Biroli, Daniele Coslovich, Walter Kob, and Cristina Toninelli. Finite-size effects in the dynamics of glass-forming liquids. *Physical Review E*, 86(3):031502, 2012.
- [48] Kang Kim and Shinji Saito. Multiple length and time scales of dynamic heterogeneities in model glass-forming liquids: A systematic analysis of multi-point and multi-time correlations. *The Journal of Chemical Physics*, 138(12):12A506, 2013.
- [49] Takeshi Kawasaki, Kang Kim, and Akira Onuki. Dynamics in a tetrahedral network glass-former: Vibrations, network rearrangements, and diffusion. *The Journal of Chemical Physics*, 140(18):184502, 2014.
- [50] Daniele Coslovich. Connections between structure, dynamics and energy landscape in simple models of glass-forming liquids. 2008.
- [51] Peter J Heaney, Charles T Prewitt, and Gerald V Gibbs. *Silica: Physical Behavior, Geochemistry and Materials Applications*. Mineralogical Society of America Washington, DC, 1994.

- [52] Takenobu Nakamura, Yasuaki Hiraoka, Akihiko Hirata, Emerson G. Escobar, Kaname Matsue, and Yasumasa Nishiura. Description of medium-range order in amorphous structures by persistent homology. *arXiv preprint arXiv:1501.03611*, 2015.
- [53] Walter Kob, Sandalo Roldan-Vargas, and Ludovic Berthier. Spatial correlations in glass-forming liquids across the mode-coupling crossover. *Physics Procedia*, 34:70–79, 2012.
- [54] JC Mikkelsen Jr. Self-diffusivity of network oxygen in vitreous sio<sub>2</sub>. *Applied Physics Letters*, 45(11):1187–1189, 1984.
- [55] Jürgen Horbach and Walter Kob. Static and dynamic properties of a viscous silica melt. *Physical Review B*, 60(5):3169, 1999.
- [56] A Saksengwitt and A Heuer. Origin of the decoupling of oxygen and silicon dynamics in liquid silica as expressed by its potential energy landscape. *Physical Review E*, 74(5):051502, 2006.
- [57] Takeshi Kawasaki and Akira Onuki. Slow relaxations and stringlike jump motions in fragile glass-forming liquids: Breakdown of the stokes-einstein relation. *Physical Review E*, 87(1):012312, 2013.
- [58] Gerold Adam and Julian H Gibbs. On the temperature dependence of cooperative relaxation properties in glass-forming liquids. *The Journal of Chemical Physics*, 43(1):139–146, 1965.
- [59] Inyong Chang and Hans Sillescu. Heterogeneity at the glass transition: Translational and rotational self-diffusion. *The Journal of Physical Chemistry B*, 101(43):8794–8801, 1997.
- [60] Francesco Mallamace, Caterina Branca, Carmelo Corsaro, Nancy Leone, Jeroen Spooren, Sow-Hsin Chen, and H Eugene Stanley. Transport properties of glass-forming liquids suggest that dynamic crossover temperature is as important as the glass transition temperature. *Proceedings of the National Academy of Sciences*, 107(52):22457–22462, 2010.
- [61] Shiladitya Sengupta, Smarajit Karmakar, Chandan Dasgupta, and Srikanth Sastry. Breakdown of the stokes-einstein relation in two, three, and four dimensions. *The Journal of Chemical Physics*, 138(12):12A548, 2013.
- [62] Jean-Louis Barrat, James Badro, and Philippe Gillet. A strong to fragile transition in a model of liquid silica. *Molecular Simulation*, 20(1-2):17–25, 1997.
- [63] Ivan Saika-Voivod, Francesco Sciortino, and Peter H Poole. Free energy and configurational entropy of liquid silica: fragile-to-strong crossover and polyamorphism. *Physical Review E*, 69(4):041503, 2004.
- [64] VN Novikov, Y Ding, and AP Sokolov. Correlation of fragility of supercooled liquids with elastic properties of glasses. *Physical Review E*, 71(6):061501, 2005.
- [65] NA Mauro, M Blodgett, ML Johnson, AJ Vogt, and KF Kelton. A structural signature of liquid fragility. *Nature Communications*, 5, 2014.
- [66] Giulio Biroli and Jean-Philippe Bouchaud. The random first-order transition theory of glasses: A critical assessment. *Structural Glasses and Supercooled Liquids: Theory, Experiment, and Applications*, pages 31–113, 2012.
- [67] Juan P Garrahan and David Chandler. Coarse-grained microscopic model of glass formers. *Proceedings of the National Academy of Sciences*, 100(17):9710–9714, 2003.
- [68] D Chandler and JP Garrahan. Dynamics on the way to forming glass: bubbles in space-time. *Annual Review of Physical Chemistry*, 61:191–217, 2009.

- [69] Chiara Cammarota and Giulio Biroli. Ideal glass transitions by random pinning. *Proceedings of the National Academy of Sciences*, 109(23):8850–8855, 2012.
- [70] Chiara Cammarota and Giulio Biroli. Random pinning glass transition: Hallmarks, mean-field theory and renormalization group analysis. *The Journal of Chemical Physics*, 138(12):12A547, 2013.
- [71] Chiara Cammarota. A general approach to systems with randomly pinned particles: Unfolding and clarifying the random pinning glass transition. *Europhysics Letters*, 101(5):56001, 2013.
- [72] Frank H. Stillinger and Thomas A. Weber. Hidden structure in liquids. *Physical Review A*, 25:978–989, Feb 1982.
- [73] Francesco Sciortino. Potential energy landscape description of supercooled liquids and glasses. *Journal of Statistical Mechanics: Theory and Experiment*, 2005(05):P05015, 2005.
- [74] Wolfgang Götze. *Complex Dynamics of Glass-Forming Liquids: A Mode-Coupling Theory: A Mode-Coupling Theory*, volume 143. Oxford University Press, 2008.
- [75] L Angelani, R Di Leonardo, G Ruocco, A Scala, and F Sciortino. Saddles in the energy landscape probed by supercooled liquids. *Physical Review Letters*, 85(25):5356, 2000.
- [76] Kurt Broderix, Kamal K Bhattacharya, Andrea Cavagna, Annette Zippelius, and Irene Giardina. Energy landscape of a lennard-jones liquid: statistics of stationary points. *Physical Review Letters*, 85(25):5360, 2000.
- [77] K Kim. Effects of pinned particles on the structural relaxation of supercooled liquids. *Europhysics Letters*, 61(6):790, 2003.
- [78] Silvio Franz and Giorgio Parisi. Universality classes of critical points in constrained glasses. *Journal of Statistical Mechanics: Theory and Experiment*, 2013(11):P11012, 2013.
- [79] Giulio Biroli, Chiara Cammarota, Gilles Tarjus, and Marco Tarzia. Random-field-like criticality in glass-forming liquids. *Physical Review Letters*, 112(17):175701, 2014.
- [80] Walter Kob and Ludovic Berthier. Probing a liquid to glass transition in equilibrium. *Physical Review Letters*, 110(24):245702, 2013.
- [81] Koji Hukushima and Koji Nemoto. Exchange monte carlo method and application to spin glass simulations. *Journal of the Physical Society of Japan*, 65(6):1604–1608, 1996.
- [82] Ryoichi Yamamoto and Walter Kob. Replica-exchange molecular dynamics simulation for supercooled liquids. *Physical Review E*, 61(5):5473, 2000.
- [83] Srikanth Sastry. Evaluation of the configurational entropy of a model liquid from computer simulations. *Journal of Physics: Condensed Matter*, 12(29):6515, 2000.
- [84] Barbara Coluzzi, Giorgio Parisi, and Paolo Verrocchio. Lennard-jones binary mixture: a thermodynamical approach to glass transition. *The Journal of Chemical Physics*, 112(6):2933–2944, 2000.
- [85] J. Nocedal and S.J. Wright. *Numerical Optimization*. Springer verlag, 1999.
- [86] M. Goldstein. Viscous liquids and the glass transition: a potential energy barrier picture. *The Journal of Chemical Physics*, 51:3728, 1969.
- [87] David Wales. *Energy Landscapes: Applications to Clusters, Biomolecules and Glasses*. Cambridge University Press, 2003.

- [88] Srikanth Sastry, Pablo G Debenedetti, and Frank H Stillinger. Signatures of distinct dynamical regimes in the energy landscape of a glass-forming liquid. *Nature*, 393(6685):554–557, 1998.
- [89] G Ruocco, F Sciortino, F Zamponi, C De Michele, and T Scopigno. Landscapes and fragilities. *The Journal of Chemical Physics*, 120(22):10666–10680, 2004.
- [90] AJ Moreno, I Saika-Voivod, E Zaccarelli, E La Nave, SV Buldyrev, P Tartaglia, and F Sciortino. Non-gaussian energy landscape of a simple model for strong network-forming liquids: Accurate evaluation of the configurational entropy. *The Journal of Chemical Physics*, 124(20):204509, 2006.
- [91] Felix Höfling and Thomas Franosch. Crossover in the slow decay of dynamic correlations in the lorentz model. *Physical Review Letters*, 98(14):140601, 2007.
- [92] Benjamin Widom. Equation of state in the neighborhood of the critical point. *The Journal of Chemical Physics*, 43(11):3898–3905, 1965.
- [93] VV Brazhkin, Yu D Fomin, AG Lyapin, VN Ryzhov, and EN Tsiok. Widom line for the liquid-gas transition in lennard-jones system. *The Journal of Physical Chemistry B*, 115(48):14112–14115, 2011.
- [94] E Flenner and G Szamel. Hybrid monte carlo simulation of a glass-forming binary mixture. *Physical Review E*, 73(6):061505, 2006.
- [95] Yael S Elmatad, David Chandler, and Juan P Garrahan. Corresponding states of structural glass formers. *The Journal of Physical Chemistry B*, 113(16):5563–5567, 2009.
- [96] Aaron S Keys, Juan P Garrahan, and David Chandler. Calorimetric glass transition explained by hierarchical dynamic facilitation. *Proceedings of the National Academy of Sciences*, 110(12):4482–4487, 2013.
- [97] Smarajit Karmakar, Edan Lerner, and Itamar Procaccia. Direct estimate of the static length-scale accompanying the glass transition. *Physica A: Statistical Mechanics and its Applications*, 391(4):1001–1008, 2012.
- [98] Giulio Biroli, Smarajit Karmakar, and Itamar Procaccia. Comparison of static length scales characterizing the glass transition. *Physical Review Letters*, 111(16):165701, 2013.
- [99] JD Bernal and J. Mason. Packing of spheres: co-ordination of randomly packed spheres. *Nature*, 188(4754):910, 1960.
- [100] Corey S O’Hern, Stephen A Langer, Andrea J Liu, and Sidney R Nagel. Random packings of frictionless particles. *Physical Review Letters*, 88(7):075507, 2002.
- [101] M Van Hecke. Jamming of soft particles: geometry, mechanics, scaling and isostaticity. *Journal of Physics: Condensed Matter*, 22(3):033101, 2010.
- [102] Salvatore Torquato, Thomas M Truskett, and Pablo G Debenedetti. Is random close packing of spheres well defined? *Physical Review Letters*, 84(10):2064, 2000.
- [103] Anuraag R Kansal, Salvatore Torquato, and Frank H Stillinger. Diversity of order and densities in jammed hard-particle packings. *Physical Review E*, 66(4):041109, 2002.
- [104] Yang Jiao, Frank H Stillinger, and Salvatore Torquato. Nonuniversality of density and disorder in jammed sphere packings. *Journal of Applied Physics*, 109(1):013508, 2011.
- [105] M Pica Ciamarra, Antonio Coniglio, and Antonio de Candia. Disordered jammed packings of frictionless spheres. *Soft Matter*, 6(13):2975–2981, 2010.

- [106] M. Hermes and M. Dijkstra. Jamming of polydisperse hard spheres: The effect of kinetic arrest. *Europhysics Letters*, 89(3):38005, 2010.
- [107] Carl F. Schreck, Corey S. O’Hern, and Leonardo E. Silbert. Tuning jammed frictionless disk packings from isostatic to hyperstatic. *Physical Review E*, 84:011305, Jul 2011.
- [108] Daniel Vågberg, Peter Olsson, and Stephen Teitel. Glassiness, rigidity, and jamming of frictionless soft core disks. *Physical Review E*, 83(3):031307, 2011.
- [109] Michio Otsuki and Hisao Hayakawa. Critical scaling of a jammed system after a quench of temperature. *Physical Review E*, 86:031505, Sep 2012.
- [110] Romain Mari, Florent Krzakala, and Jorge Kurchan. Jamming versus glass transitions. *Physical Review Letters*, 103(2):025701, 2009.
- [111] Giorgio Parisi and Francesco Zamponi. Mean-field theory of hard sphere glasses and jamming. *Reviews of Modern Physics*, 82(1):789, 2010.
- [112] Patrick Charbonneau, Atsushi Ikeda, Giorgio Parisi, and Francesco Zamponi. Glass transition and random close packing above three dimensions. *Physical Review Letters*, 107(18):185702, 2011.
- [113] FH Stillinger Jr, EA DiMarzio, and RL Kornegay. Systematic approach to explanation of the rigid disk phase transition. *The Journal of Chemical Physics*, 40(6):1564–1576, 1964.
- [114] Tomás S Grigera, Andrea Cavagna, Irene Giardina, and Giorgio Parisi. Geometric approach to the dynamic glass transition. *Physical Review Letters*, 88(5):055502, 2002.
- [115] Yisroel Brumer and David R Reichman. Mean-field theory, mode-coupling theory, and the onset temperature in supercooled liquids. *Physical Review E*, 69(4):041202, 2004.
- [116] Misaki Ozawa, Takeshi Kuroiwa, Atsushi Ikeda, and Kunimasa Miyazaki. Jamming transition and inherent structures of hard spheres and disks. *Physical Review Letters*, 109(20):205701, 2012.
- [117] G. Brambilla, D. El Masri, M. Pierno, L. Berthier, L. Cipelletti, G. Petekidis, and A. B. Schofield. Probing the equilibrium dynamics of colloidal hard spheres above the mode-coupling glass transition. *Physical Review Letters*, 102:085703, Feb 2009.
- [118] Kenneth W Desmond and Eric R Weeks. Random close packing of disks and spheres in confined geometries. *Physical Review E*, 80(5):051305, 2009.
- [119] D Coslovich and G Pastore. Understanding fragility in supercooled lennard-jones mixtures. 2. potential energy surface. *The Journal of Chemical Physics*, 127(12):124505, 2007.
- [120] Daniel Vågberg, Daniel Valdez-Balderas, MA Moore, Peter Olsson, and Stephen Teitel. Finite-size scaling at the jamming transition: Corrections to scaling and the correlation-length critical exponent. *Physical Review E*, 83(3):030303, 2011.
- [121] R. MARI and J. KURCHAN. Dynamical transition of glasses: From exact to approximate. *The Journal of Chemical Physics*, 135(12), 2011.
- [122] A Crisanti and F Ritort. Potential energy landscape of finite-size mean-field models for glasses. *Europhysics Letters*, 51(2):147, 2000.
- [123] Aleksandar Donev, Salvatore Torquato, and Frank H Stillinger. Pair correlation function characteristics of nearly jammed disordered and ordered hard-sphere packings. *Physical Review E*, 71(1):011105, 2005.

- [124] Adam B Hopkins, Frank H Stillinger, and Salvatore Torquato. Disordered strictly jammed binary sphere packings attain an anomalously large range of densities. *Physical Review E*, 88(2):022205, 2013.
- [125] Matthieu Wyart, Leonardo E. Silbert, Sidney R. Nagel, and Thomas A. Witten. Effects of compression on the vibrational modes of marginally jammed solids. *Physical Review E*, 72:051306, Nov 2005.
- [126] Leonardo E Silbert, Andrea J Liu, and Sidney R Nagel. Normal modes in model jammed systems in three dimensions. *Physical Review E*, 79(2):021308, 2009.
- [127] Carl P Goodrich, Andrea J Liu, and Sidney R Nagel. Finite-size scaling at the jamming transition. *Physical Review Letters*, 109(9):095704, 2012.
- [128] Jeffrey S Olafsen. *Experimental and Computational Techniques in Soft Condensed Matter Physics*. Cambridge University Press Cambridge, England, 2010.
- [129] Chris Rycroft. Voro++: A three-dimensional voronoi cell library in c++. *Lawrence Berkeley National Laboratory*, 2009.
- [130] Ning Xu and Emily SC Ching. Effects of particle-size ratio on jamming of binary mixtures at zero temperature. *Soft Matter*, 6(13):2944–2948, 2010.
- [131] Paul J Steinhardt, David R Nelson, and Marco Ronchetti. Bond-orientational order in liquids and glasses. *Physical Review B*, 28(2):784, 1983.
- [132] Hajime Tanaka. Bond orientational order in liquids: Towards a unified description of water-like anomalies, liquid-liquid transition, glass transition, and crystallization. *The European Physical Journal E*, 35(10):1–84, 2012.
- [133] Takeshi Kawasaki and Hajime Tanaka. Structural signature of slow dynamics and dynamic heterogeneity in two-dimensional colloidal liquids: glassy structural order. *Journal of Physics: Condensed Matter*, 23(19):194121, 2011.
- [134] Daniele Coslovich. Locally preferred structures and many-body static correlations in viscous liquids. *Physical Review E*, 83(5):051505, 2011.
- [135] Sadanand Singh, MD Ediger, and Juan J de Pablo. Ultrastable glasses from in silico vapour deposition. *Nature Materials*, 12(2):139–144, 2013.
- [136] Fabian Weysser and David Hajnal. Tests of mode-coupling theory in two dimensions. *Physical Review E*, 83(4):041503, 2011.
- [137] G Foffi, W Götze, F Sciortino, P Tartaglia, and Th Voigtmann.  $\alpha$ -relaxation processes in binary hard-sphere mixtures. *Physical Review E*, 69(1):011505, 2004.
- [138] S Mossa, E La Nave, HE Stanley, C Donati, F Sciortino, and P Tartaglia. Dynamics and configurational entropy in the lewis-wahnström model for supercooled orthoterphenyl. *Physical Review E*, 65(4):041205, 2002.
- [139] Daan Frenkel and Berend Smit. *Understanding Molecular Simulation: from Algorithms to Applications*, volume 1. Academic Press, 2001.
- [140] Hua Tong and Ning Xu. Order parameter for structural heterogeneity in disordered solids. *Physical Review E*, 90(1):010401, 2014.